

DOTTORATO DI RICERCA IN
**Scienze Chirurgiche: Progetto n.1 “Metodologie di
Ricerca nelle Malattie Vascolari”**

Ciclo XXIII

Settore/i scientifico-disciplinare/i di afferenza: MED/22-CHIM/04

New Polymeric Materials for Vascular Surgery

Presentata da: Elisa Cortecchia

Coordinatore Dottorato

Relatore

Chiar.mo Prof. Andrea Stella

Chiar.mo Prof. Andrea Stella

Esame finale anno 2011

ABSTRACT	1
INTRODUCTION.....	3
1. Biomedical Devices and Biomaterials for Vascular Surgery	4
1.1. Vascular Graft.....	5
1.2. Vascular Stents	6
1.3. Stent Grafts	9
1.4. Catheters and Guidewires	10
2. Radiopaque Biomaterials	11
2.1. Fluoroscopy Equipment for Endovascular Procedures	11
2.2. Radiopacity.....	12
2.3. Radiopaque Materials for Enhanced X-ray Visibility in Biomedical Devices	13
2.4. Materials for X-ray Shielding	15
3. Organic-Inorganic Hybrid Materials	17
3.1. Definition and Classification of Organic-Inorganic Hybrids.....	17
3.2. The Sol-Gel Process	18
3.3. Synthesis of Organic-Inorganic Hybrids.....	24
3.4. Applications of Organic-Inorganic Hybrids.....	29
EXPERIMENTAL PART.....	35
1. Materials.....	35
2. Synthetic Procedures	35
2.1. Synthesis of PTMC	35
2.2. Synthesis of Hybrids	36
2.3. Synthesis of PDMS-Titania Hybrids Loaded with Nanoparticles	38
3. Other Procedures.....	39
3.1. Extraction Experiments	39
3.2. Tantalum Sputtering.....	39
3.3. Cytotoxicity Tests	39
4. Instrumental Techniques.....	40
RESULTS AND DISCUSSION.....	43
1. Polyester-Titania Hybrids: Synthesis and Characterization.....	43
1.1. Synthesis and Characterization of Bulk, Self-standing Hybrids	43
1.2. Hybrid Coating on Flat Surfaces	51
2. Polycarbonate-Titania Hybrids: Synthesis and Characterization.....	55
2.1. Synthesis and Characterization of the Organic Phase Precursor PTMC.....	56
2.2. Synthesis of PTMC-Titania Hybrids and Study of Phase Interactions.....	60
2.3. Solid-State Properties of PTMC-Titania Hybrids.....	70
2.4. Hybrid Coating on Flat Surfaces	73

3. Polyester-Titania Hybrid Coatings for X-ray Shielding	75
4. Organic-Inorganic Hybrids for Enhancement of Device X-ray Visibility.....	82
4.1. Synthesis and Characterization of Tantalum Layer	83
4.2. Synthesis and Characterization of PCL-containing Bulk Hybrid and Double-layer Coating (Metal/PCL-Hybrid).....	88
4.3. Synthesis and Characterization of PDMS-Containing Bulk Hybrid and Double-layer Coating..	95
5. PDMS-Titania Hybrids Loaded with Nanoparticles.....	100
5.1. Synthesis of PDMS-Titania Hybrids Loaded with Tantalum Nanoparticles	101
 BIBLIOGRAPHY.....	 111

Abstract

The dramatic impact that vascular diseases have on human life quality and expectancy nowadays is the reason why both medical and scientific communities put great effort in discovering new and effective ways to fight vascular pathologies. Among the many different treatments, endovascular surgery is a minimally-invasive technique that makes use of X-ray fluoroscopy to obtain real-time images of the patient during interventions. In this context radiopaque biomaterials, i.e. materials able to absorb X-ray radiation, play a fundamental role as they are employed both to enhance visibility of devices during interventions and to protect medical staff and patients from X-ray radiations.

Organic-inorganic hybrids are materials that combine characteristics of organic polymers with those of inorganic metal oxides. These materials can be synthesized via the sol-gel process and can be easily applied as thin coatings on different kinds of substrates. Good radiopacity of organic-inorganic hybrids has been recently reported suggesting that these materials might find applications in medical fields where X-ray absorption and visibility is required.

The present PhD thesis aimed at developing and characterizing new radiopaque organic-inorganic hybrid materials that can find application in the vascular surgery field as coatings for the improvement of medical devices traceability as well as for the production of X-ray shielding objects and garments.

Novel organic-inorganic hybrids based on different polyesters (poly-lactic acid and poly- ϵ -caprolactone) and polycarbonate (poly-trimethylene carbonate) as the polymeric phase and on titanium oxide as the inorganic phase were synthesized. Study of the phase interactions in these materials allowed to demonstrate that Class II hybrids (where covalent bonds exist between the two phases) can be obtained starting from any kind of polyester or polycarbonate, without the need of polymer pre-functionalization, thanks to the occurrence of transesterification reactions operated by inorganic molecules on ester and carbonate moieties.

Polyester based hybrids were successfully coated via dip coating on different kinds of textiles. Coated textiles showed improved radiopacity with respect to the plain fabric while remaining soft to the touch. The hybrid was able to coat single fibers of the yarn

rather than coating the yarn as a whole. Openings between yarns were maintained and therefore fabric breathability was preserved. Such coatings are promising for the production of light-weight garments for X-ray protection of medical staff during interventional fluoroscopy, which will help preventing pathologies that stem from chronic X-ray exposure.

A means to increase the protection capacity of hybrid-coated fabrics was also investigated and implemented in this thesis. By synthesizing the hybrid in the presence of a suspension of radiopaque tantalum nanoparticles, PDMS-titania hybrid materials with tunable radiopacity were developed and were successfully applied as coatings.

A solution for enhancing medical device radiopacity was also successfully investigated. High metal radiopacity was associated with good mechanical and protective properties of organic-inorganic hybrids in the form of a double-layer coating. Tantalum was employed as the constituent of the first layer deposited on sample substrates by means of a sputtering technique. The second layer was composed of a hybrid whose constituents are well-known biocompatible organic and inorganic components, such as the two polymers PCL and PDMS, and titanium oxide, respectively. The metallic layer conferred to the substrate good X-ray visibility. A correlation between radiopacity and coating thickness derived during this study allows to tailor radiopacity simply by controlling the metal layer sputtering deposition time. The applied metal deposition technique also permits easy shaping of the radiopaque layer, allowing production of radiopaque markers for medical devices that can be unambiguously identified by surgeons during implantation and in subsequent radiological investigations. Synthesized PCL-titania and PDMS-titania hybrids strongly adhered to substrates and show good biocompatibility as highlighted by cytotoxicity tests. The PDMS-titania hybrid coating was also characterized by high flexibility that allows it to stand large substrate deformations without detaching nor cracking, thus being suitable for application on flexible medical devices.

Introduction

Cardiovascular disease (CVD) is the main cause of mortality in the world and it accounts for around 17 million deaths per year worldwide, which corresponds to 30% of all causes of mortality [1]. The underlying cause of the majority of clinical cardiovascular events is represented by atherosclerosis [2]. *Atherosclerosis* is a chronic, progressive disease of the artery wall intima (artery innermost layer composed of a monolayer of endothelial cells and a connective tissue membrane which anchors the cells to the arterial wall) whose characteristic lesion is the atheromatous plaque. Mature atherosclerotic plaques are constituted of a central core of lipid and cholesterol crystals and cell such as macrophages, smooth muscle cells and foam cells along with necrotic debris, proteins and degenerating blood elements. The core is surrounded by a fibrous cap rich in collagen which separate it from the lumen. Atherosclerosis is a multifocal disease that individuals tend to develop in a number of different types of arteries, i.e. large and small arteries and those feeding the heart, brain, kidneys, and limb. The major complications of this pathology result from progressive narrowing of the vascular lumen, disruption of a plaque followed by thrombus formation, or destruction of the underlying artery wall. Complications due to atherosclerosis are numerous and most of them can be fatal if not diagnosed and effectively treated in time [3,4,5].

The most important complication is *myocardial infarction*, which is a permanent injury to heart muscle initiated by complete thrombotic occlusion of a coronary artery following rupture of an atherosclerotic plaque that was previously only partially obstructive. When the blockage of the coronary artery occurs, the heart muscle is deprived of blood and oxygen and within minutes irreversible death of the tissue begins to occur. On the other hand, when a thrombotic occlusion happens within arteries leading to the brain an ischemic *stroke* occurs, causing partial or total brain damage due to insufficient blood flow. Stroke is the second most common cause of death worldwide after myocardial infarction and it accounts for 9% of total death per year [6]. The presence of carotid artery atherosclerosis predisposes patients to stroke, and the risk of this event is correlated with the severity of the carotid disease [7,8]. *Peripheral Arterial Disease* (PAD) is a chronic arterial occlusive disease of the lower

extremities caused by atherosclerosis. PAD is common in the developed world, affecting approximately 14% to 20% of the adult population, and cases with femoral and popliteal arteries as primary site of involvement constitute the 80-90% of total events [9]. Mild PAD may be asymptomatic or cause intermittent claudication (defined as discomfort, usually in the calf muscles, with exertion that resolves after a few minutes of rest), while when arterial flow to the lower extremities is not able to meet the needs of resting tissue metabolism, critical limb ischemia occurs, causing rest pain in the toes or foot with progression to ulceration and gangrene. Furthermore PAD patients are at high risk for cardiac and cerebrovascular-related events and the majority will eventually die mostly of myocardial infarction or stroke [10].

The great impact that these cardiovascular diseases have on human life quality and expectancy explains the great effort that medical and scientific community is putting on finding more and more effective ways to fight these pathologies. Although a great work has been done in the sense of warning people about the importance of lowering CVD risk factors, such as smoking, overweight and physical inactivity [2], a strong demand of innovative surgical procedures and biomedical devices is present nowadays.

1. Biomedical Devices and Biomaterials for Vascular Surgery

Vascular biomedical devices play a real critical role in the life-saving treatment of patients affected by vascular diseases. Both metallic and polymeric biomaterials are employed for the production of implantable devices, such as vascular grafts and stents, and single use devices, such as catheters and guidewires. Blood compatibility is the most important requirement that all vascular devices need to fulfill and it is defined as the property of a material or device that permits it to function in contact with blood without inducing adverse reactions. Such undesirable blood reactions can be formation of clot or thrombus composed of various blood elements, shedding or nucleation of emboli (detached thrombus), destruction of circulating blood components and activation of immunologic pathways [5]. Here follows a description of the most widely used vascular biomedical devices.

1.1. Vascular Graft

Bypass surgery is a surgical procedure where a graft is used to create a detour around a blocked artery. Although being rather invasive, vascular grafting remains the treatment of choice for heavily clogged or multiple clogged vessels and it is often employed in case of peripheral vascular disease, where diagnosis of blockage is usually delayed and other less invasive procedures do not perform satisfactorily [11].

Critical requirements for the “ideal arterial substitute” are [11,12]:

- biocompatibility → the graft should be non-thrombogenic, non-inflammatory, non-immunogenic, non-toxic and non-carcinogenic;
- mechanical properties → graft should be compliant and elastic, it must closely mimic the unique viscoelastic nature of the artery;
- grafts should accommodate pressure changes, and be non-disruptive to blood flow;
- endothelization → graft should allow growth of a layer of endothelial cells (neointima) that simulates the inner layer of a native blood vessel and serves as a non-thrombogenic surface in a reasonable period of time.

Vascular grafts currently employed for bypass surgery can be classified as autologous or synthetic, the former being a vessel of the patient himself. Current replacements for large arteries are typically fabricated from poly(ethylene terephthalate) (Dacron) or expanded poly(tetrafluoroethylene) (ePTFE). Synthetic grafts perform well in large-diameter, high-flow, low resistance locations such as the aorta and the iliac arteries, having 5 to 10 year patency rates of 90%; in contrast, they perform less well in small-diameter arteries (<6-8 mm) with 5-year patency less than 50% (with ePTFE performing better than Dacron) [5]. In general, the longer the bypass graft, and the smaller the recipient vessel (with a corresponding increase in resistance to flow) the less favorable are both short-term and long-term patency rates. Failure of small diameter vascular prostheses is most frequently due to occlusion by thrombus formation (caused by the absence of spontaneous graft endothelization), or to generalized or anastomotic neointimal hyperplasia (thickening of the neointima due to abnormal cell proliferation determining lumen narrowing, caused mainly by compliance mismatch between graft and artery) [5]. In order to prevent such complications different coatings have been applied on grafts, including fibrin, collagen

and heparin-bound polymers, silicone elastomers, gelatin. In addition, polyurethane has been investigated as an alternative bulk material, owing to its ability to match native artery mechanical properties quite well, but its clinical trials showed worse performance than ePTFE grafts [11].

Therefore in cardiovascular bypass surgery, when small caliber conduits are required, every effort is made to use autologous vessels. In the case of coronary artery bypass, the internal thoracic or internal mammary artery is the first choice graft; in distal bypass surgery, the saphenous vein is harvested and used wherever possible. The main issue associated with autologous grafts employment is that about one-third of patients that need bypass surgery do not have native vessels suitable for grafting, owing to preexisting vascular disease, vein stripping, or vein harvesting for prior procedures [13,14]. That's why an active research on new easily available functional small diameter vascular graft is present.

Tissue engineered vascular grafts have gained attention in recent years [15,16]. Tissue engineering approach consists in the in vitro production of a biological vascular graft through seeding of isolated living cells on bioabsorbable scaffolds. Bioreactors are employed in order to let the new constructs grow in optimized environmental and mechanical conditions that mimic real ones. Scaffold can be made of biodegradable polymers such as polyglycolic acid (PGA), poly(ϵ -caprolactone) (PCL) or poly(lactic acid) (PLA) [17]. Although tissue engineering is proving to be a good strategy for the production of grafts that can fulfill all critical requirements at a time, the main drawback is the long time period required before an individualized graft can be made available (60-90 days) [11]. Arterial bypasses are indeed required on a semi-urgent base for the relief of critical ischemia; in some cases they are needed even urgently, after the onset of acute ischemia which may occur as a consequence of unsuccessful interventional radiological procedures [13].

1.2. Vascular Stents

The stent is a cylindrical mesh tube, generally constructed of metal wire, which is used to open blocked or narrowed arteries through a minimally-invasive endovascular technique which is called transluminal vascular angioplasty with stenting [5]. In this

procedure a stent mounted on a long balloon catheter is inserted in the artery and guided at the site of the stenosis with the aid of X-ray fluoroscopy, a technique that allows to obtain a real-time image of the internal body of the patient through X-ray irradiation. Once the stent-balloon system is correctly positioned, the balloon is inflated, and the stent along with it, to compress the atherosclerotic plaque against the artery wall and restore the original artery patency. When the balloon is deflated and withdrawn, the stent remains in place, serving as permanent scaffolding for the newly widened artery.

The characteristics of an “ideal” stent are [18,11]:

- biocompatibility → stents should be non-thrombogenic, non-inflammatory, non-immunogenic, non-toxic and non-carcinogenic;
- mechanical properties → stents should have good expandability in order to conform to the vessel wall once the balloon is inflated, and after deflation should be able to overcome the forces imposed by the atherosclerotic arterial wall and not collapse. The device should be also flexible enough to travel through even the smaller diameter atherosclerotic artery;
- low profile → stent should have the ability to be crimped on the delivery catheter;
- radiopacity → stents should have adequate X-ray radiopacity to assist clinicians in assessing its “in-vivo” location;
- endothelization → stents should allow growth of the neointima in a reasonable period of time.

Stents have been used in patients since the 1980s [5]; metals have been the first choice for stent manufacturing because they generally allow to obtain devices with well-suited mechanical properties and good X-ray radiopacity [19]. The majority of stents in use today are composed of 316L stainless steel or nitinol [18]. 316 stainless steel has good mechanical properties and excellent corrosion resistance. However is a poor radiopaque material and it has also some biocompatibility issues due to toxic ion release (Ni, Cr, Mo) [20]. Nitinol is a shape memory alloy composed of nickel and titanium. It is used for the production of self-expanding stents, devices that have a small diameter at room temperature and that are able to regain their original shape (previously “memorized” according to the diameter of the target vessel) at body

temperature conforming to the artery wall [18]. Nitinol is also characterized by suitable mechanical properties, but its main drawback is the occurring of toxic nickel ion release [21,22]. Another metal alloy which has been approved by FDA for stent production is the Co-Cr one, which is characterized by excellent radial strength and good X-ray visibility [18]. On the contrary, tantalum stents have not been approved by FDA, but these stents are commercially released in Japan, Canada and Europe [18]. Ta has excellent corrosion resistance, is biocompatible and it is excellently visible under X-ray fluoroscopy. However Ta stents commercial availability is lower than that of 316L stainless steel or nitinol ones because of poor mechanical properties that enhance the risk of stent breaking during deployment.

The early complications of stenting generally involve subacute stent thrombosis that occurs in 1% to 3% of patients within 7 to 10 days of the procedure [5]. This complication has largely been overcome by aggressive multidrug treatment. The major long-term complication is in-stent restenosis (renarrowing of the vessel localized at the stent site), which occurs within 6 months in 50% of patients who are stented. Many approaches have been used in the attempt to reduce in-stent restenosis: the most promising results were attained with the so-called drug eluting stents (DES). First-generation DES contain drugs embedded in a polymer matrix that is coated onto the stent [23]. The drug is released by diffusion over varying periods of time that can be tailored by the specifics of the polymer-drug system. Examples of polymer matrix employed on commercial DES are polyethylene-co-vinyl acetate (PEVA), poly-n-butyl methacrylate (PMBA) and the triblock copolymer poly(styrene-b-isobutylene-b-styrene) (SIBS). While several trials and investigations have supported the short-to-medium term safety and efficacy of these stents (restenosis is eliminated over time periods of 2 years and longer), doubts have been raised about long-term safety, particularly concerning the risk of late stent thrombosis, that seems related to the inflammatory reaction induced by polymeric drug carriers [24]. In second-generation DES a biodegradable polymer, such as PLA or polylactic-co-glycolic acid (PLGA), is used as the drug carrier, eliminating doubts about long-term effects of the polymer. A number of devices are currently in clinical trials but it will need some other time to know how successful they will be in the long-term [23].

A last category which is worth mentioning is that of totally biodegradable stent materials. Indeed the stent is a foreign object within the vessel and its presence is associated with the potential for inflammatory reactions, progressive abnormal neointima development, damaged endothelium and thrombosis. Biodegradable stents have been made using polymeric materials, such as poly(L-lactic acid) (PLLA), but also metallic alloys based on magnesium or iron [23,18]. Common to all these systems is the lack at the present of clinical evidence demonstrating a clear advantage of this approach, hence there should be a focus on materials and clinical research in the coming years.

1.3. Stent Grafts

An aneurysm is a permanent, localized dilation of a blood vessel defined by an increase greater than 50% in the diameter compared with the expected normal diameter. The predominant extracranial location for aneurysm is the infrarenal aorta, where abdominal aortic aneurysm (AAA) occurs. Aneurysm may cause arterial occlusion or distal embolization of thrombus, but tissue failure, rupture and exsanguinations are the most deadly outcomes [7].

Endovascular procedure with stent graft application has been introduced for the AAA repair since the 1990s. Stent grafts are devices composed of a metallic frame (stent) covered by a polymeric fabric tube (graft) and combine the features of stents and vascular grafts. While the graft portion is intended to provide a mechanical barrier to prevent intravascular pressure from being transmitted to the weakened wall of the aneurysm (thus excluding the aneurysm from the flow of blood), the metallic structure positions the graft precisely without the need for a surgical connection, and at the same time provides a certain level of support. "Ideal" stent graft should fulfill requirements already listed for both vascular grafts and stents; in addition the graft material must be strong enough to resist late deterioration and damage due to friction with metallic parts of the device, that need to be thin enough to be compressed in a small delivery catheter. Various materials have been tested for the fabric part and all majors producers now use the two materials most employed in surgery, i.e. polyester and ePTFE. Other materials, such as polycarbonate and polyurethane, are under

investigation. The metallic part is generally made of nitinol or stainless steel in accordance with what previously discussed for vascular stent.

1.4. Catheters and Guidewires

Guidewires and catheters are fundamental for any interventional procedure in endovascular surgery. In general, guidewires are devices that enable to progress through a blood vessel; after they are introduced, they provide support for insertion of the catheter, stent, balloon, or other materials required for a specific diagnostic or therapeutic procedure [25]. Standard guidewires typically comprise a core wire formed from metals such as stainless steel, nitinol and tantalum [26]. Guidewires have usually been coated with polymers such as PTFE and silicone in order to facilitate placement through the vasculature. More recently, guidewires have been coated with hydrophilic polymers, such as polysaccharides, that are able to trap a film of water on the surface of the device which prevents direct contact with the vessel wall and with the catheter which is introduced over the guidewire. Each guidewire has a specific length, thickness, composition, and maneuverability for the different purposes for which it was designed [25]. Like guidewires, catheters are shaped to facilitate the procedure for which they are employed [25,27]. They are normally described by their length, external diameter and tip design. Similarly to other biomedical devices already described, properties which are required for optimal vascular catheter comprehend biocompatibility, rapid endothelization, radiopacity, flexibility and resistance to compression. Moreover catheters need to have a low friction coefficient in order to reduce both pain perceived by the patient and endothelium damage during device insertion. Vascular catheters are usually constructed of polyethylene (PE), polypropylene (PP), nylon, PTFE, silicone, polyurethane and combination of these materials. Like guidewires, catheters can be coated with other materials in order to improve characteristics such as blood compatibility and friction. As already explained about catheters shape, also the constituent material must be selected based on an assessment of the intended application. Polyurethane catheters are for example soft and pliable, and follow guidewires easily, but they have a high coefficient of friction. On the contrary nylon

catheters are stiffer and they tolerate higher flow rates, thus they are useful for examination of large arteries.

2. Radiopaque Biomaterials

Endovascular surgeons make use of X-ray fluoroscopy to obtain real-time images of the patient during interventions. Interventional fluoroscopy represents a great advantage over invasive surgical procedures, because it requires only a very small incision, substantially reduces risks of infection and allows for shorter recovery time compared to surgical procedures. The preference to use methods that are less invasive and less costly than surgery has driven in the past ten years the increasing of number of fluoroscopic procedures performed. In this context radiopaque biomaterials plays a fundamental role as they are employed both to enhance visibility of devices during interventions and to protect medical staff and patients from X-ray radiations.

2.1. Fluoroscopy Equipment for Endovascular Procedures

The fluoroscopic imaging system is constituted of an X-ray generator, divided in a high-voltage transformer and an X-ray tube, and an imaging chain, which is composed of an image intensifier and a display. The image intensifier and the X-ray tube are usually mounted together in a C-shaped configuration, which is called gantry [27].

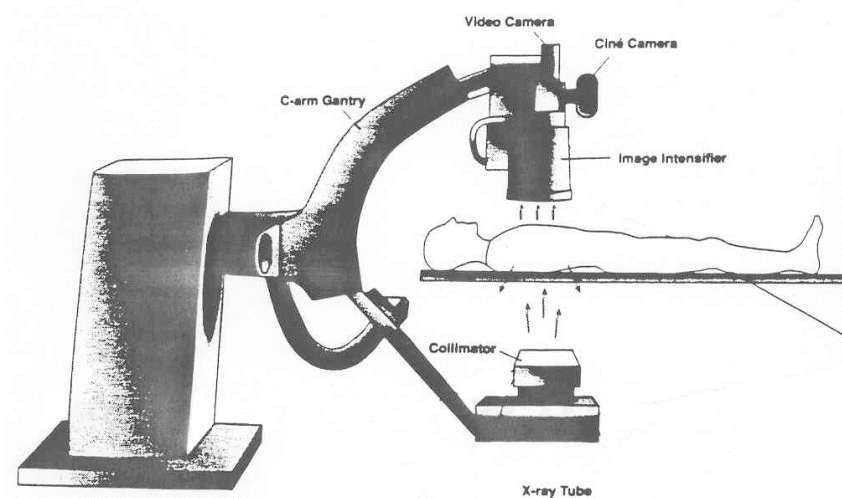


Figure 1. Schematization of a fluoroscopic equipment

X-ray photons are generated by a vacuum tube that has a stationary cathode and a rotating anode. A focal spot on the anode is bombarded by electrons from the cathode, exciting the anode to produce X-ray photons. The energy of the electron, and hence the energy of the generated photons, is determined by the voltage potential between the cathode and the anode. The number of available electrons accelerated into the anode, and hence the number of photons produced, is controlled by the amount of current (measured in mA) passed through the filament in the cathode. The X-rays emitted from the tube pass through the patient. On interfacing with the patient, some photons are absorbed, some are reflected (scattered radiation) and some pass entirely and strike the image intensifier. The image obtained is transmitted to a video system that displays a real-time moving image, in which darker images usually corresponds to higher X-ray absorption (hence lower intensity of transmitted radiation). Image quality can be improved varying both kilovoltage and current. By increasing the voltage potential a “harder”, high-energy spectrum is produced and this leads to increased radiographic penetration and lower contrast. As concern current, an insufficient intensity of the radiation reaching the image device results in a grainy image appearance.

2.2. Radiopacity

Radiopacity is defined as the capability of a substance to hinder or completely stop the passage of X-rays [28]. An X-ray beam loses intensity in traversing matter both by absorption, which is a transformation from X-rays into kinetic energy of ejected electrons, and by scattering, a transfer of radiant energy from the primary beam to scattering beams that originate in the atoms of the absorbing matter [29]. The intensity of the transmitted X-ray radiation (I) through a sample, which decreases as the radiopacity of the analyzed material increases, is expressed by the following equation:

$$I = I_0 \cdot e^{-\rho m x} \quad [\text{Eq. 1}]$$

where I_0 is the intensity of the incident radiation, m is the mass attenuation coefficient of the material, ρ is the density and x is the sample thickness. Since the loss

of intensity is due to the combined effects of absorption and scattering, m can be divided in two separated terms, as shown in the following equation:

$$m = \frac{\mu}{\rho} = \frac{\tau}{\rho} + \frac{\sigma}{\rho} \quad [\text{Eq. 2}]$$

where μ is the linear attenuation coefficient, τ/ρ is the true absorption coefficient and σ/ρ is the scattering coefficient. The second term is the less important of the two and it contributes a relatively small amount to the total absorption. It doesn't vary greatly with changes in the wavelength or atomic number. On the contrary, the true absorption coefficient varies markedly with wavelength and atomic number according to the following relation:

$$\frac{\tau}{\rho} = cZ^3\lambda^3 \quad [\text{Eq. 3}]$$

where Z is the atomic number, λ is the wavelength of the X-ray radiation and c is a constant (which has different values in different λ ranges, delimited by absorption edges K , i.e. K corresponding to energy that equals the energy of electronic levels). Owing to the fact that true absorption predominates over scattering, substituting equation [Eq. 3] in [Eq. 1], it is obtained that the transmitted X-ray radiation, hence the radiopacity of the material, is dependent on the atomic number of atoms constituting the material, on material thickness and density. In particular an increase in atomic number, thickness or density determines a lower intensity of transmitted radiation, hence a higher radiopacity of the material. It is worth noting that also the radiation wavelength λ has a direct influence on I , and this explains why increasing X-ray radiation energy in a fluoroscopic equipment (through increase of kilovoltage), results in a smaller difference between intensity of radiation through material and background, hence in a less contrasted image.

2.3. Radiopaque Materials for Enhanced X-ray Visibility in Biomedical Devices

X-ray identification and traceability is nowadays an essential requirement for medical devices in many surgical and medical applications. As a matter of fact, medical devices such as vascular stents or catheters with good radiopacity can be easily positioned (and later-on detected) inside the human body through fluoroscopy and X-ray radiography, thus avoiding invasive surgical procedures on patients. Medical devices with improved radiopacity can be obtained following three different strategies:

1. modification of the bulk material that constitutes the device in order to enhance its ability to absorb X-ray radiation [30,31,32];
2. application at the device surface of small bulk radiopaque markers attached to the device structure [33,34];
3. application at the device surface of a radiopaque coating [35,36].

As concerns the first route, many polymeric materials with improved visibility have been obtained by the incorporation into the polymer of radiopaque compounds, such as barium [37,38] and strontium salts [39] or by linking to the polymer chain (through covalent bonds) radiopaque - typically halogen-containing - moieties [40,41,42,43]. Highly-radiopaque metallic materials have been also successfully produced by alloying radiopaque elements (tantalum, iridium, platinum, palladium, etc.) with typical biomedical metallic materials such as nitinol and titanium [44,45,46]. Although this route allows to obtain devices characterized by an excellent level of radiopacity, the principal drawback in choosing this strategy is that the addition of the radiopaque component in the bulk material often leads to change in its properties, negatively affecting device performance [47,48].

Impact on bulk material properties can be substantially reduced if an intrinsically radiopaque material is applied at the surface of the device rather than incorporating it in the bulk structure. Radiopaque markers are generally small metallic objects that are crimped to the device structure. These markers are typically formed of a radiopaque material such as tantalum, gold, or platinum [49]. In order to help surgeons in identifying the full-body of the implanted device during delivering inside the patient, multiple markers can be placed in strategic positions along the device to completely delineate its surface [49,50]. Markers with particular shape have also been developed to allow identification of both position and orientation of the device [51]. The main issue associated with radiopaque marker employment is the requirement of a very complex technology for the attachment of these objects on the device surface, because marker fixation must be performed without deforming the device, thus avoiding formation of cracks on its surface [52,53,54]. Furthermore, devices need often to be designed in order to make possible the allocation of markers inside their structure [53,54]. This is necessary because the presence of roughness at the device

surface can lead to difficult device insertion inside the vessel and, worst of all, to damage of the vessel wall [55].

Deposition of a thin coating layer of a radiopaque compound at the device surface is a quite simple process compared with the complex and costly fixing technologies currently used to apply external small radiopaque bulky markers to biomedical devices. A strong improvement of device X-ray visibility has been obtained by the application of a surface layer of a radiopaque metal, such as tantalum [56], using physical vapor deposition techniques or electroplating. The increase of visibility is significant even if few micrometer-thick layers are applied. However such metal coatings have some main drawbacks, such as (i) low adhesion to the substrate leading, upon metal corrosion, to the release of ions inside the human body and (ii) inability of the metal coating to follow substrate deformation, thus causing surface cracking [57]. Some of the earlier efforts to improve radiopacity utilized gold coatings on conventional stainless steel devices [58]. Unexpectedly, coated devices were associated with poor clinical outcomes that showed an increased risk of restenosis with respect to the bare metal ones.

2.4. Materials for X-ray Shielding

The majority of the radiation dose received by patient and hospital staff using X-ray derives from procedures involving fluoroscopy [59]. The number of fluoroscopic interventional procedures performed every year has steadily increased because of the preference to employ methods that are less invasive for the patient and also less costly than standard surgery [60]. At the same time, the complexity of interventional fluoroscopy has been increasing rapidly due to the development of new devices and procedures, such as endografts for the treatment of AAA. Although the benefits of properly performed interventional fluoroscopy almost always outweigh the radiation risk experienced by an individual, unnecessary exposure to X-rays may produce negative consequences to operators as well as to patients.

Biologic effects of radiation can be grouped as stochastic and non-stochastic effects. A stochastic effect is one in which the probability of the effect, rather than its severity, increases with dose [61]. Radiation-induced cancer and genetic effects are stochastic.

These kinds of injuries are believed to lack a threshold dose because damage to few cells or even a single cell could theoretically result in production of the effect. On the other hand, there are other effects for which the probability of causing certain types of harm will be zero at small radiation doses. Above some threshold level, damage will become apparent, with severity increasing as dose rises above the threshold. Such effects are called non-stochastic or deterministic effects. Cataracts, erythema, epilation, dermal necrosis and even death are examples of the deterministic effects that can result from high X-ray radiation exposure.

Health care providers are at risk from radiation damage from chronic X-ray exposure. There are indeed an increasing number of case reports of skin changes on the hands and injuries to the eye lenses in operators and assistants [62]. Furthermore, leukemia and breast cancer episodes have been associated with radiation exposure [63]. Therefore it is extremely important that appropriate protection devices are in place for interventional operators. Personal protective equipment currently employed includes lead-containing apron and neck collar to shield respectively the trunk and the thyroid from scattered X-ray radiation [64,65]. These garments consist of a multilayer sheet having two polymeric outer layers and a core layer constituted of a polymer rubber in which fine particles of lead oxide are dispersed. Although lead filled garments provide an excellent protection against the harmful effects of X-rays, they are often heavy, stiff, bulky and lacking in breathability. As such, they result uncomfortable and restrictive. As a matter of fact cervical radiculopathy, low back strain and disc problems have been reported in relationship to wearing lead aprons and extending the neck to see the image monitor of the fluoroscopic equipment [27]. Moreover, lead is a toxic substance which must be handled carefully and cannot be carelessly disposed of. Last but not least, because of lead's heavy weight, lead garments that cover the whole operator's body cannot be produced, leaving operator head, arms and lower legs unprotected. In patent literature recent documents about the production of light weight radiation resistant clothing can be found, showing the necessity of new full-body covering clothes. In a US patent of 2004, radiopaque garments are realized impregnating the fibers with barium sulfate compounds, or laminating a polymer/barium mixture onto one or more layer of the fabric [66]. Another strategy is illustrated in a US patent application of 2010, where the garment is impregnated with

a water solution of a bismuth salt, which is then absorbed on garment fibers with the help of a fixing agent that makes the salt insoluble [67]. These new X-ray shielding clothes will be able to shield from X-ray previously unprotected body areas.

3. Organic-Inorganic Hybrid Materials

3.1. Definition and Classification of Organic-Inorganic Hybrids

Organic-inorganic hybrids can be defined as synthetic materials where organic and inorganic phases are mixed at the nanometer to sub-micrometer scale. The organic phase is generally constituted by a polymer (but can also be constituted by an organic molecule or an oligomer) while the inorganic phase is constituted by a metal oxide in form of particle or cluster [68]. In the 1980s this class of components was named “ormocers” (organically modified ceramic polymers) by Schmidt et al. [69] and “ceramers” (ceramic polymers) by Wilkes et al. [70], with the aim to stress their dual organic and inorganic nature. This class of materials has gained increasing attention in recent years because of the remarkable changes of the thermal [71,72], mechanical [68], electrical [73,74], magnetic [75] and optical [76] properties obtained by the organic-inorganic combination compared with the plain polymeric and ceramic components. Optical transparency, for instance, is a property that stems from the presence of nanostructured inorganic domains in hybrids whose components are characterized by different refractive indexes [77].

The nature and strength of interactions at the interface between organic and inorganic phase domains strongly influences the final material behavior. Therefore hybrids are conveniently divided in two groups based on the type of organic-inorganic interactions [78]:

- Class I → includes hybrid materials where organic and inorganic components interact through weak interactions, i.e. van der Waals, hydrogen bonding or ionic interactions;
- Class II → corresponds to hybrid materials where organic and inorganic components are bonded through strong covalent or ionic-covalent chemical bonds. Within many class II hybrid materials, organic and inorganic

components can additionally interact through the same kind of weak bonds that define Class I hybrids.

3.2. The Sol-Gel Process

Polymers are generally characterized by poor thermal stability (less than 250°C) meaning that high temperatures are prohibited during organic-inorganic hybrid formation process. A common way to obtain hybrid materials is represented by the sol-gel process, a synthetic method that applies mild processing conditions (low temperature) initially developed for the production of inorganic ceramics and glasses [79,80]. The process allows to obtain inorganic metal oxides MO_x ($M = Si, Ti, Zr, Al, Mo,$ etc.) via “inorganic polymerization” reactions, employing as molecular precursors correspondent metal alkoxides $M(OR)_y$ ($R = OC_nH_{2n+1}$) [81]. Reactions need to be carried out in a solvent, and the term “sol-gel processing” is often broadly used to describe the synthesis of inorganic oxides by “wet chemistry” methods [82]. The steps involved in the synthesis of sol-gel derived metal oxides are the following [80]:

1. Mixing → in this step a solution of the convenient precursors is prepared and “inorganic polymerization” reactions start to occur at numerous sites within the solution, leading to the formation of interconnection bonds between precursor molecules. When sufficient bonds are formed in a region, they respond cooperatively as colloidal particles or a *sol*;
2. Gelation → with time the colloidal particles link together, to become a three-dimensional network, forming what is called a *gel*. At gelation, the viscosity of the systems increases sharply. Solvents and reaction byproducts remain in the pores of the network;
3. Aging → during aging, the gel is maintained at ambient temperature for a period of time, polymerization reactions continue along with localized solubilization and reprecipitation of the gel network, which increases the thickness of interparticles neck and decrease the porosity. After a certain time, solvent evaporation from the interconnected pore network starts, causing the gel shrinkage and the increase of its rigidity;

- *Alcoxolation* → a reaction by which a bridging oxygen bond M-O-M is formed through condensation of one hydroxyl group and one alkoxy group, with the elimination of an alcohol molecule. The mechanism is basically the same as for hydrolysis with M replacing H in the entering group;

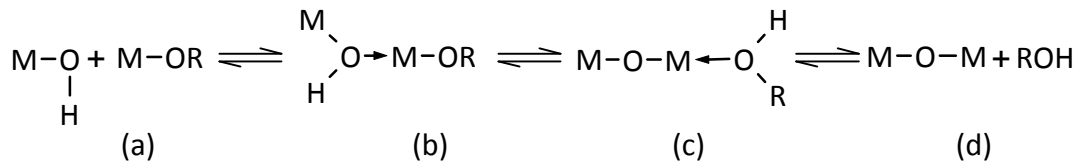


Figure 4. Alcoxolation reaction mechanism

- *Oxolation* → two hydroxyl groups react together to form an M-O-M bond. The reaction follows the same mechanism as alcoxolation, but the leaving species is a water molecule in this case;

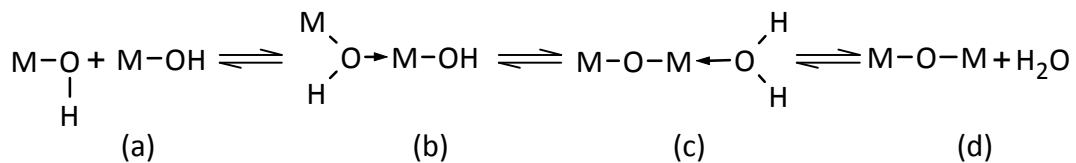


Figure 5. Oxolation reaction mechanism

- *Olation* → this kind of condensation reaction can occur when the coordination unsaturation of the metal atom, given by the difference between the maximum coordination number N of the metal atom in the oxide and its oxidation state Z, doesn't equal zero. In this case bridging hydroxyl group can be formed through the elimination of a solvent molecule or of a water molecule;

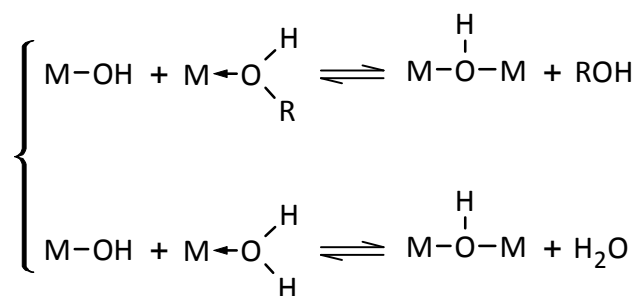


Figure 6. Olation reaction mechanism

Generally, both the hydrolysis and condensation reactions occur simultaneously in the system once the hydrolysis reaction has been initiated. The structure and morphology of the resulting oxide strongly depend on the relative contribution of each reaction. These contributions can be optimized by carefully adjusting the experimental conditions which are related to both internal (nature of the metal atom and alkoxy group, structure of the molecular precursor) and external parameters (catalyst, solvent, temperature, etc.):

- *Nature of the metal atom* → the degree of reactivity of a given metal or semi-metal atom of an alkoxide is mainly due to its electrophilic character (measured by electronegativity, X) and to its ability to increase its coordination number (Table 1). Since transition elements are more electropositive than silicon, nucleophilic addition of a water molecule in the first step of hydrolysis is much easier for transition metal alkoxides [82]. It is also worth noting that coordination expansion of the metal occurs upon hydrolysis. In silicon alkoxides the Si atom is characterized by a degree of unsaturation equal to zero. On the contrary, in transition metal alkoxides the full coordination of the metal atom is not satisfied and the latter tends to increase its coordination number by using its vacant d orbitals to accept oxygen lone pairs from water molecules.

Table 1. Electronegativity (X), number of coordination (N) and degree of unsaturation of interesting metals (adapted from [83])

Alkoxide	X	N	Z	$N - Z$
$\text{Si}(\text{OPr}^i)_4$	1.90	4	4	0
$\text{Sn}(\text{OPr}^i)_4$	1.96	6	4	2
$\text{Ti}(\text{OPr}^i)_4$	1.54	6	4	2
$\text{Zr}(\text{OPr}^i)_4$	1.33	7	4	3
$\text{Ce}(\text{OPr}^i)_4$	1.12	8	4	4
$\text{Al}(\text{OPr}^i)_3$	1.61	6	3	3

Experimental practice has indeed shown that while silicon alkoxides are not very reactive with respect to water, transition metal alkoxides react vigorously

and a strongly exothermic reaction is observed as soon as the alkoxide is brought into contact with water [82]. Takahashi and co-workers thoroughly studied the reactivity of transition metal alkoxides, and they demonstrated the possibility of running sol-gel reactions even without water addition [84]. In fact, they observed that water, which is indeed required for hydrolysis to occur, can be obtained in a convenient amount and concentration from air humidity, thus avoiding any undesired oxide precipitation;

- *Nature of the alkoxide precursor* → some kinetic studies made on the sol-gel process of different silicon alkoxides have shown that the rate of hydrolysis generally decreases as the dimension of the alkoxide group increases. This behavior is attributed to two factors:
 1. *Steric hindrance* → the longer and the bulkier is the alkoxide group, the more difficult is the nucleophilic attack of the water molecule onto the metal atom [80];
 2. *Inductive effect* → the partial positive charge on the metal atom, hence its electrophilicity, decreases as the length of the bound alkoxide group increases, inhibiting the nucleophilic attack of water to the metal atom. For the same reason, in the second step of the hydrolysis reaction, the proton transfer from the added water molecule to the OR group is disfavored by the presence of long chain alkyl groups that lower the proton partial positive charge [85];
- *Molecular structure of the alkoxide* → as already described, when the metal atom unsaturation degree in the alkoxide is not equal to zero, the metal tends to increase its coordination number accepting oxygen lone pairs from nucleophilic ligands [82]. In non-polar solvents this will lead to the formation of oligomers of two or more alkoxide molecules, linked together by OR bridging bonds (Figure 7). The formation of this complex molecules, that decreases both hydrolysis and condensation reaction rates, can be inhibited by the presence of polar solvents, which are able to solvate the alkoxide molecule, or by employing alkoxides with bulky OR groups that cause steric hindrance;

a nucleophilic activation of silicon through the coordination of the nitrogen lone pair [85]. Conversely, using NaOH, it was revealed that hydrolysis of $\text{Ti}(\text{OBu})_4$ was more difficult than under neutral condition [86]; in this case, nucleophilic addition of OH^- on Ti atom can occur, which decreases the positive charge of the metal atom. Unlike hydrolysis, condensation is always activated by base catalysts, thanks to formation of the highly nucleophilic species M-O^- . The condensation involves the attack of a deprotonated M-O^- group on a neutral species M-OH or M-OR . According to the literature, in base-catalyzed conditions, the condensation occurs preferentially between highly condensed species, leading to strongly cross-linked structures [79].

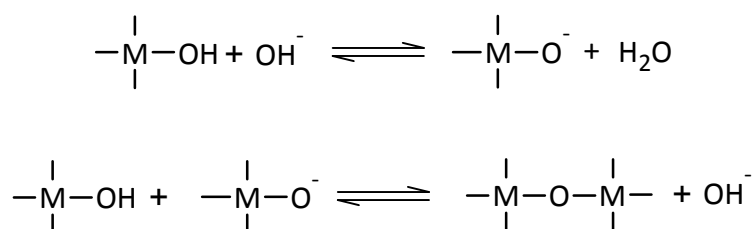


Figure 9. Base catalyzed condensation reaction

- *Temperature* → increasing the temperature generally activates both hydrolysis and condensation processes. As a consequence, with poorly reactive precursors such as $\text{Si}(\text{OR})_4$, the temperature may be increased to activate the sol-gel process [82]. On the other hand, for strongly reactive precursors such as transition metal alkoxides, the temperature must be lowered in order to slow down hydrolysis and condensation processes and prevent metal oxide precipitation.

3.3. Synthesis of Organic-Inorganic Hybrids

Synthetic strategies based on sol-gel developed for the production of organic-inorganic hybrids can be divided into two main groups, the first which includes strategies for the synthesis of Class I materials and the second which comprises strategies for the synthesis of Class II hybrid materials.

Synthesis of Class I Organic-Inorganic Hybrids

- *Organic monomers dispersed in sol-gel matrices* → sol-gel inorganic oxides are often highly porous structures, consequently the pores of the structure can be filled by immersing the bulk in a solution containing a polymerizable organic monomer, such as methylmethacrylate, or butadiene, and a convenient catalyst. In a second step, polymerization is started either by UV irradiation or by heating and the polymer is formed. Organic functional molecules can be also mixed with the organic monomer in order to make materials with specific optical properties [78,81];
- *Inorganic phase precursors dispersed in polymer matrices* → this strategy consists of mixing together the polymer and the metal alkoxide in a suitable solvent (alcohol, THF, etc.) [78,81]. Catalyst and water may be added to the mixture and the inorganic polycondensation is performed *in situ*. The best system homogeneity is achieved when the weak interactions developed between organic and inorganic phases are sufficient to force networks to interpenetrate mutually at the molecular level. For example some M-OH groups generated during sol-gel process could remain at the surface of the growing inorganic particles and form hydrogen bonds with carbonyl groups that can be present on the polymeric chain. Following this strategy silica hybrids have been obtained employing polymers such as poly(N-vinyl pyrrolidone) [87] and poly(2-methyl 2-oxazoline) [88];
- *Simultaneous formation of interpenetrating organic-inorganic networks* → this strategy has been proposed for the production of homogeneous nanocomposites based on silica [78]. The materials are synthesized through a synchronous organic polymerization and hydrolysis/condensation of modified silicon alkoxides, which are employed as the unique hybrid precursor. These alkoxide molecules possess two distinct reactivities: the first is due to the metal atom and causes the formation of the oxide network SiO₂, while the second results from the presence of a polymerizable group. An example of such modified alkoxide is represented by silicon alkoxides bearing an alkoxy group carrying a methacrylate function [89] (Figure 10).

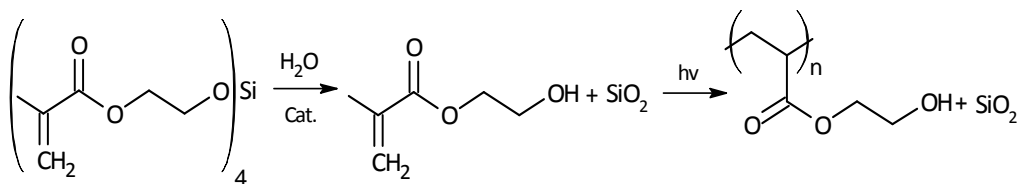


Figure 10. Example of functionalized alkoxides employed for the simultaneous formation of interpenetrating organic-inorganic networks

The functionalized alkoxy group is initially bonded to the metal atom through an M-O-C bond. This bond is hydrolyzed during the hydrolysis-condensation step, thus releasing the polymerizable organic group. By the application of either UV-light or heating during sol-gel process, two networks are formed independently, without mutual chemical bonds. Furthermore, since the unsaturated alcoholic molecules used as solvent are the same as those released during hydrolysis, they are involved in the methacrylate polymerization. Hence no gel drying is necessary and, if the density of the monomeric species and the polymer are similar, the material shrinkage is negligible.

Synthesis of Class II Organic-Inorganic Hybrids

- *Synthesis from polymers bearing sol-gel reactive groups* → the synthesis is conducted using polymers that bear, either at chain end or along the polymeric backbone, chemical moieties able to react with alkoxides units during the sol-gel process. As an example, a dihydroxy-terminated polymer has two –OH terminals which may condensate with M-OH groups during hybrid synthesis. In the first hybrid system developed by Wilkes et al., silanol-terminated (Si-OH) PDMS was selected as the polymeric component [70]. In this hybrid Si-O-Si bonds covalently link PDMS with SiO₂ inorganic phase. More recently, hybrids were obtained also by reacting silanol-terminated PDMS with precursor of transition metal oxides like titania, zirconia and tantalum oxide [90,91]. In such case the link between PDMS and the metal oxide is constituted by oxygen that bridges silicon to the transition metal, i.e. Si-O-Ti, Si-O-Zr, and Si-O-Ta. Generally, when transition metal alkoxides are employed, due to their high reactivity with respect to hydrolysis, it is

necessary to introduce in the initial system a convenient additive which slows down condensation reaction; in such condition, contact between polymeric chain terminals and M-OH groups is promoted. As already pointed out, inorganic acids are able to inhibit condensation reaction, through protonation of nucleophilic species M-OH. Alternatively, the chemical reactivity of transition metal alkoxides can be controlled by using strong complexing ligands. The best ones are β -diketones and their derivatives, polyhydroxylated ligands such as polyols, and also α - or β -hydroxyacids [78]. Acetylacetonate (*acac*) is known to be a rather strong chelating ligand and it has been often reported in the sol-gel literature as a stabilizing agent for non-silicate metal alkoxide precursors ($\text{W}(\text{OEt})_6$, $\text{Zr}(\text{OR})_4$, $\text{Ti}(\text{OR})_4$, etc.) [92] (Figure 11).

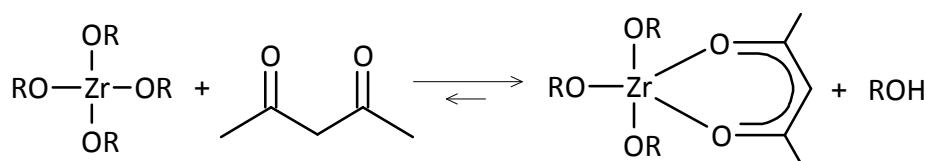


Figure 11. Reaction of a β -diketones with a transition metal alkoxide

Complexing ligands such as *acac* lead to less hydrolysable M-*acac* bonds which prevent fast condensation and favor reaction with polymeric chain terminals. Hydrolysis/condensation reactions of *acac*-modified alkoxides are mainly governed by the complexation ratio, defined the molar ratio between *acac* and metal atoms;

- *Functionalization of polymer chain with alkoxysilane group* \rightarrow this strategy consists of modifying the polymer chain ends, prior to reaction with metal alkoxides, with functional groups that also bear metal alkoxide units, mainly triethoxysilyl and trimethoxysilyl units (Figure 12). When the functionalized polymer and the inorganic precursor are solubilized in a convenient solvent, polymeric chains are able to condensate with alkoxide units resulting in their covalent incorporation inside the inorganic network.

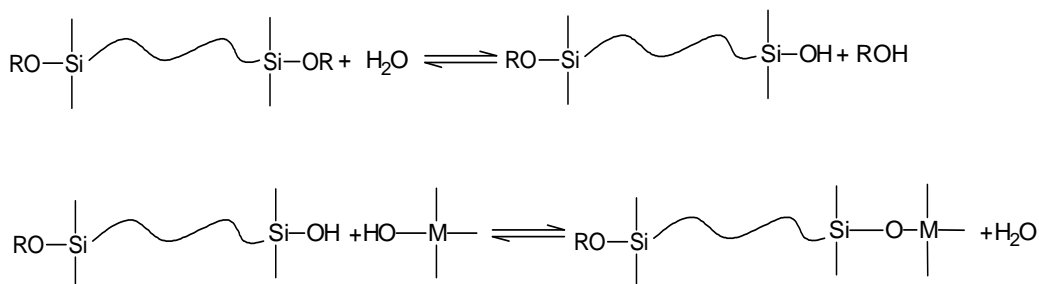


Figure 12. Hydrolysis and condensation reactions of alkoxy silane modified polymers

The strategy has been employed to synthesize hybrids using a wide range of polymers as the organic phase, including poly(tetramethylene oxide) (PTMO) [93,94], poly(ether ketone) (PEK) [95], poly(ethylene oxide) (PEO) [96,97] and PCL [98];

Transesterification reactions → in a recent work by Mazzocchetti et al. [99], an organic-inorganic hybrid was prepared via the sol-gel process starting from a dihydroxy-terminated polyester, i.e. poly(1,4-butylene glutarate) (PBG), and titanium tetraisopropoxide (TIPT) as inorganic oxide precursor. In the cited work, it was demonstrated that a strong interaction between the polymer and the in situ forming titania was achieved via the transesterification reaction of the polymer chain, leading to organotitanium esters connecting organic and inorganic domains (Figure 13). The presence of organotitanium esters bonds was confirmed by FT-IR and XPS analyses of the material. It was observed that the extent of the transesterification reaction strongly depends on the reaction solvent and on the presence of acid in the reaction mixture: transesterification is favored by the presence of the acid and by the use of solvents which are not able to solvate the metal atom, such as chloroform. Because the transesterification reaction does not require the presence of any specific chain end group, in principle any polyester able to dissolve in a good solvent for the titania precursor should be able to lead to hybrid structure such as those observed with hydroxyl-terminated PBG.

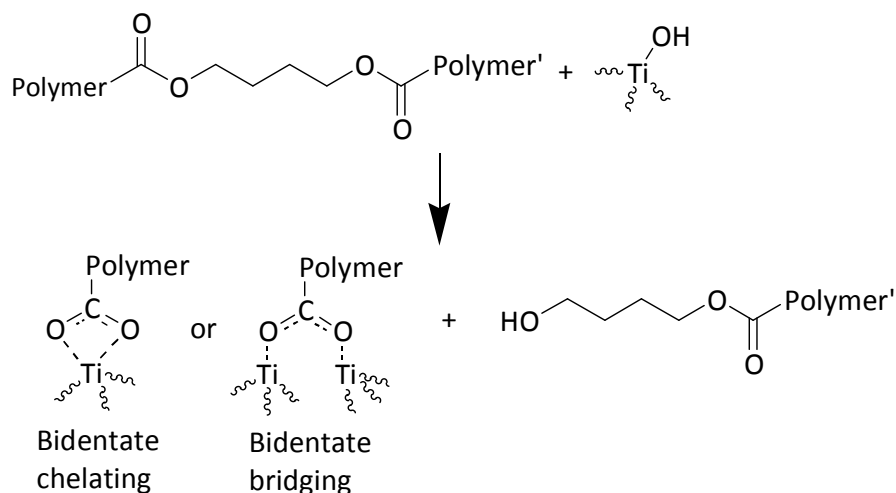


Figure 13. The transesterification reaction

3.4. Applications of Organic-Inorganic Hybrids

The great number of synthetic procedures available for obtaining organic-inorganic structures allows producing materials characterized by a wide range of properties. The choice of the organic and inorganic primary components, which must be guided by the properties that the final materials will need to display, represents the first important step in the development of hybrid materials. Some of the conventional properties of polymeric and inorganic materials are summarized in Table 2.

Table 2. Comparison of the general properties of polymeric and inorganic materials (adapted from [100])

Property	Polymer	Inorganic (MO _x)
Nature of bonds	covalent (plus weak van der Waals and hydrogen bonding)	Ionic or ionic-covalent
Thermal stability	low (<300°C)	high (>>30°C)
Density	0.9-1.2	2.0-4.0
Refractive index	1.2-1.6	1.15-2.7
Mechanical properties	elasticity, plasticity	hardness, strength, fragility
Hydrophobicity	Hydrophilic or hydrophobic depending on functional groups	Hydrophilic
Gas permeability	permeable	low permeability
Electronic properties	insulator	insulator or semiconductor

The choice of the polymer is usually guided by its mechanical and thermal behavior, but, depending on the application of the final hybrid material, other particular properties, such as chemical stability, hydrophobic/hydrophilic balance, biocompatibility and optical properties may be also considered. The inorganic component provides mechanical and thermal stability. In addition, peculiar properties such as biocompatibility, optical properties, magnetic and electronic properties and radiopacity may be taken into account. As already pointed out, the final material properties are not just the sum of those of the primary components. Indeed a large synergy is expected to arise from the close coexistence of the two phases owing to size-domain effects and to the nature of the interfaces.

The extremely high versatility of organic-inorganic hybrids makes this class of materials hypothetically suitable for a huge number of applications in the form of both bulk material and coating. The big effort that academic community and also industry have put into hybrid materials research has resulted in the commercialization of some of these products in different application fields. Some examples of organic-inorganic material applications (either commercial or not) are the following:

- Protective coatings (scratch/abrasive-resistant hard coatings [101,102], anti-corrosion coatings [102], chemical-resistant coatings [103], etc.);
- Super hydrophobic/hydrophilic coatings [104];
- Decorative coatings for glass objects [105];
- UV shielding particles for cosmetic products [106];
- Radiopaque materials [99,107];
- Catalyst (based on enzymes immobilized inside so-gel derived materials) [108];
- Hybrid materials for microelectronics (dielectric parts, flexible optical waveguides, media for photolithography processes) [109,110,111];
- Hybrid materials for micro-optics (diffractive and refractive lenses, interference optical coatings) [112,113];
- Ionic conducting gels for flexible thin film batteries [114];
- Proton-exchange membranes for fuel cells [115,116].

Organic-inorganic hybrids have also been investigated as biomaterials for application in the medical field. Obviously, in this specific case organic and inorganic phase constituents are chosen among biocompatible compounds. Bone tissue repairing represents a great area of interest for the employment of hybrid materials. Generally, synthetic materials implanted into bone defects are encapsulated by a fibrous tissue isolating them from the surrounding bone. Bioactive ceramics, such as sintered hydroxyapatite, in the living body are able to form a bone-like apatite layer at their surface which binds to living bone [117]. Although bioactive ceramics are used clinically as important bone-repairing materials, they are essentially brittle and hence limited in their applications. In this context, sol-gel derived organic-inorganic hybrids have been studied for the production of flexible, elastic bioactive bone-repairing materials. In such hybrids the inorganic phase is usually constituted of silica or titania plus calcium inorganic compounds such CaO [118,119] and CaCO₃ [120] (which promote the apatite layer formation), while PTMO [117] or PDMS [121] are employed as the polymeric phase. In addition, biodegradable polymers such as PLA [120], PCL [122] and poly(hydroxyalkanoate) (PHA) [122], have been chosen as the organic phase, in order to produce tissue-engineered scaffolds for guided bone-regeneration.

Silica-containing hybrid materials have been also investigated in their bulk form as filling composites for dental applications [100]. The filler is constituted by organic reactive monomers embedded in the sol-gel derived silica network. After placement inside the dental cavity, polymerization of organic monomers under blue light is performed during the curing process, and the hybrid material is obtained in situ with minimum shrinkage. Hybrids are advantageous compare to traditional plastic filling composites because they can be designed in order to display tooth-like properties (appropriate hardness, elasticity, and thermal expansion behavior) and they are easy to use by the dentist. Indeed, they easily penetrate into the cavity and harden quickly under blue light. Furthermore, abrasion resistance is significantly enhanced by the presence of the silica inorganic phase.

Besides orthopedic and dental applications, hybrid materials have been also proposed as coating for improvement of compatibility of blood contacting materials. As an example, Osaka et al. performed blood compatibility tests on stainless steel surfaces coated with a PDMS-titania hybrid and showed how platelet adhesion was

inhibited by the presence of this material on stainless steel surfaces. Such hybrid material might be therefore promising for application in the vascular field.

Recently Mazzocchetti et al. have demonstrated that hybrid materials display another very important feature for vascular applications (already pointed out in the previous chapter), i.e. radiopacity. In the hybrid, radiopacity is associated with the inorganic phase, which contains heavy atoms. In a first article published in 2006, organic-inorganic hybrids based on poly(D,L-lactic acid) (PDLLA) and silica were prepared [107]. The synthetic strategy followed proceeded via modification of hydroxyl polymer chain ends with groups bearing triethoxysilane units, as shown in Figure 14.

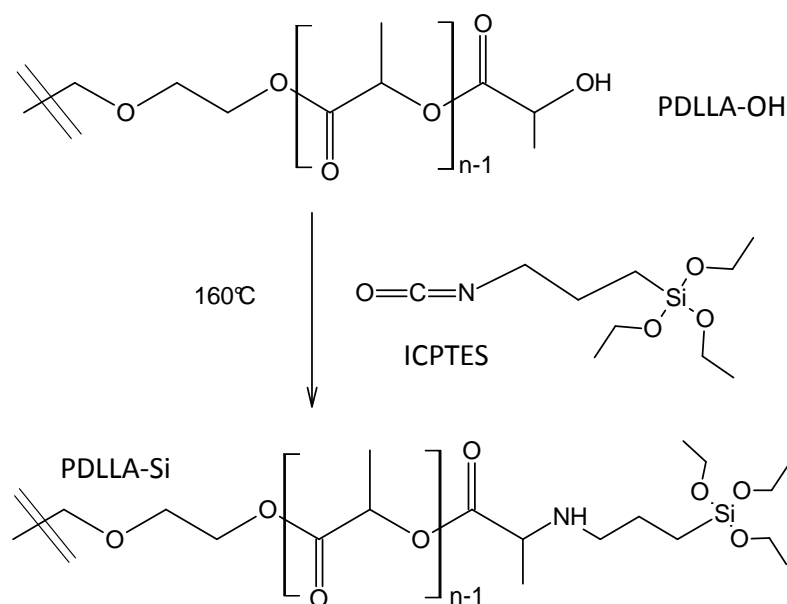


Figure 14. PLLA chain terminals functionalization reaction (polymer chains are shown as half of the whole macromolecule)

In the paper, hybrids obtained starting from different organic to inorganic precursor ratio and applying different thermal treatments are described. All synthesized materials were optically transparent (Figure 15) and the silica particles, observed by AFM, were shown to have nanometric dimensions and to be homogeneously dispersed in the system. Radiopacity of the materials was tested using mammographic equipment. The radiographic image, in Figure 15, showed that the hybrid is bright and well evident against the dark background.



Figure 15. Picture and radiographic image of a PDLLA-SiO₂ hybrid

In a second work of 2008 [99], organic-inorganic hybrids based on PBG and titanium oxide TiO₂ (titania) were synthesized, starting from different ratios of organic to inorganic precursors and varying type of solvent and catalyst amount. The main aim of the work was to study the interactions between organic and inorganic phase.

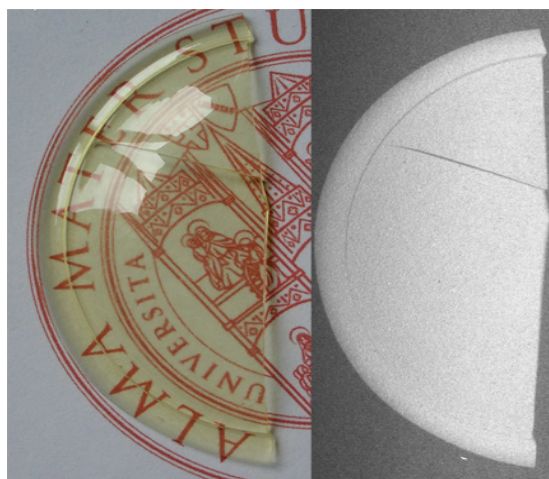


Figure 16. Picture and radiographic image of PBG-TiO₂ hybrid

As previously described in Paragraph 3.3, it was shown that a strong interaction between the polymer and the in situ forming titania was achieved via transesterification of the polymer chain, leading to organotitanium esters connecting organic and inorganic domains. In addition, a characterization of the hybrids regarding their interaction with electromagnetic radiation was performed, and it was shown that PBG-titania hybrids were both transparent and radiopaque (Figure 16), with radiopacity increasing with titania content.

Experimental Part

1. Materials

Poly(1,4-butylene-glycol) (PBG, Aldrich, $\overline{M}_w = 3700$ Da, PDI=2.8), two different poly(ϵ -caprolactone)s (PCLa; Tone 787, Union Carbide, $\overline{M}_w = 75000$ Da, PDI = 4.9. PCLb, Aldrich, $\overline{M}_n = 10000$ Da), poly(L-lactic acid) (PLLA, Lacea H-100-E, $\overline{M}_w = 84000$ Da, PDI = 1.7), poly(D,L-lactic acid) (PDLLA, Resomer R 203 H Boheringer, $\overline{M}_w = 36000$ Da, PDI = 2.6) and poly(dimethylsiloxane) di-carboxypropyl terminated (PDMS, $\overline{M}_n = 28000$ Da, ABCR GmbH) were used as organic hybrid precursor. Poly (trimethylene carbonate) dihydroxy terminated (PTMC, $\overline{M}_n = 17750$ Da, from GPC analysis) was synthesized by ring-opening polymerization (ROP) starting from cyclic trimethylene carbonate (TMC, Boehringer Ingelheim) and propan-1,3-diol ($\geq 99.0\%$, Fluka).

Titanium tetraisopropoxide (TIPT, 97% Aldrich) was employed as hybrid inorganic precursor. Tantalum nanopowder (APS = 50 – 80 nm, Iolitec GmbH) was used for loading organic-inorganic hybrids.

Chloroform ($\geq 99.8\%$, Aldrich), THF (absolute, Fluka), dichloromethane ($\geq 99.9\%$, Aldrich), diethyl ether ($\geq 99.5\%$, Riedel de Haen), concentrated hydrochloric acid (HCl, 37% Aldrich), hydrogen peroxide (Carlo Erba Reagents), smooth muscle growth medium-2 (SmGM-2, Lonza) and Trypan blue solution (Sigma) were employed.

All chemicals and commercial polymers were used without further purification.

2. Synthetic Procedures

2.1. Synthesis of PTMC

PTMC with an average chain length of 100 monomer units was synthesized by the following procedure: 7,5 g of TMC (73,47 mmol) are introduced in a nitrogen-flushed two-necked round bottom flask equipped with a magnetic stirrer. The flask is immersed in an oil bath at 60 °C, and then the melted TMC (mp = 47 °C) is subjected to 3 vacuum/nitrogen cycles, in order to eliminate any traces of water. After cooling to room temperature, 53 μ L of 1,3-propanediol initiator (0,73 mmol) are added to the monomer under nitrogen flux and then the stoppered flask is heated at 120 °C for 7 h.

The product obtained is twice dissolved in chloroform and precipitated into an excess of cool diethyl ether ($T = 0 - 5\text{ }^{\circ}\text{C}$). The recovered polymer is further dried in an oven at $70\text{ }^{\circ}\text{C}$ under vacuum for 12 h in order to eliminate residual solvent. TGA analysis confirms the absence of weight losses attributable to solvent. The final yield, gravimetrically determined, is 90%.

2.2. Synthesis of Hybrids

Hybrids were synthesized starting from TIPT as the inorganic precursor and from different organic precursors, such as PBG, PCL, PDLLA and PDMS. Generally, the polymer and TIPT were dissolved in different weight ratios in the solvent. All hybrid samples synthesized are labeled H-PX, where P stands for the polymer acronym (PBG, PCL, PDLLA, PDMS, etc.) and X is the weight percentage of the polymer in the sol-gel feed.

Synthesis of Polyester-Titania Hybrids

Polyester containing hybrids were synthesized employing the following polymers as organic precursor: PBG, PCLa, PLLA and PDLLA, and starting from different weight ratios ($X = 10, 25, 50$ or 75). As an example, synthesis of hybrid H-PBG50 is described in the following: 1 g of TIPT is added to 2 mL of CHCl_3 (solution 1). In a separate container 1 g of PBG is dissolved in 4 mL of CHCl_3 (solution 2). After complete polymer dissolution, solution 2 is added to solution 1 under vigorous stirring. The obtained clear mixture (solution 3) is then either poured in a Teflon Petri dish to produce a bulk hybrid sample or, alternatively, it is coated on different flat substrates such as aluminum, steel, copper, glass, cellulose acetate, polypropylene (PP) or PTFE sheets. Coating is obtained either by dipping the substrate in the solution, or by casting the solution on the substrate and removing the excess solution with the aid of a sliding glass rod (Doctor Blade Method). After 2 h at room temperature (RT), a transparent solid layer (maximum thickness $10\text{ }\mu\text{m}$) forms on all different substrates. Then the coated samples are thermally treated for 1 h in an oven at $110\text{ }^{\circ}\text{C}$. The bulk “self-standing” hybrids prepared in the Petri dishes, as described above, are aged for 24 h at RT prior to a 2 h oven treatment at $110\text{ }^{\circ}\text{C}$. The procedure followed for the synthesis of the other hybrid material was identical to the one described for HPBG-50.

Polyester containing hybrids were also coated on different textiles. In order to achieve the application of a hybrid coating on textiles, a synthetic procedure analogous to that described above was followed, the only difference being a greater amount of solvent (10 mL vs. 3 mL of CHCl_3) used to dissolve 1 g of hybrid precursors (polymer + TITP). As an example, the procedure to synthesize the H-PBG50 textile coating is described: 0.5 g of TIPT are added to 1 mL of CHCl_3 (solution 1), while in a separate container 0.5 g of PBG are dissolved in 9 mL of CHCl_3 (solution 2). After complete polymer dissolution, solution 2 is added to solution 1 under vigorous stirring and the obtained mixture is allowed to stir for 1 minute (solution 3). Then, small samples (2 cm x 2 cm) of different fabrics (cotton, silk, wool and polyester) are immersed in solution 3, from which they are retrieved after 15 seconds. A portion of solution 3 is also cast on a PTFE sheet in order to obtain the hybrid in the form of a thin self-standing layer, which can be used as reference material for the coatings. Both such samples and the coated textiles are aged for 2 h at RT and further thermally treated for 1 h in an oven at 110 °C.

Synthesis of PTMC-Titania Hybrids

PTMC containing hybrids were synthesized starting from different weight ratios of organic to inorganic precursors ($X = 25, 50$ or 75). The synthesis of H-PTMC50 is reported as an example: 2 mL of CHCl_3 are added to 1.0 g of TIPT under vigorous stirring (solution 1). A solution containing 1.0 g of PTMC in 6 mL of CHCl_3 (solution 2) is slowly added to solution 1. The mixture is stirred for a few minutes to obtain a clear homogeneous solution (solution 3). A thin layer of solution 3 is then cast on a PTFE sheet and other flat substrates (such as aluminum, steel, copper, glass, cellulose acetate or PP) with Doctor Blade technique in order to produce a layer with uniform thickness. After 24 h at room temperature the solid and transparent materials obtained are thermally treated for 1 h in an oven at 110 °C (for the sake of comparison plain titania was also synthesized following the same procedure described above for hybrid synthesis, except for addition of solution 2, which was omitted).

Synthesis of PCLb-Titania and PDMS-Titania Hybrids

PCLb hybrid was synthesized starting from a ratio of organic to inorganic precursor of 50/50 w/w (H-PCLb50); the synthesis procedure was as follows: 2 mL of THF are added to 1.0 g of TIPT under vigorous stirring (solution 1); a solution containing 1.0 g of

PCL in 4 mL of THF (solution 2) is then slowly added to solution 1; the mixture is stirred for a few minutes to obtain a clear homogeneous solution (solution 3). Solution 3 is then cast on Teflon sheet, on PP sheet and on tantalum-coated PP with the Doctor Blade technique, maintaining the blade at 200 μm distance from the substrates. After 24 h at room temperature, all samples are thermally treated for 2 h in an oven at 100 $^{\circ}\text{C}$ under vacuum. PDMS hybrid was synthesized starting from an organic to inorganic precursor ratio of 70/30 w/w (H-PDMS70); the synthetic procedure was the same as that described above for H-PCLb50 except for the two following changes: a) solution 1 contained 0.6 g of TIPT, 2.4 mL of THF and 5.2 μL of HCl (molar ratio HCl:TIPT = 0.06:1), b) solution 2 contained 1.4 g of PDMS in 6 mL of THF.

2.3. Synthesis of PDMS-Titania Hybrids Loaded with Nanoparticles

PDMS-Titania hybrids were synthesized starting from a PDMS to TIPT ratio 80/20 w/w, in the presence of Ta nanoparticles (NP). Loaded hybrid samples are labeled H-TaNP-X, where X represents the weight percentage of the nanoparticles in the final material (X = 1, 2, 5 or 10). The synthesis of hybrid H-TaNP2 is described as an example: 4 mg of Ta nanoparticles and 183 mg of PDMS are added to 3 mL of THF (solution 1) and sonicated for 2 min (Ultrasonic Bath UTA18, Falc). In a separate container 46 mg of TIPT and 1,6 μL of concentrated HCl (molar ratio TIPT:HCl = 10:1) are dissolved in 2 mL of THF (solution 2) and put under stirring. After complete polymer dissolution, solution 2 is added to solution 1 drop by drop. The obtained mixture (solution 3) is sonicated for 10 min and then poured in a Teflon Petri dish to produce a self-standing hybrid sample. The sample is maintained in a desiccator under vacuum until complete solidification. Then the samples are thermally treated for 2 h in an oven at 100 $^{\circ}\text{C}$ under vacuum.

NP-loaded hybrids were also coated on cotton following a synthetic procedure analogous to that described above. Small samples of cotton fabric were immersed in solution 3, from which they are retrieved after 10 seconds. The coated textiles were aged for 2 h at RT in a desiccator under vacuum and further thermally treated for 1 h in an oven at 100 $^{\circ}\text{C}$ under vacuum.

3. Other Procedures

3.1. Extraction Experiments

Extraction experiments were performed on H-PTMCX samples using a Soxhlet extraction apparatus and dichloromethane as solvent. A weighed amount of hybrid was introduced into a porous cellulose extraction thimble and extracted for 4 h with dichloromethane. Then the thimble containing the insoluble fraction was dried under vacuum in a desiccator over P₂O₅ for 24 h and the dried material was gravimetrically quantified. Recovery of the soluble hybrid fraction was carried out by evaporation of the solvent under reduced pressure and its amount was gravimetrically determined after further drying over P₂O₅ under vacuum for 24 h.

3.2. Tantalum Sputtering

Tantalum was deposited on a polypropylene (PP) substrate (PP sheet, 150 μm thick, without any pre-treatment prior to Ta deposition) employing a Bal-Tec MED 010 sputter coater and a Ta sputtering target (99.9% purity, PI-KEM Ltd). Sputtering was carried out in Argon atmosphere (pressure: 8×10^{-3} mbar, current: 120 mA, target-to-substrate distance: 5cm), after evacuation of the sputtering chamber (Ar pressure $< 10^{-4}$ mbar). Superficial oxide layer on Ta target was preliminarily removed by applying a current of 100 mA for 5 min (Ar pressure 8×10^{-3} mbar).

3.3. Cytotoxicity Tests

Cytotoxicity tests were conducted on H-PCLb50 and H-PDMS70 coated samples using human Vascular Wall resident - Mesenchymal Stem Cells (VW-MSCs) derived from human femoral artery [123]. After sterilization under UV light for 2 h (1 h each side) samples were exposed to cell culture medium SmGM-2 for 24 h at 37 °C (RH ≥ 95%, CO₂: 5%). The medium was then recovered and used to incubate for 24 h VW-MSCs, previously seeded (50.000 cells/well) in a 12-well culture plate (Corning Incorporated, Euroclone). After that, cells were detached with 0.25% trypsin-EDTA, diluted in trypan blue solution and both vital and dead cells were counted with a Neubauer hemocytometer. A negative control was run by exposing cells to plain fresh culture medium for 24 h, whilst for positive control cells were exposed to 1 mM H₂O₂ for 2 h

before counting. Five replicates were run for each experiment. Cells were observed using a NIKON Eclipse TS100 inverted microscope.

4. Instrumental Techniques

Infrared (IR) spectra were recorded using a Nicolet 380 FT-IR spectrometer (32 scans from 4000 cm^{-1} to 400 cm^{-1} , resolution: 4 cm^{-1}). Insoluble solid samples were ground with KBr (1 mg sample / 100 mg KBr) and were pelletized under pressure. Soluble samples were dissolved in chloroform and were cast on KBr discs, allowing total solvent evaporation prior to measurement. All samples were dried overnight under vacuum in a desiccator over P_2O_5 before FT-IR measurements.

Differential Scanning Calorimetry (DSC) was carried out in helium atmosphere by using a TA DSC-Q100 (TA Instruments) apparatus equipped with a Liquid Nitrogen Cooling System (LNCS) low-temperature accessory. Samples (about 5 mg) were placed in open aluminum pans and subjected to heating runs from $-100\text{ }^\circ\text{C}$ to $110\text{ }^\circ\text{C}$ at $20\text{ }^\circ\text{C}/\text{min}$. Either quench cooling or controlled cooling at $10\text{ }^\circ\text{C}/\text{min}$ were applied between heating scans. Glass transition temperature values (T_g) were taken at half-height of the glass transition heat capacity step while melting temperature (T_m) was taken at the maximum of the endotherm peak.

Thermogravimetric (TGA) measurements were carried out using a TGA 2950 thermogravimetric analyzer (TA Instruments). Analyses were performed on samples weighing 5-8 mg, from room temperature to $600\text{ }^\circ\text{C}$ / $800\text{ }^\circ\text{C}$ at a heating rate of $10\text{ }^\circ\text{C}/\text{min}$ under air flow.

UV-Vis spectra were recorded on a Cary 1E (Varian) Spectrophotometer in the range 200-800 nm with a scan rate of $600\text{ nm}/\text{min}$. For hybrid coated samples, transparent polypropylene (PP) film ($31\text{ }\mu\text{m}$ thick) was used as the substrate on which a hybrid layer ($4\text{-}6\text{ }\mu\text{m}$ thick) is coated. Transmittance of the coated PP is measured with changing wavelength and λ_{50} is the wavelength at which the transmittance is reduced to less than 50%.

Scanning electron microscopy (SEM) observations were carried out using a Philips 515 scanning electron microscope at an accelerating voltage of 15.0 kV. Samples were fixed with a conductive bi-adhesive tape on aluminum stubs. Sputter coating with gold

was applied to non-conductive samples prior to SEM analysis. SEM pictures were analyzed by means of Zeiss AxioVision 3.0 software.

The *textile sample area* was evaluated through the analysis of its digital picture by means of the Zeiss AxioVision 3.0 software. Hybrid load on textiles was quantified using an analytical electronic Sartorius RC210D balance (reproducibility ± 0.02 mg).

Radiographic images were recorded on a mammographic apparatus (Diamond MGX Instrumentarium Co. Imaging Division) equipped with a radiogenic tube Varian M113SP (experimental parameters: 22 kV, 4 mA/s, 20 cm sample-to-detector distance) and on an angiographic apparatus (OEC 9800 Plus, GE Medical Systems) (experimental parameters: 55 kV, 20 cm sample-to-detector distance). X-ray films were digitized with an EPSON V10 scanner at 300 dpi resolution and obtained images were analyzed by means of ImageJ 1.42q software.

Proton Nuclear Magnetic Resonance ($^1\text{H-NMR}$) spectra were recorded on a Varian Gemini 300 MHz spectrometer using CDCl_3 solutions. Chemical shifts are reported in parts per million referred to CDCl_3 signal.

Gel Permeation Chromatography (GPC) was performed in chloroform (flow rate = 1 mL/min) at 35 °C, using a Viscotek solvent delivery system with a set of two Tosohaas PL Mixed C columns and a Shodex SE 61 refractive index detector. A volume of 100 μL of sample solution in chloroform (5% w/V) was injected. Polystyrene standards were used to generate a calibration curve.

Wide Angle X-ray diffraction measurements (WAXS) were carried out at room temperature with a PANalytical X'Pert PRO diffractometer equipped with an X'Celerator detector (for ultrafast data collection). A Cu anode was used as X-ray source (K radiation: $\lambda = 0.15418$ nm, 40 kV, 40 mA). Data were collected in 2θ range from 2° to 60°.

Atomic Force Microscopy (AFM) characterization of H-PTMCX samples was carried out on a Veeco Nanoscope 3D equipped with a multimode head. Tapping-mode images and phase-contrast images of $1 \times 1 \mu\text{m}$ were collected with Phosphorus (n) doped Si probes (by Veeco) operated near their resonance frequency and scanned at approximately 2 $\mu\text{m/s}$ linear speed. Phase contrast was optimized by changing the tapping-mode amplitude set point. AFM images of tantalum sputtered samples were

carried out on a Veeco Nanoscope IIIa in tapping-mode. Images were collected using a Si probe operated at a resonance frequency of 330 kHz and scanned at a rate of 1 Hz.

Stability of nanoparticle suspensions was evaluated through *Optical Density (OD) vs time* measurements using a Cary 1E (Varian) Spectrophotometer at a fixed wavelength $\lambda = 650$ nm acquiring OD values every 2 s.

Results and Discussion

1. Polyester-Titania Hybrids: Synthesis and Characterization

In an earlier work by Mazzocchetti et al. [99] an organic-inorganic hybrid was prepared via sol-gel process starting from a dihydroxy-terminated polyester (poly[1,4-buthylene glutarate], PBG) and a titanium alkoxide (titanium tetraisopropoxide, TIPT) as titania precursor. In the cited work it was demonstrated that a strong interaction between the polymer and the *in situ* forming titania was achieved via transesterification reaction of the polymer chain, leading to organo-titanium esters connecting organic and inorganic domains (see Introduction, Paragraph 3.3). Since the transesterification reaction does not require the presence of any specific chain end group, in principle any polyester able to dissolve in a good solvent for the titania precursor should be able to lead to hybrid structures such as those earlier observed with dihydroxy-terminated PBG. In this chapter the synthesis and characterization of new hybrids made of titania and polyesters with different solid state behavior, i.e. PCL and polylactic acid (both PLLA and PDLLA), is reported. The results of the characterization study allow obtaining information on the interactions that set between organic and inorganic phases during hybrid synthesis and confirm the hypothesis previously formulated in connection with hybrids containing titania and PBG. Moreover, properties of polyester-based hybrid coated on different substrates are showed, highlighting the extreme versatility of these materials.

1.1. Synthesis and Characterization of Bulk, Self-standing Hybrids

The same procedure formerly adopted by Mazzocchetti et al. for low molecular weight dihydroxy-terminated PBG ($\overline{M}_w = 3700$ Da) was applied in the synthesis of hybrids using high molecular weight polyesters with different solid-state properties as organic phase precursors. Poly[ϵ -caprolactone] (PCLa) was selected due to its low glass transition temperature (T_g around -60 °C) and low melting crystal phase (T_m around 55 - 65 °C) [124], while poly(lactic acid), employed both as poly(L)-lactic acid homopolymer and as poly(D,L)-lactic acid copolymer, has $T_g = 55$ °C and it is glassy at room

temperature. Moreover, PLLA is able to crystallize ($T_m = 185\text{-}215\text{ }^\circ\text{C}$) whereas PDLLA is totally amorphous [124].

The hybrids were produced via sol-gel process in chloroform, a good solvent for both the polymers and the titania precursor employed (TIPT), without the addition of water in the system. Water is required during sol-gel process to promote hydrolysis of the alkoxide groups producing intermediate metal hydroxides, which can then condensate to form the metal oxide network. However, as already pointed out in the Introduction (see Introduction, Paragraph 3.2) it is well established that transition metal alkoxides, hence titanium alkoxides, are highly reactive towards nucleophiles and that they can give rise to uncontrolled fast reactions [82]. As an example, the presence of water in the reaction environment often leads to instantaneous titania precipitation. Takahashi and co-workers demonstrated the possibility to run sol-gel reactions without water addition, using water obtained from air humidity as hydrolysis initiator, thus avoiding any undesired titania precipitation [84]. In a first step, the hybrids were synthesized in this work using a 50/50 (w/w) polymer/TIPT feed ratio. All hybrid samples synthesized are named H-PX, where P stands for the polymer and X is the weight percentage of the polymer in the sol-gel feed.

It is worth noting that, if TIPT reaction during hybrid synthesis does not run to completion, the synthesized materials may contain residual organic products. This point may be clarified with the help of *TGA analysis*, in particular by evaluation of the high temperature solid residue in TGA experiments run in the presence of oxygen. When the hybrid is subjected to TGA in air (up to $T = 600\text{ }^\circ\text{C}$, for example), all carbon-based compounds are oxidized and they volatilize during the scan, while titanium atoms, independent of their initial oxidation state, end up as fully oxidized, i.e. as titanium oxide. The solid residue measured after hybrid thermal degradation may thus reveal the amount of Ti atoms present in the starting material and consequently it yields useful information about the actual composition of the analyzed material. For a given hybrid, the theoretical amount of titania solid residue expected at the end of a TGA scan (SR_{bulk}^{Cal}) can be calculated, on the assumption that during the sol-gel process leading to the hybrid complete hydrolysis and condensation of the inorganic phase precursor has occurred. The value is given by the following equation:

$$SR_{bulk}^{Cal} = \frac{X_{TIPT} \frac{MW_{TiO_2}}{MW_{TIPT}}}{X_{Polymer} + X_{TIPT} \frac{MW_{TiO_2}}{MW_{TIPT}}} \quad [Eq.4]$$

where $X_{polymer}$ and X_{TIPT} are the weight fractions of the organic and inorganic precursors in the feed, and MW_{TiO_2} and MW_{TIPT} are the molecular weights of titania and of TIPT respectively. Comparison of the experimental solid residues for the three hybrids obtained starting from PCLa, PDLLA and PLA as organic phase precursor with the calculated data (reported in Table 3) shows good agreement. This observation suggests that prior to thermogravimetric analysis almost complete hydrolysis of the inorganic precursor has occurred in the hybrid.

Table 3. TGA results for hybrids and for correspondent polymer organic-phase precursors

Sample	TIPT/PTMC In feed (wt.-%)	Titania residue	
		Exp. ^a	Calc. ^b
PCLa	-	<0.5	0
H-PCLa50	50/50	21.2	21.9
PLLA	-	<0.5	0
H-PLLA50	50/50	22.6	21.9
PDLLA	-	<0.5	0
H-PDLLA50	50/50	22.5	21.9

^a Experimental solid residue at 600 °C from TGA experiments run in air.

^b Calculated according to Eq.4, on the assumption that the hybrid precursors have fully reacted before TGA measurement.

Sol-gel of transition metal alkoxides is usually an equilibrium process, driven by several parameters affecting the relative rates of hydrolysis and condensation and unable to go to completeness at RT [78,125,126]. Under thermal treatment, the Ti-OR and Ti-OH groups still present after room temperature ageing can further react releasing ROH and H₂O, both via sol-gel reactions and involving the reactive functionalities provided by polymer chains. Hence TGA results show that upon curing

at 110°C (see Experimental Part, Chapter 2) the hydrolysis reaction is complete and the reaction by-products have been eliminated. Therefore it can be concluded that, within the accuracy of the TGA quantification, the synthetic procedure applied represents a reliable method to produce hybrids with given composition determined by the sol-gel feed.

In order to investigate *organic-inorganic phase interactions*, synthesized hybrids were then analyzed by *FT-IR spectroscopy*. The earlier work by Mazzocchetti et al. on PBG-containing hybrids showed that titanium-driven transesterification leads to formation of a new carbonyl stretching absorption band in the FT-IR spectrum, centered at lower wavenumbers than the traditional ester carbonyl stretching (1535 cm^{-1} vs 1740 cm^{-1}) [99]. This is shown in Figure 17 where the band intensity increases with titania content in the hybrid, reaching around 30% of the classical carbonyl stretching (1740 cm^{-1}) band intensity in the hybrid synthesized starting from 75%-wt of TIPT.

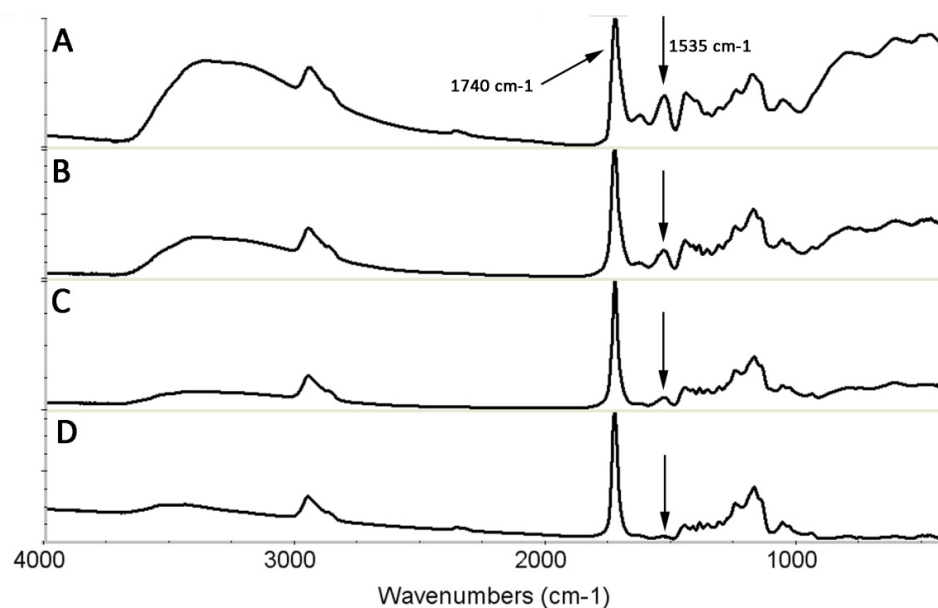


Figure 17. Normalized FT-IR spectra of H-PBGX hybrids: A. H-PBG75, B. H-PBG60, C. H-PBG50 and D. H-PBG25.

It is well known that a carbonyl group complexing an electron-deficient atom shifts its IR-absorption to lower wavenumbers to an extent which depends on the mode of interaction [127,128,129], as depicted in Figure 18.

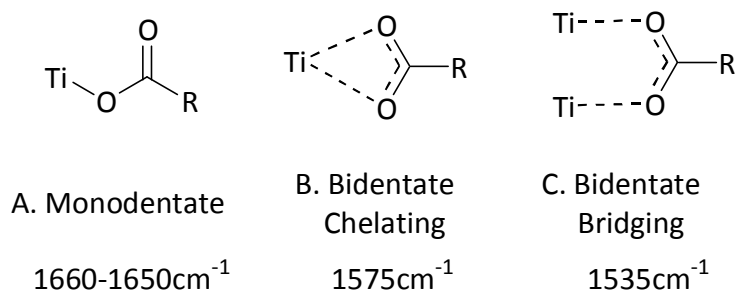


Figure 18. Modes of interaction between a Ti atom and a carbonyl group and correspondent IR-absorption wavenumbers

The mentioned new band observed in PBG-based hybrids [99] was attributed to the stretching of the C=O moiety interacting with the titanium atom in agreement with previous assignments [84]. Figure 19 compares the FT-IR spectra of the presently synthesized hybrids (H-PCLa50, H-PLLA50 and H-PDLLA50) focused on the carbonyl stretching absorption range, with those of the respective plain polymers.

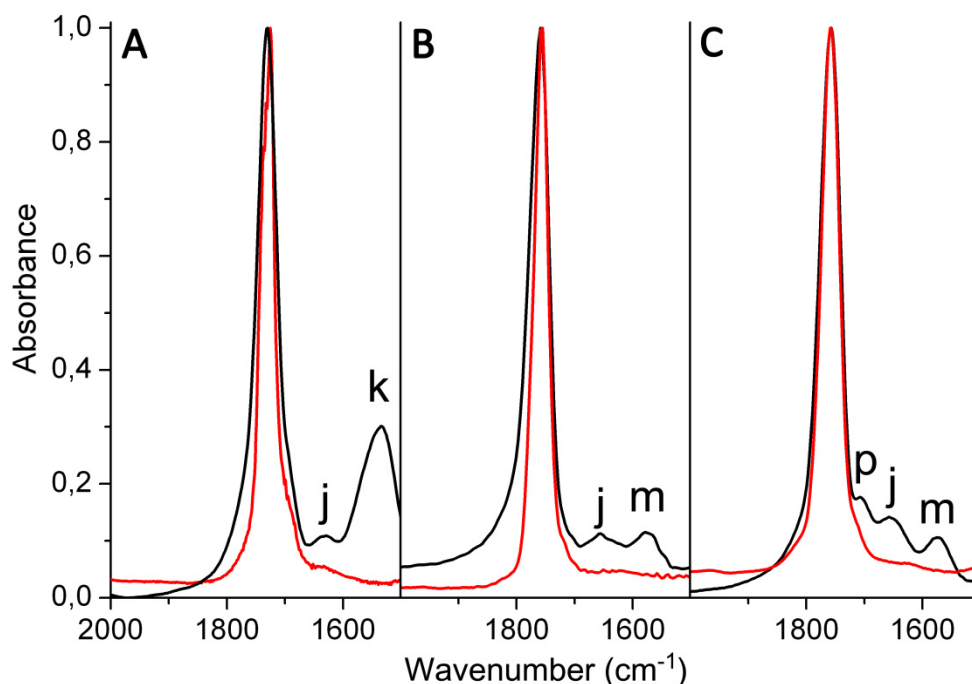


Figure 19. FT-IR spectra, focused on the $1500-2000\text{ cm}^{-1}$ carbonyl region of: A. PCLa (red) and H-PCLa50 (black); B. PLLA (red) and H-PLLA50 (black); C. PDLLA (red) and H-PDLLA50 (black). Letters identify peaks at different wavelength: j. $1650-1660\text{ cm}^{-1}$; k. 1535 cm^{-1} ; m. 1575 cm^{-1} ; p. 1700 cm^{-1}

Besides the expected carbonyl absorption at 1740 cm^{-1} , all hybrids in Figure 19 display a new band in the range $1660-1650\text{ cm}^{-1}$ (absorption j) that, according to the

literature [129], can be attributed to monodentate titanium ester carbonyl (Figure 18-A). The presence of such a band, not detected in the previously synthesized H-PBGX hybrids, may owe to the high molecular weight of the present polymers that may hinder further carbonyl coordination expansion after transesterification. Moreover all hybrids show a second signal at even lower wavenumbers, i.e. absorption *k* at 1535 cm^{-1} and absorption *m* at 1575 cm^{-1} .

The new band (*k*) at 1535 cm^{-1} in the FT-IR spectrum of H-PCLa50 (Figure 19-A) lies at the same wavenumber as the absorption found in the spectrum of the previously analyzed H-PBG50 [99]. Accordingly absorption *k* in H-PCLa50 is attributed to the organo-titanium ester carboxylate that additionally interacts with titanium atoms through carbonyl oxygen, giving rise to a bidentate bridging structure [84], as sketched in Figure 18-C. The presence of the 1535 cm^{-1} band in the spectrum of the hybrid containing the high molecular weight polyester PCLa is a further confirmation that the chemical bond forms via chain scission at the ester linkage and that this bond formation is not linked to the chain end functionalization of the polymer.

The spectra of H-PLLA50 and H-PDLLA50 (Figure 19-B and Figure 19-C respectively) show the additional absorption *m* at 1575 cm^{-1} , i.e. at slightly higher wavenumbers than absorption *k* of hybrid H-PCLa50 (Figure 19-A). According to the literature, absorption *m* in the two PLA-based hybrids might be ascribed to a bidentate chelating structure, as depicted in Figure 18-B. Worth noting is that in the case of H-PDLLA50 a third new band at 1700 cm^{-1} is observed (absorption *p*), that can be attributed to some free carboxylic acid moiety possibly formed during the transesterification process.

The different FT-IR behavior of hybrids H-PLLA50 and H-PDLLA50 with respect to hybrids H-PBG50 and H-PCLa50 may be due to the presence, in the former hybrids, of the methyl group in α position to the carboxyl moiety (see Figure 20). The sterical hindrance of the α substituent inhibits to some extent transesterification reaction on the carbonyl, as evidenced by the lower intensity of bands *j+m* in PLA-hybrids with respect to bands *j+k* in H-PCLa50. Moreover, when titanium coordination expansion occurs, the mode of interaction is affected by the presence of a bulk group close to the carboxyl moiety and the bidentate chelating structure (band *m*) is preferred to a bidentate bridging one (band *k*).

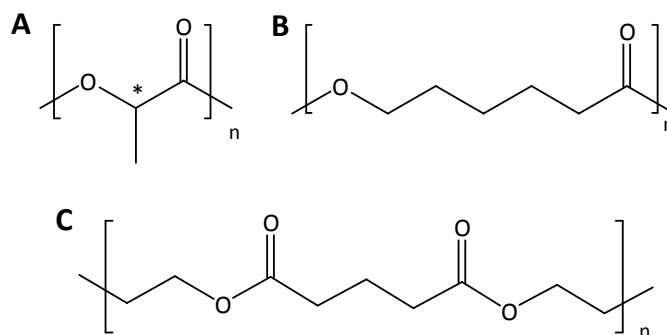


Figure 20. Chemical structure of A. PLA, B. PCL, C. PBG

With the aim of confirming that the observed new bands in PLA containing hybrids originate from the interaction between organic and inorganic components, two new hybrids with higher inorganic content were investigated, namely H-PDLLA25 and H-PDLLA10, whose FT-IR spectra are reported in Figure 21.

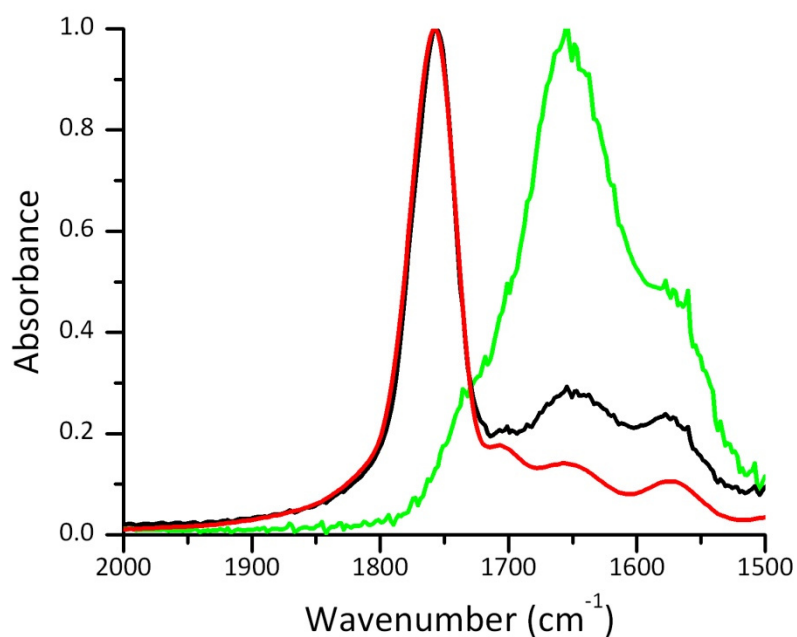


Figure 21. FT-IR spectra, focused on the 1500–2000 cm⁻¹ carbonyl region of H-PDLLA50 (red); H-PDLLA25 (black) and H-PDLLA10 (green). Spectra are normalized with respect to the intensity of the main carbonyl stretching signal, i.e. 1740 cm⁻¹ for H-PDLLA50 and H-PDLLA25, 1650 cm⁻¹ for H-PDLLA10

For the sake of comparison, the spectrum of H-PDLLA50 (same as in Figure 19-C) is also displayed in the figure. Spectra are normalized with respect to the intensity of the main carbonyl signal, which is 1740 cm⁻¹ for H-PDLLA50 and H-PDLLA25, and 1650 cm⁻¹ for H-PDLLA10. With increasing titania content a clear increase of intensity of the new

bands in the range 1500 - 1720 cm^{-1} is observed, showing that the new signals are titania related. It is clear that the new bands grow at the expense of the organic ester absorption (1740 cm^{-1}) which is totally absent in the H-PDLLA10, thus confirming the involvement of polyester carboxylate groups in the interaction with titanium atoms.

The *chain mobility and phase behavior* of the polymeric components of the hybrids was investigated by DSC. Table 4 compares the results of DSC measurements on H-PCLa50, H-PLLA50 and H-PDLLA50 with those of the respective plain polymers (PCLa, PLLA and PDLLA). For the sake of comparison, Table 4 also reports DSC data of the previously synthesized hybrid H-PBG50 (see ref. [99]).

Table 4. Thermal properties of hybrids and of the correspondent polyester precursors, from DSC on quench-cooled samples

Sample	T_g (°C)	ΔT_g^a (°C)	ΔC_p (J/g·°C)	T_m (°C)	ΔH_m (J/g)
PCLa	-63	7	0.13	56	71
H-PCLa50	-65	10	0.39	-	-
PLLA	70	5	0.22	163	36
H-PLLA50	64	21	0.18	158	24
PDLLA	51	5	0.57	-	-
H-PDLLA50	46	13	0.27	-	-
PBG	-72	8	0.68	13	44
H-PBG50	-61	12	0.40	-	-

^aGlass transition width.

Analysis of the DSC data shows that none of the polyesters containing a linear monomer (PCLa and PBG) leads to hybrids containing a crystal phase, although both plain polymers are easily crystallizable in identical experimental conditions. Conversely, PLLA develops crystallinity in hybrid H-PLLA50. The different behavior observed can be attributed to the different ability of the “linear” polyesters and of PLLA to interact with Ti atoms, which has been discussed above in connection with the FT-IR results. Owing to the presence of a methyl group close to carbonyl, PLLA interacts with Ti to a lower degree thus maintaining its crystallizing ability in the hybrid, whereas crystallization of PCLa and PBG is prevented by the strong interaction between these polymers and the inorganic phase. A similar behavior has been

previously reported not only for PBG-containing hybrids [99] but also for silica-based hybrids containing a crystallizable polymer [107,130,131,132], where crystallization of the polymeric component was found to be strongly reduced or even totally inhibited owing to organic-inorganic phase interaction.

As concerns the glass transition of the hybrids, previously studied silica ceramers synthesized from end-functionalized precursors [107,130,131,132] showed an increase of T_g of the polymer component upon hybrid synthesis, that reflects a decrease of mobility of the polymer chains whose ends are locked into the silica network. Conversely, the T_g data for H-PCLa50, H-PDLLA50 and H-PLLA50 in Table 4 show an opposite trend, with T_g being lower in the hybrids than in the respective precursor polymers. In the present hybrids a degree of chain anchoring by the titania phase can be reasonably expected owing to the aforementioned polymer-inorganic phase interactions. However, it is worth noting that the molecular weight of the polymeric phase decreases as a consequence of the transesterification reactions occurring during hybrid synthesis, and this leads to an opposite effect on T_g . The interplay of the two phenomena determines the final hybrid T_g value. Table 4 also shows that the transition width (ΔT_g) is larger in the hybrids than in the respective polymers, implying that the polymer-titania interactions lead to broadening of the relaxation time distribution, as expected.

1.2. Hybrid Coating on Flat Surfaces

The versatility of the synthesized hybrids in yielding materials with different hardness and stiffness, and the particularly mild and easy conditions required to carry out the sol-gel process [80] make this class of products excellent candidates to be applied as coating layers on a wide variety of substrates. In this thesis hybrids made of PBG [99], PCLa, PLLA or PDLLA as the organic phase, and titania as the inorganic phase precursor were applied as coating layers on different flat substrates.

As displayed in Figure 22 for H-PDLLA50 as an example, hybrids with different formulation (polymer type, polymer/TIPT feed ratio, precursors/solvent ratio) can be easily applied (by casting the solution on a flat substrate or dipping a substrate in the reactive solution) to a range of different materials such as aluminum, steel, copper,

glass, cellulose acetate and polypropylene. It is clearly observed that when the hybrid is cast on a transparent substrate the resulting coated material maintains transparency to visible light. This is mainly due to the nanometric dimension of titania domains that do not scatter radiation with wavelength in the range of visible light [77].

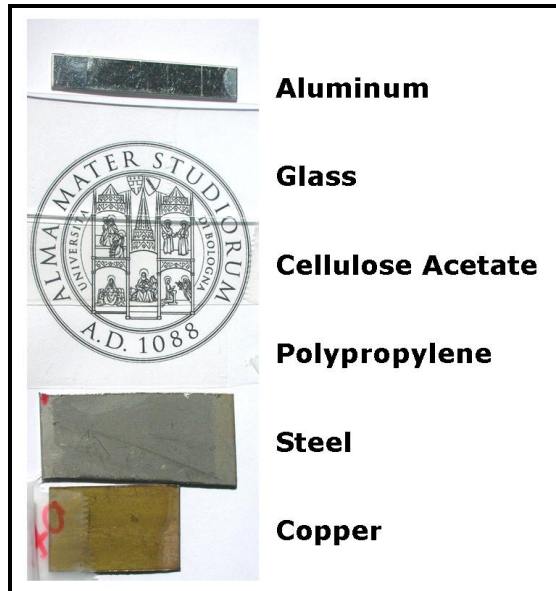


Figure 22. Hybrid H-PDLLA50 cast on different substrates. Application on transparent substrates outlines coating transparency to visible light

Transparency is maintained up to high titania loads, as demonstrated in Figure 4 by the hybrid H-PBG15, produced starting from a feed ratio polymer/TITP = 15/85, that contains more than 60% by weight of titania.

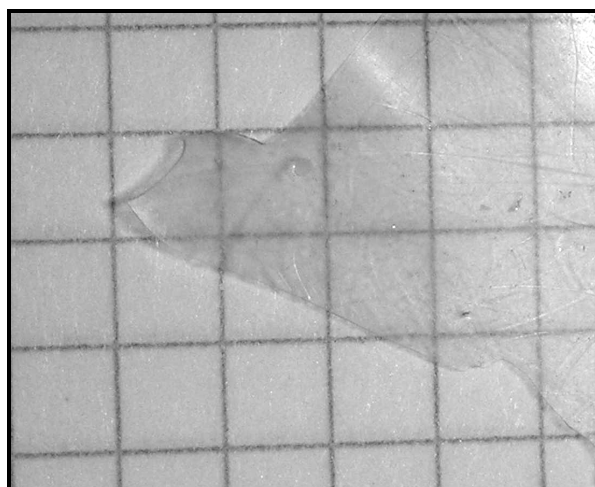


Figure 23. Hybrid H-PBG15 in bulk is transparent to visible light despite the high titania content ($\text{TiO}_2=61.4\%$)

Hybrids show good adhesion towards all surfaces on which they have been coated in this study (plastics, metals, glass) except to Teflon, a substrate from which they can be easily peeled off. The latter support was thus used to produce very thin self-standing hybrid layers, whose thickness (around 10 μm) is comparable to that of the coating layers applied to plastics, metals and glass. These self-standing thin hybrids, that are the reference materials for the coatings, were characterized by FT-IR, DSC and TGA, and no substantial differences between such samples and the previously discussed bulk materials (see Results and Discussion, Paragraph 1.1) were observed.

The *hardness* of hybrid coatings was evaluated on samples coated on aluminum through pencil hardness method (standard ASTM test method D3363, [133]), that determines the hardest pencil which does not fracture or gouge the coating. Pencil hardness results for synthesized hybrid are reported in Table 5. The results show that hardness increases in the order H-PCL50 < H-PBG50 < H-PDLLA50 < H-PLLA50. The mechanical behavior of the synthesized hybrids at room temperature is likely to reflect the material thermal properties and it can be rationalized taking into account the T_g values in Table 4 showing that PCL and PBG are rubbery at RT, while the two PLAs are glassy.

Table 5. Pencil hardness values for hybrid coatings

Sample	H-PCLa50	H-PLLA50	H-PDLLA50	H-PBG50
Pencil hardness ^a	< 6B	3H	HB	6B

^aMeasured according to ASTM D3363, on hybrids coated on aluminum plates

Moreover, H-PLLA50 also contains a crystal phase that enhances hardness of this hybrid with respect to that of H-PDLLA50. The present results suggest that it is possible to tune hybrid mechanical properties through selection of a polymeric phase with suitable thermal properties.

UV-Vis absorption properties of hybrids in the form of thin layers coated on transparent polypropylene (PP) sheet (31 μm thick) were also tested. As an example, Figure 24 shows UV-Vis transmittance spectra of three PBG hybrids with different titania content, namely H-PBG75, H-PBG50 and H-PBG25, coated on PP. For the sake of

comparison, the spectrum of plain PP is also reported, showing transmittance higher than 90% along all the UVB/UVA range ($280 < \lambda < 400$ nm). In the same frequency range, hybrids H-PBG75, H-PBG50 and H-PBG25 are able to cut off a large fraction of the UV radiation. In particular, H-PBG50 and H-PBG25 layers ($5 \mu\text{m}$ and $4 \mu\text{m}$ thick, respectively) cast on PP are completely opaque to UV radiation up to $\lambda = 325$ nm, i.e. over the whole so-called UVB range ($280 - 315$ nm) [134]. Although UVB rays represent a small fraction of the extraterrestrial solar radiation, due to their high energy they are responsible for most of the harmful effects of exposure to sun light [135]. The synthesized hybrids are also able to cut off a large part of the UVA spectrum, i.e. the UV-A2 range [134]. In particular, for wavelengths lower than 345 nm the transmitted radiation intensity is reduced down to 50%.

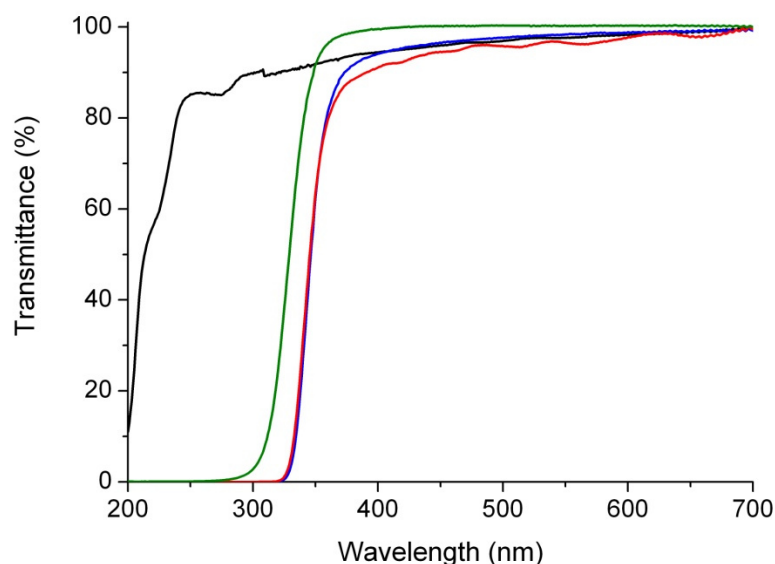


Figure 24. Comparison of UV-Vis spectra of PP sheet ($31 \mu\text{m}$ thick, black) with those of PP sheet coated with: H-PBG75 ($6 \mu\text{m}$ thick coating, red), H-PBG50 ($5 \mu\text{m}$ thick coating, blue) and H-PBG25 ($4 \mu\text{m}$ thick coating, green)

It is worth noting that although the titania content in H-PBG75 is rather small (75%-wt of PBG and 25%-wt of TIPT in the feed correspond to about 9%-wt of titania in the final hybrid) a mere $6 \mu\text{m}$ thick layer of this hybrid is able to halve the intensity of UV radiation with $\lambda \leq 330$ nm.

It can be concluded that the synthesis of new titania-containing hybrids where the organic phase is constituted by different polyesters such as PCL, PDLLA and PLLA provides further evidence that transesterification of ester moieties by titanium atoms leads to formation of the organo-titanium ester, resulting in very strong interaction between the hybrid organic and inorganic domains, as previously reported for PBG-containing hybrids [99]. The occurrence of this transesterification reaction allows obtaining Class II hybrid materials starting from any kind of polyester, that doesn't need to be pre-functionalized in order to react during the sol-gel process. Hybrids obtained from such diverse polyesters display different properties, which depend on the starting polymer characteristics and on the inorganic phase content. They can thus be applied as coatings in different fields, according to the degree of stiffness required by the specific application. Hybrids coated on transparent substrates show their intrinsic optical transparency and their ability to completely block UV radiation in the range UVB and UV-A2.

2. Polycarbonate-Titania Hybrids: Synthesis and Characterization

In the previous chapter it has been demonstrated how in polyester-titania hybrids strong interactions between organic and inorganic phases can be obtained without the need of preliminary functionalization of polymer chain ends. Hybrids have been obtained employing different polyesters, such as PCL, PLLA and PDLLA. In such hybrids interactions between organic and inorganic phase are ascribed to organotitanium ester moieties produced by transesterification reactions of the polyester chain, promoted by Ti atoms acting as Lewis acids. Besides polyesters, also polycarbonates are able to undergo transesterification reactions and the literature offers several examples of the use of titanium alkoxides as catalysts for transesterification of carbonates [136,137] and polycarbonates [138,139]. In this chapter the suitability of aliphatic polycarbonates to enter titania-containing hybrids as organic phase precursors is investigated. The aim of this work is to verify the hypothesis that interconnections between organic and inorganic components may arise from transesterification reactions concomitant with the sol-gel process. This work describes in particular the synthesis of hybrid materials containing poly(trimethylene carbonate) (PTMC) and titania in different weight ratios. The spectroscopic, structural and thermal properties

of the obtained hybrids are investigated with the aim of understanding the type of polymer-titania interactions that come into play in the system.

2.1. Synthesis and Characterization of the Organic Phase Precursor PTMC

A well-established procedure to synthesize PTMC is the ring opening polymerization (ROP) of cyclic trimethylene carbonate (TMC) monomer, which can be conducted with different catalysts and initiators, such as organometallic compounds of tin [140,141] and aluminum [142,143], alcohols [144,145] and enzymes [146,147,148]. In particular Sepulchre et al. investigated the synthesis of PTMC via bulk ROP using two different diols as nucleophilic initiators: 1,3-propanediol and 4-(hydroxymethyl)benzyl alcohol [149]. When diols are employed the polymerization can proceed at both sides of the initiator molecule and the final product is a dihydroxy terminated polymer chain (Figure 25). Moreover, the molecular weight of the synthesized polymer can be controlled by choosing the appropriate monomer to initiator molar ratio, thanks to the pseudo-living character of the process [149].

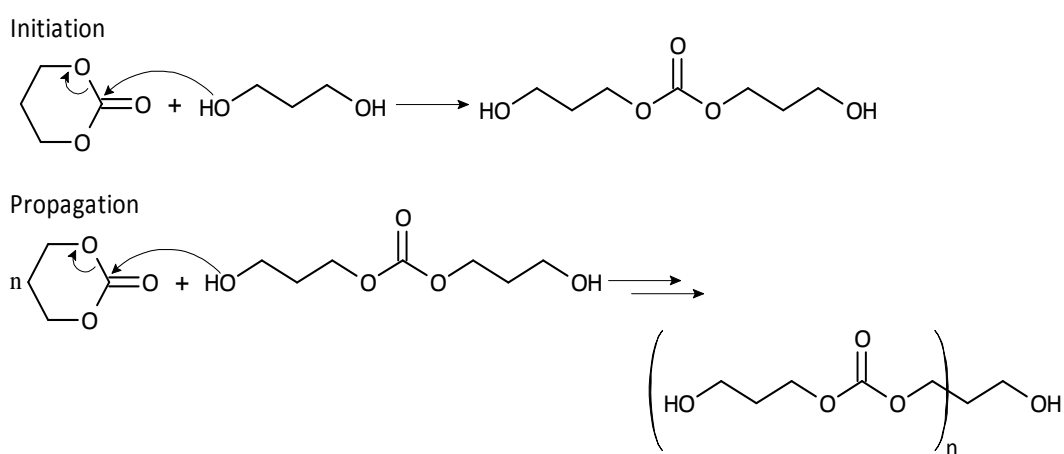


Figure 25. Mechanism of polymerization of PTMC by ROP of TMC initiated by 1,3-propanediol

In the present study 1,3-propanediol was chosen as initiator not only because it yields dihydroxy-terminated PTMC, but also because of its molecular structure. Indeed the initiator becomes unidentifiable in the final polymer structure owing to its identity to part of the TMC molecule. The polymerization was conducted in this work (as described in the Experimental Part) starting from a monomer to initiator ratio of 100,

with the aim of obtaining dihydroxy-terminated PTMC with an average molecular weight of approximately 10 kDa.

The synthesized PTMC was analyzed by means of $^1\text{H-NMR}$. Figure 26 compares $^1\text{H-NMR}$ spectra of PTMC before (A) and after purification (B). The spectrum of the as-polymerized *unpurified PTMC* is collected in order to estimate the percentage of monomer conversion and average molecular weight of the polymer before purification. The spectrum in Figure 26-A shows chemical shifts that are in perfect agreement with the dihydroxy-terminated PTMC structure [149]: partially overlapped signals in the range $\delta = 4.4 \text{ ppm} - 4.0 \text{ ppm}$ are attributed to protons of the methylene group adjacent to the carbonate group, belonging to chain terminal units (*c*) and to internal repeating units (*d*). In the range $\delta = 2.2 \text{ ppm} - 1.8 \text{ ppm}$, partially overlapped signals attributed to protons of the “central” methylene group, belonging to terminal chain units (*b*) and to internal repeating units (*e*), are observed. Finally, at $\delta = 3.7 \text{ ppm}$ the triplet corresponding to protons of the methylene group next to OH terminal functionality (*a*) is present. Besides the typical PTMC signals, the spectrum also shows a triplet in the range $\delta = 4.5 \text{ ppm} - 4.4 \text{ ppm}$, attributed to the presence of unreacted TMC monomer units in the unpurified polymer. Indeed the TMC monomer should show signals at $4.5 \text{ ppm} - 4.4 \text{ ppm}$ (*f*) and at $2.2 \text{ ppm} - 2.1 \text{ ppm}$ (*g*), as reported in literature [149]. In the present case signal (*g*) is not visible because it is hidden by (*b*) and (*e*) signals of PTMC.

The percent monomer conversion can be calculated from the PTMC and TMC signals in Figure 26 according to the following equation:

$$C_{TMC} = \left(1 - \frac{I_f}{I_f + I_{c+d} + I_a} \right) \cdot 100 \quad [\text{Eq.5}]$$

where I_f is the integral value of the signal corresponding to the protons of TMC methylene group close to the carbonate moiety (*f*), while I_{c+d} and I_a stand for integral values of signals attributed respectively to protons of methylene groups next to carbonate moieties (*c+d*) and protons of methylene groups close to OH chain terminals

(a). The calculated value of monomer conversion is 98.4%, which should theoretically correspond to an average molecular weight \overline{M}_n of 10110 Da.

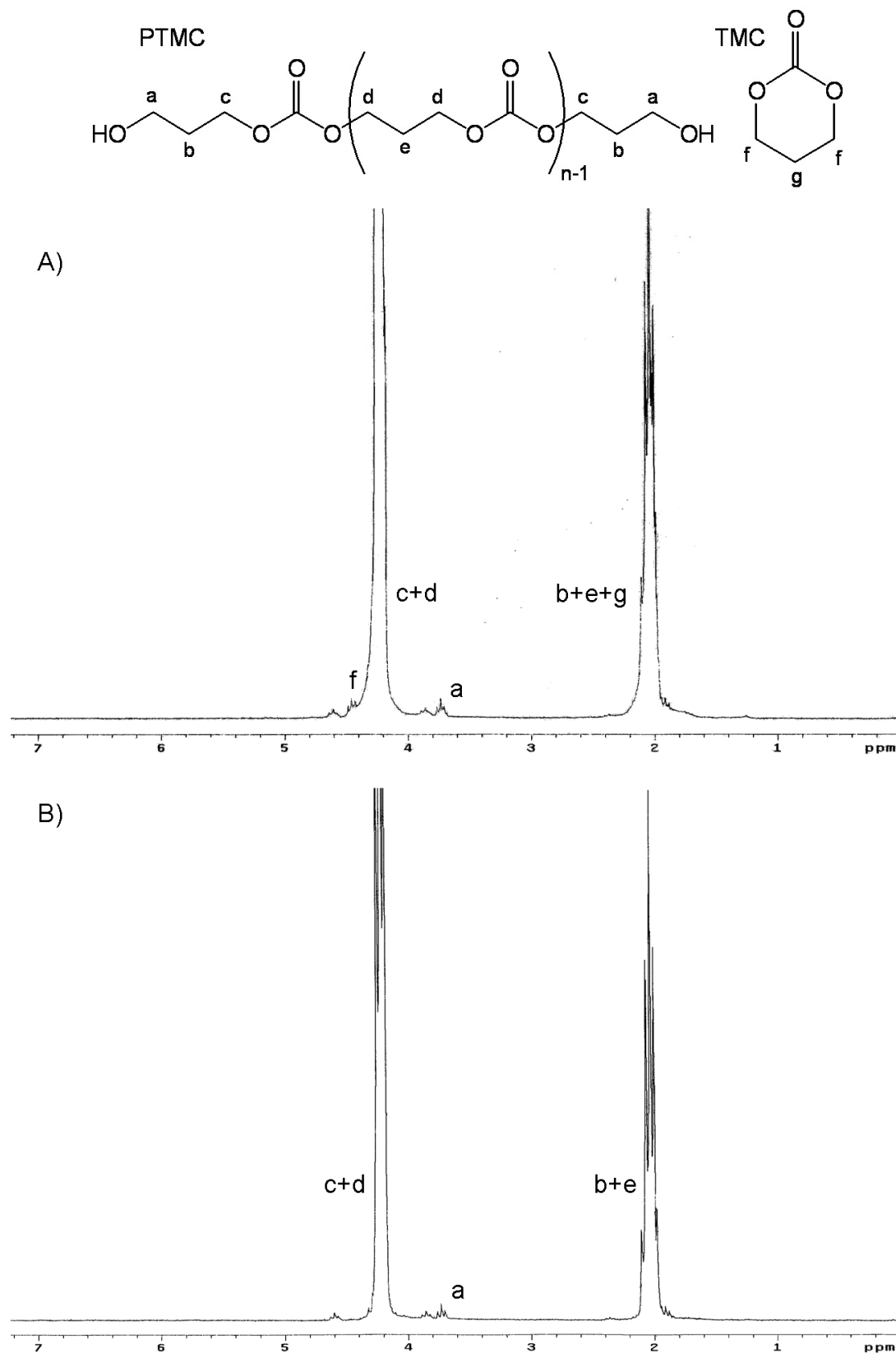


Figure 26. ^1H NMR spectra in the 0 - 7 ppm spectral window with peak attribution. A. unpurified PTMC, B. purified PTMC

This value can be compared with the actual \overline{M}_n value that can be derived from ^1H -NMR signal areas. Signal (*a*) is not affected by polymer chain length, therefore it is taken as an internal reference for the evaluation of the polymer \overline{M}_n .

By comparison of the (*a*) signal area with that of the signal (*c+d*), whose integral directly depends on the number of repeating TMC units in the chain, the average molecular weight is obtained as:

$$\overline{M}_n = \left(\frac{I_{c+d}}{I_a} \cdot MW_{TMC} + MW_{PD} \right) \cdot C_{TMC} \quad [\text{Eq.6}]$$

where MW_{TMC} and MW_{PD} are the molecular weights of TMC and 1,3-propanediol respectively. The \overline{M}_n value obtained from Eq.6 is 10418 Da, in good agreement with the expected one based on the observed monomer conversion (10110 Da).

As concerns *purified PTMC*, whose ^1H -NMR spectrum is reported in Figure 26-B, no signals associated with the presence of residual TMC monomer are observed, confirming the efficiency of the purification procedure employed (see Experimental Part, Paragraph 2.1). The average molecular weight \overline{M}_n of purified PTMC, calculated from Eq.6, is 12132 Da, while \overline{M}_n from GPC analysis is 17750 Da (polydispersity index $PI = 2.44$). Both \overline{M}_n values are significantly higher than that expected from the monomer to initiator ratio employed and this difference can be attributed to the loss of low molecular weight oligomers during product purification and, in the case of GPC analysis, to the use of polystyrene (PS) standards for column calibration.

Purified PTMC was also analyzed by FT-IR spectroscopy and the obtained spectrum, reported in Figure 27 closely agrees with those available in the literature [150,151]. PTMC shows characteristic bands at 1745 cm^{-1} and 1243 cm^{-1} , attributed respectively to carbonate C=O stretching and carbonate C-O stretching vibrations, and a band at 792 cm^{-1} due to the stretching vibration of O-C-C bonds.

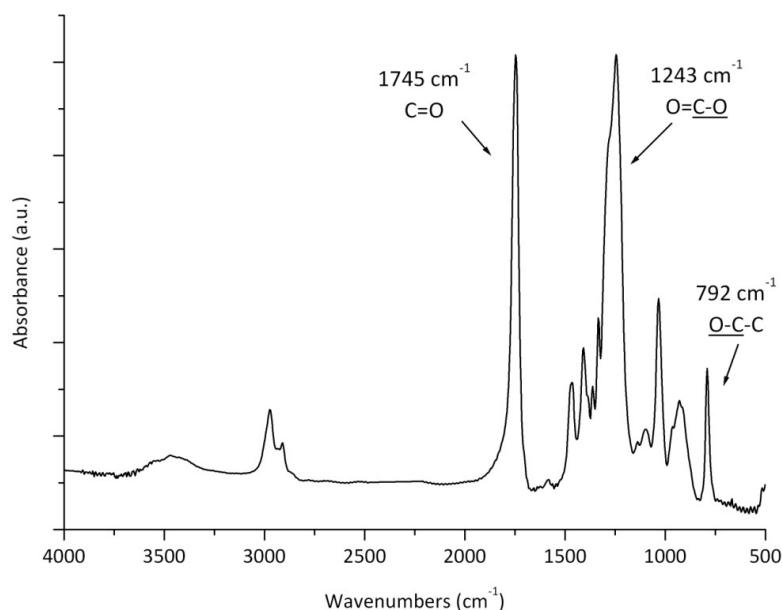


Figure 27. FT-IR spectrum of synthesized PTMC in the range 4000 cm^{-1} - 500 cm^{-1} with band attribution

DSC analysis of PTMC showed that the polymer is totally amorphous with glass transition at $T_g = -18\text{ }^\circ\text{C}$ and an associated specific heat increment $\Delta C_p = 0.5\text{ J/g}\cdot^\circ\text{C}$. These results are in good agreement with those reported in the literature [152].

2.2. Synthesis of PTMC-Titania Hybrids and Study of Phase Interactions

Organic-inorganic hybrids were synthesized via sol-gel method using the purified PTMC and the Titania precursor TIPT. Like in the synthesis of polyester-containing hybrids, precursors were dissolved in chloroform and, in order to keep a better control on TIPT sol-gel reactions during hybrid formation, no water was added to the reaction mixture, on the assumption that air humidity can provide the water amount required for hydrolysis to occur [84].

With the aim of investigating the effect of increasing inorganic phase content on organic-inorganic interactions and on the properties of the final hybrid materials, PTMC-titania hybrids were synthesized starting from different weight ratios of organic to inorganic precursor, i.e. 25/75, 50/50 and 75/25. All hybrid samples synthesized are labeled H-PX, where P stands for the polymer acronym and X is the weight percentage of the polymer in the sol-gel feed.

As already discussed for polyester-containing hybrids, TGA can help understanding if TIPT hydrolysis has run to completion, through analysis of the final solid residue at 600 °C. Hence TGA analyses were carried out on PTMC-Titania hybrids performing heating scan from RT to 600 °C under air flux. TGA residue at 600 °C, reported in Table 6, can be compared with two limit situations, as illustrated in Figure 28. One limit case stands on the assumption that the sample is a hybrid composed of titania and polymer only, i.e. a hybrid resulting from sol-gel reaction pushed to completion with total elimination of reaction by-products. In this case, the theoretical solid residue (SR_{bulk}^{Cal}) is calculated using Eq.4 as already explained in the previous chapter.

Table 6. TGA results for hybrids and for PTMC organic-phase precursor

Sample	TIPT/PTMC In feed (wt.-%)	Titania residue	
		Exp. ^a	Calc. ^b
PTMC	-	<0.5	0
H-PTMC75	25/75	10	9
H-PTMC50	50/50	23	22
H-PTMC25	75/25	48	46

^a Experimental solid residue at 600 °C from TGA experiments run in air.

^b Calculated according to Eq.4, on the assumption that the hybrid precursors have fully reacted before TGA measurement.

In the second limiting case, the theoretical solid residue is calculated as if a completely unreacted TIPT and PTMC mixture were thermally degraded during the TGA scan under air purge.

In this circumstance, PTMC is not the only organic component that can thermally degrade upon heating, because the alkoxide groups belonging to TIPT can also be oxidized. In this case the solid residue ($SR_{bulk}^{B, Cal}$) is calculated according to the following equation:

$$SR_{bulk}^{B, Cal} = \frac{X_{TIPT} \frac{MW_{TiO_2}}{MW_{TIPT}}}{X_{Polymer} + X_{TIPT}} \quad [Eq. 7]$$

where $X_{Polymer}$ and X_{TIPT} are weight fractions of organic and inorganic precursors in the feed and MW_{TiO_2} and MW_{TIPT} are molecular weights of titania and TIPT respectively.

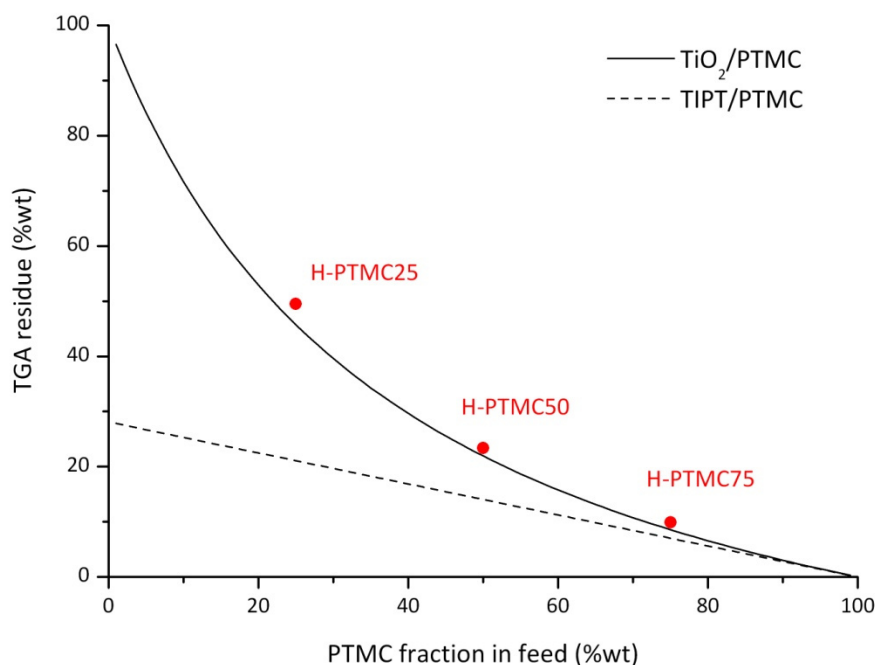


Figure 28. TGA experimental solid residue of H-PTMCX hybrids plotted as a function of PTMC precursor (TIPT) in the feed (red points). The drawn lines correspond to the titania solid residue calculated assuming that, before the TGA experiment, the sol-gel precursor have fully reacted (solid line) or are completely unreacted (broken line)

Figure 28 compares the experimental solid residue of the synthesized hybrids (characterized by different TIPT weight fraction X_{TIPT}) in the feed with the behaviors predicted by Eq. 4 and Eq. 7 discussed above. A good agreement between experimental values and the prediction of Eq. 4 is observed. This result shows that all analyzed hybrids are essentially composed of PTMC and titania, implying that within the accuracy of TGA quantification, prior to thermogravimetric analysis, hydrolysis of the inorganic precursor and removal of the reaction by-products during the thermal treatment at 110°C is complete. It is therefore confirmed that the synthetic procedure adopted is a reliable and easy method to obtain hybrids with controlled composition.

All synthesized hybrids were solid self-standing transparent films. The obtainment of solid materials with given shape and rigidity, while the starting compounds are a viscous and tacky polymer and a liquid inorganic precursor, suggests that significant

interactions have been established between organic and inorganic phases in the hybrids.

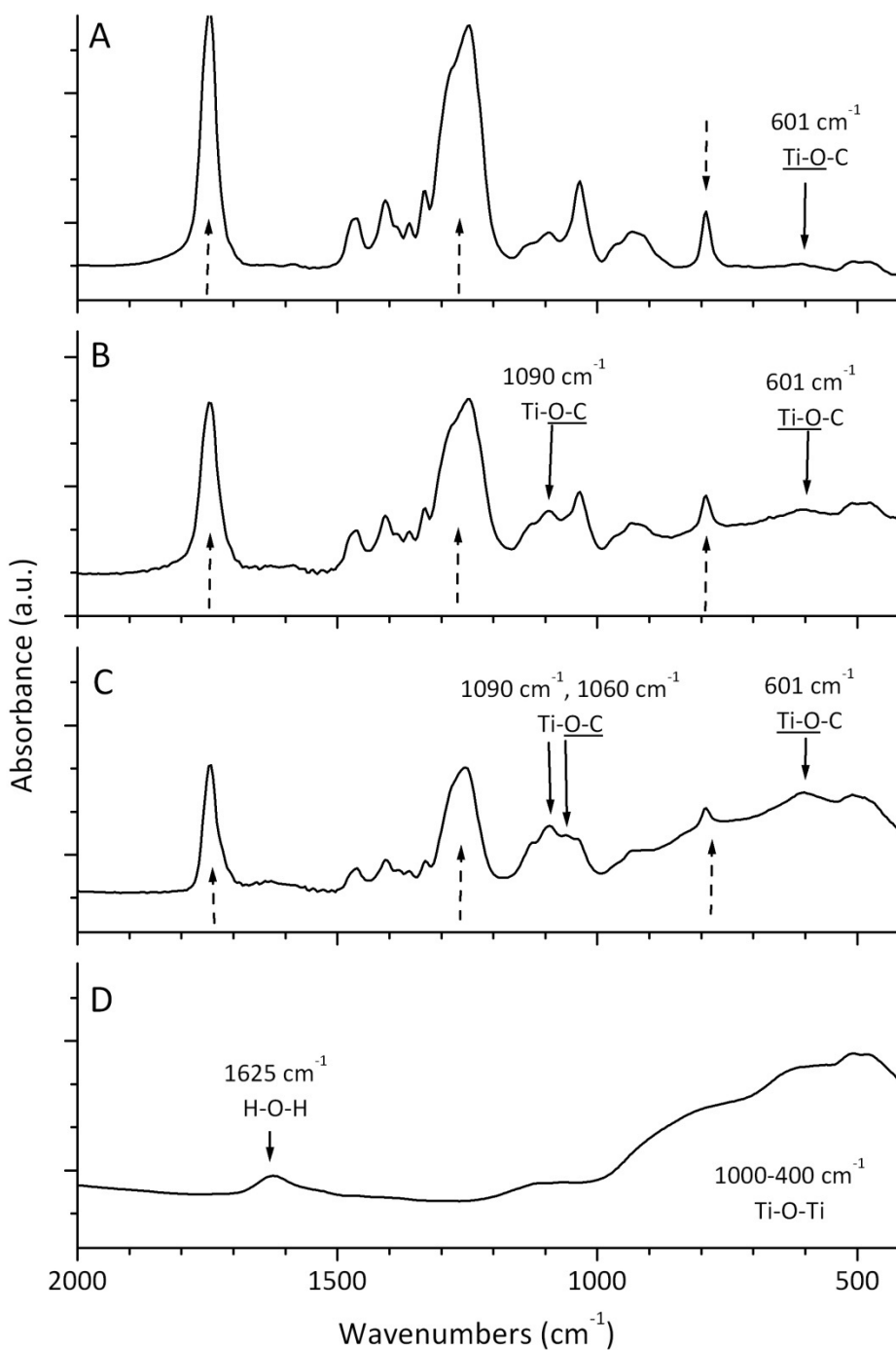


Figure 29. FT-IR spectra in the range 2000 cm^{-1} – 400 cm^{-1} with band attribution. A: H-PTMC75, B: H-PTMC50, C: H-PTMC25, D: plain titania. Broken arrows indicate PTMC characteristic bands

In order to gain information about the nature of such interactions, FT-IR spectra of all samples were recorded. Figure 29 shows the spectra of the hybrids focused in the range $2000 - 400\text{ cm}^{-1}$, together with that of plain Titania synthesized in the same

experimental conditions. The spectrum of titania (Figure 29-D) is in good agreement with that reported in the literature for amorphous titanium oxide [153]. It displays a weak and broad band at 1625 cm^{-1} attributed to bending vibrations of absorbed water [154] and a broad multiple absorption region in the range 1000 cm^{-1} - 400 cm^{-1} , where vibrations of Ti-O-Ti bonds are located [153,155].

XRD measurements (Figure 30), performed both on plain titania and on H-PTMC50, reveal the absence of any peak associated with a crystalline phase, confirming that in analyzed samples TiO_2 is completely amorphous. In the case of H-PTMC50, the broad signal around 15° - 25° is due to the amorphous polymeric phase. This result is reasonable taking into account the mild curing treatment applied during hybrid synthesis ($T = 110\text{ }^\circ\text{C}$), whose temperature is too low to promote crystal phase formation [156].

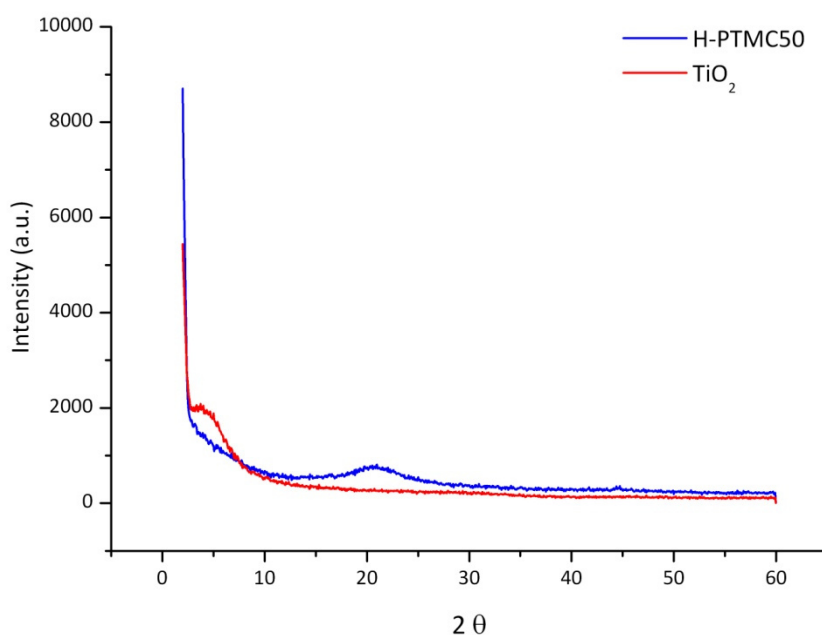


Figure 30. WAXS results for plain titania (red) and H-PTMC50 (blue)

Hybrid spectra in Figure 29 exhibit the characteristic absorption bands of both PTMC and titania. As expected, the intensity of PTMC bands at 1745 cm^{-1} , 1243 cm^{-1} and 792 cm^{-1} decreases with decreasing organic phase content in the hybrid, while in the region between 1000 cm^{-1} and 400 cm^{-1} , where vibrations of titania moieties are located, band intensity shows an opposite trend.

As concerns titania-related vibrations, it can be noted that the band located at 601 cm^{-1} is particularly prominent in the hybrid spectra with respect to its intensity in the spectrum of plain TiO_2 . Furthermore two new bands, particularly evident in H-PTMC50 and H-PTMC25 spectra, appear at 1090 cm^{-1} and 1060 cm^{-1} , the latter being well visible only in H-PTMC25. Kriegsmann et al. [157] investigated FT-IR absorption bands of several titanium alkoxides and reported the presence of a strong band around 600 cm^{-1} , attributed to Ti-O stretching vibration, and of two intense bands in the region 1000 cm^{-1} - 1100 cm^{-1} , assigned to C-O stretching vibrations. According to these results, absorption bands of PTMC-titania hybrids located at 601 cm^{-1} and at 1060 cm^{-1} and 1090 cm^{-1} are assigned to the vibration of Ti-O-C covalent bonds linking PTMC chain terminals to the titania network.

Surprisingly the intensity of the absorption bands attributed to Ti-O-C covalent bonds increases with the increase of inorganic content in hybrids. In other words, it seems that the number of Ti-O-C covalent bonds between organic and inorganic phases is higher when the PTMC content, thus the OH organic chain terminal content, is lower. This is an unexpected trend considering that, in the range of organic-inorganic compositions employed for hybrid synthesis polymeric OH functionalities are in great defect compared with the amount of Ti-OH groups.

Table 7. Results of extraction experiments in dichloromethane of HPTMC-50 and H-PTMC25

Sample	Insoluble residue (wt.-%)	Extract (wt.-%)	PTMC (wt.-%)		
			before extraction ^a	after extraction	
				from residue ^b	from extract ^c
H-PTMC50	53	49	77	30	28
H-PTMC25	79	23	52	27	25

^a PTMC content in hybrid, evaluated as $w_{PTMC} = (1 - w_{TiO_2})$, where w_{TiO_2} is obtained from the TGA solid residue (Table 6. TGA results for hybrids and for PTMC organic-phase precursor Table 6, Titania residue Exp.) as described in the text.

^b Evaluated from Eq.4.

^c Evaluated from Eq.5.

With the aim to find an explanation for the observed FT-IR behavior, H-PTMC50 and H-PTMC25, i.e. the two samples for which the presence of Ti-O-C covalent bonds is

well evident in FT-IR spectra, were selected to perform extraction experiments in dichloromethane, whose results are reported in Table 7.

In order to calculate the weight percentage of PTMC which is bound to titanium oxide in the hybrids, both the insoluble (residue) and the soluble fraction (extract) were accurately dried and weighed. The fraction of bound PTMC was calculated both from the residue (Eq.8) and from the extract (Eq.9) as follows:

$$w_{PTMC-bound} = (w_{res} - w_{TiO_2}) \cdot 100 \quad [Eq.8]$$

$$w_{PTMC-bound} = [(1 - w_{ex}) - w_{TiO_2}] \cdot 100 \quad [Eq.9]$$

where w_{ex} and w_{res} are the weight fractions of dried extract and residue respectively and w_{TiO_2} is the weight fraction of TiO_2 in the hybrid derived from TGA (experimental values in Table 6). The results, listed in Table 7, show that by adding extract and residue percentages a value very close to 100% is obtained. Taking into account the experimental error, this result confirms that no significant material loss has occurred during the extraction procedure. The extraction experiments reveal that only part of PTMC in the hybrid is covalently bound to the titania network and that this bound fraction is higher in H-PTMC25 than in HPTMC-50, in agreement with the FT-IR results described above.

The extracted soluble fractions were also analyzed by 1H -NMR and the spectrum of HPTMC-50 extract is reported in Figure 31. All PTMC signals already discussed (see Figure 26) are present in the spectrum of the extract. However, in Figure 31 the ratio of the area of the (a) signal at $\delta = 3.7$ ppm (corresponding to the protons of the methylene groups adjacent to OH terminal functionalities) to that of the (c+d) signal at $\delta = 4.4$ ppm – 4.0 ppm (assigned to the protons of the methylene groups adjacent to carbonate groups) is significantly higher than the value obtained for plain PTMC (Figure 26). This observation accounts for a molecular weight of PTMC in the hybrid that is lower than that in the pure polymer precursor.

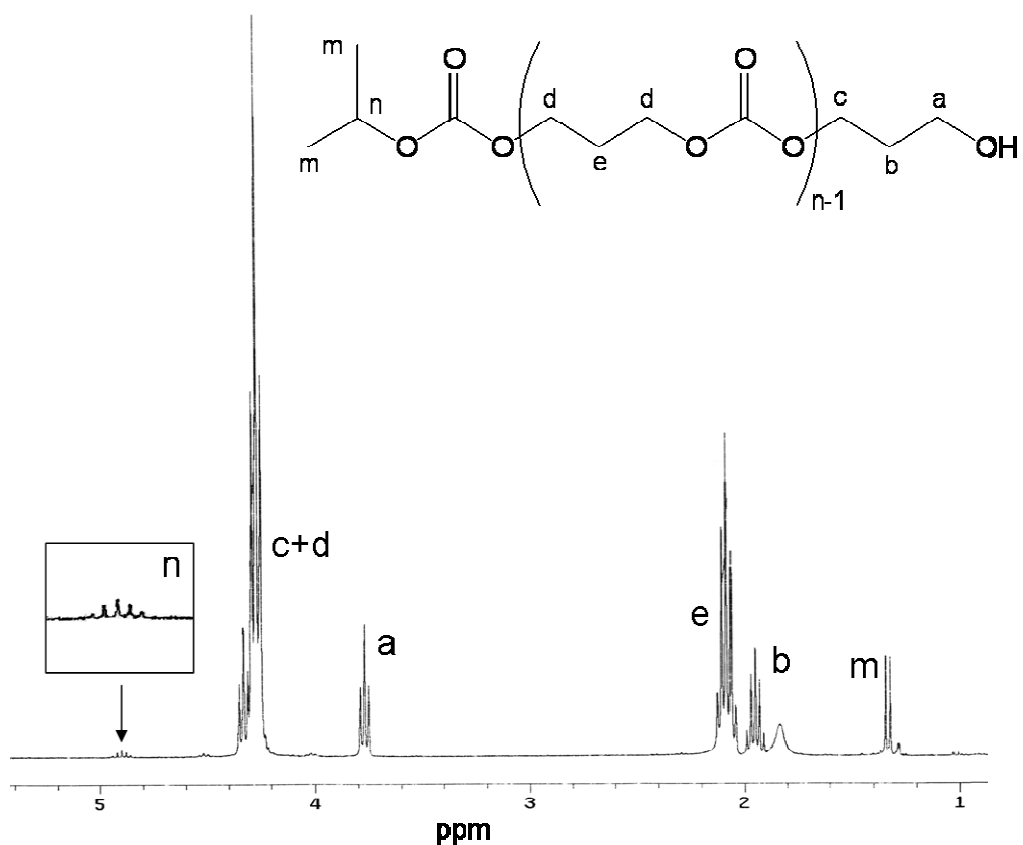


Figure 31. ^1H NMR spectrum in the 1 – 5 ppm spectral window with peak attribution of H-PTMC50 extracted fraction

The occurrence of PTMC degradation after hybrid synthesis is also confirmed by DSC measurement of the same extract, which reveals that the glass transition temperature of PTMC extracted from the hybrid has decreased from $-18\text{ }^\circ\text{C}$ (plain polymer) to $-42\text{ }^\circ\text{C}$. Furthermore, besides the expected chemical shifts, two additional signals are detected in the ^1H -NMR spectrum of H-PTMC50 extract (Figure 31), i.e. a doublet at $\delta = 1.3\text{ ppm}$ (m) and a multiplet at $\delta = 4.9\text{ ppm}$ (n). These two signals are consistent with the presence of isopropyl carbonate moieties located at PTMC chain terminals, according to earlier literature results [158,159].

^1H -NMR analysis of H-PTMC25 extracted fraction, reported in Figure 32, revealed that in this hybrid PTMC is degraded to lower molecular weight than in H-PTMC50 and that the number of isopropyl terminal groups is accordingly larger in H-PTMC25. Also the glass transition temperature of H-PTMC25 extract, determined by DSC, is lower ($T_g = -62\text{ }^\circ\text{C}$) than that of H-PTMC50 insoluble fraction ($T_g = -42\text{ }^\circ\text{C}$).

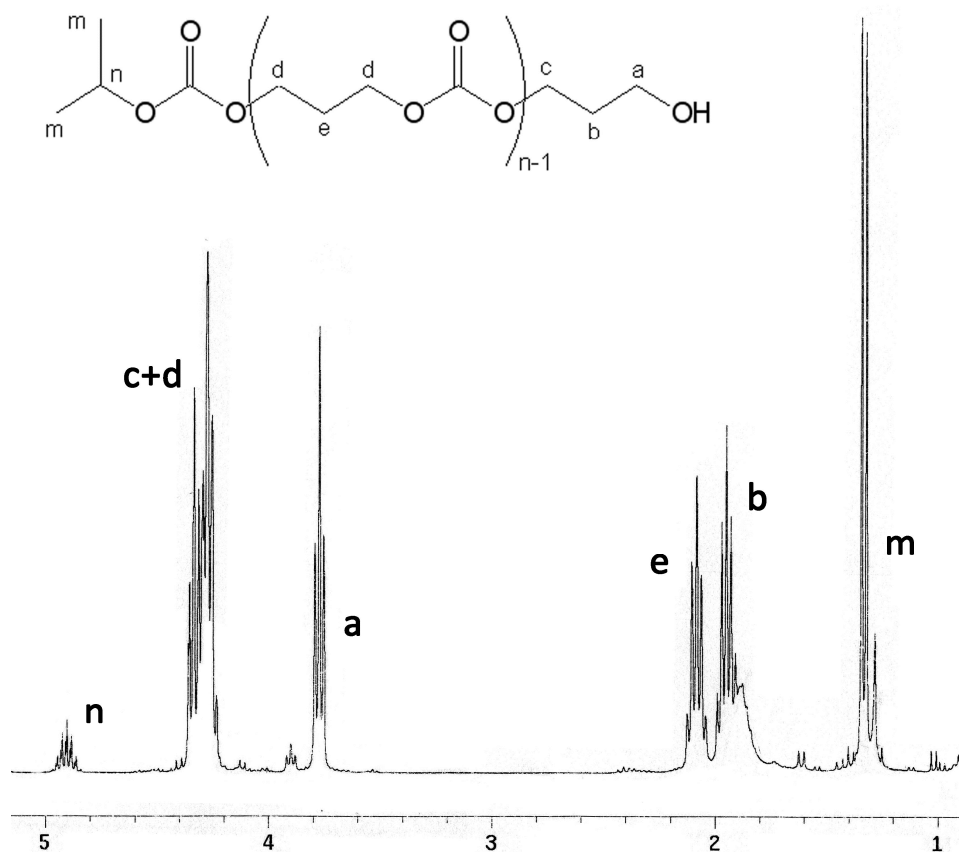


Figure 32. ¹H NMR spectrum in the 1 – 5 ppm spectral window with peak attribution of H-PTMC25 extracted fraction

The presence in the extracted fraction of low molecular weight PTMC chains bearing some isopropyl terminals may find its reason in transesterification of polycarbonate chains operated by isopropanol (by-product of TIPT hydrolysis) during the sol-gel process, as sketched in Figure 33. The proposed reaction is promoted by TIPT, with Ti(IV) atom that acts as a Lewis acid and increases electrophilicity of the carbonate carbon, thus favoring nucleophilic attack of isopropanol. Each transesterification event leads to formation of one isopropyl carbonate terminal group and also of one hydroxyl end functionality (Figure 33) that is able to react with a Ti-OH group forming a Ti-O-C covalent bond between polymer and Titania.

The insoluble residue obtained from extraction procedures was also analyzed by FT-IR spectroscopy. Figure 34 compares the FT-IR of the insoluble fraction with the spectra of the correspondent hybrid before extraction.

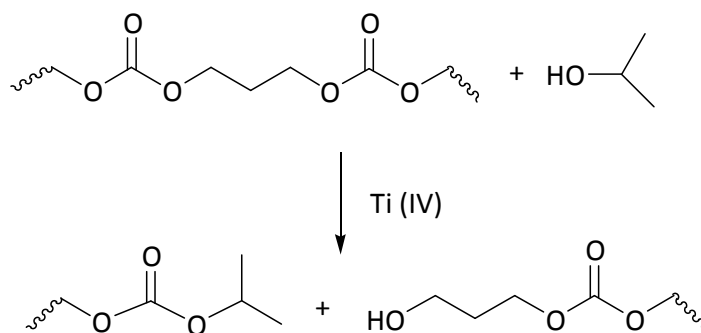


Figure 33. Proposed mechanism of transesterification reaction

The curves of the residues exhibit all signals present in the respective plain hybrid spectra, but they display a different relative intensity of characteristic absorption bands. PTMC specific bands at 1745 cm^{-1} , 1243 cm^{-1} and 792 cm^{-1} are less intense in the residue than in the original hybrid spectra, as expected, because extraction of non-bound polymer chains has changed the organic to inorganic ratio in the materials. Worth noting is the presence in the residue spectra of bands at 1090 cm^{-1} , 1060 cm^{-1} and 601 cm^{-1} , whose intensity is higher than in the corresponding whole hybrid spectra. This result demonstrates correctness of the above attribution of such bands to Ti-O-C covalent bond vibrations.

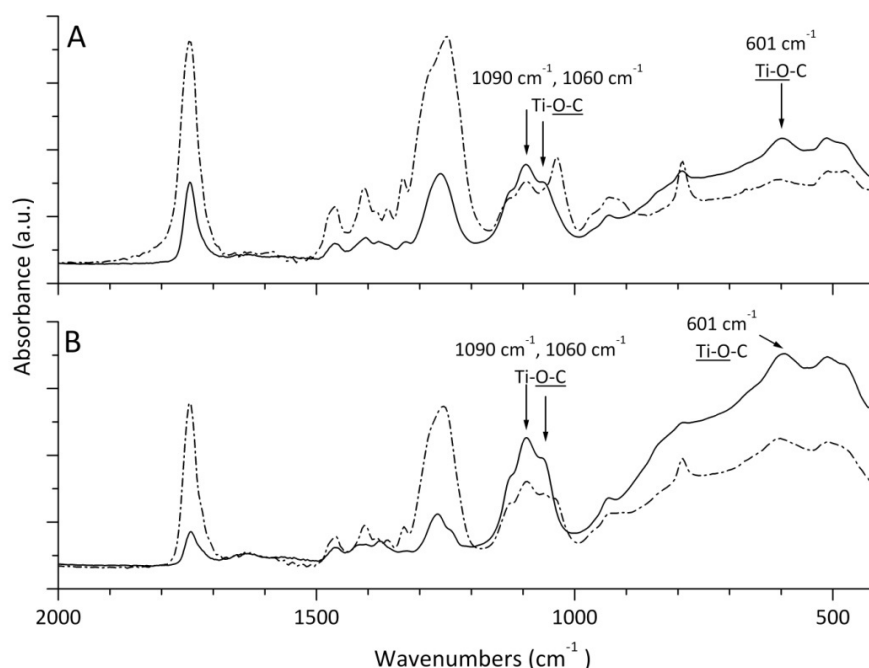


Figure 34. Comparison of FT-IR spectra of hybrids (broken line) with FT-IR spectra of insoluble residue from extraction experiments (solid line) in the range $2000\text{ cm}^{-1} - 400\text{ cm}^{-1}$; A. H-PTMC50, B. H-PTMC25

In summary, investigation of the internal structure of PTMC-titania hybrids with different composition has demonstrated formation of covalent bonds between polymer and inorganic phase, whose amount increases with increasing inorganic phase content. Responsible for this behavior is a transesterification reaction, operated by isopropanol on PTMC chains and catalyzed by the presence of Ti atoms, which occurs during hybrid synthesis. Transesterification, which is favored by the increase of inorganic precursor content in the feed, leads to lowering of PTMC molecular weight and to formation of additional hydroxyl polymer terminals, thus promoting formation of Ti-O-C covalent bonds.

2.3. Solid-State Properties of PTMC-Titania Hybrids

Thermal properties of hybrid samples were investigated by DSC and the results are compared in Figure 35 and Table 8 with those of plain PTMC.

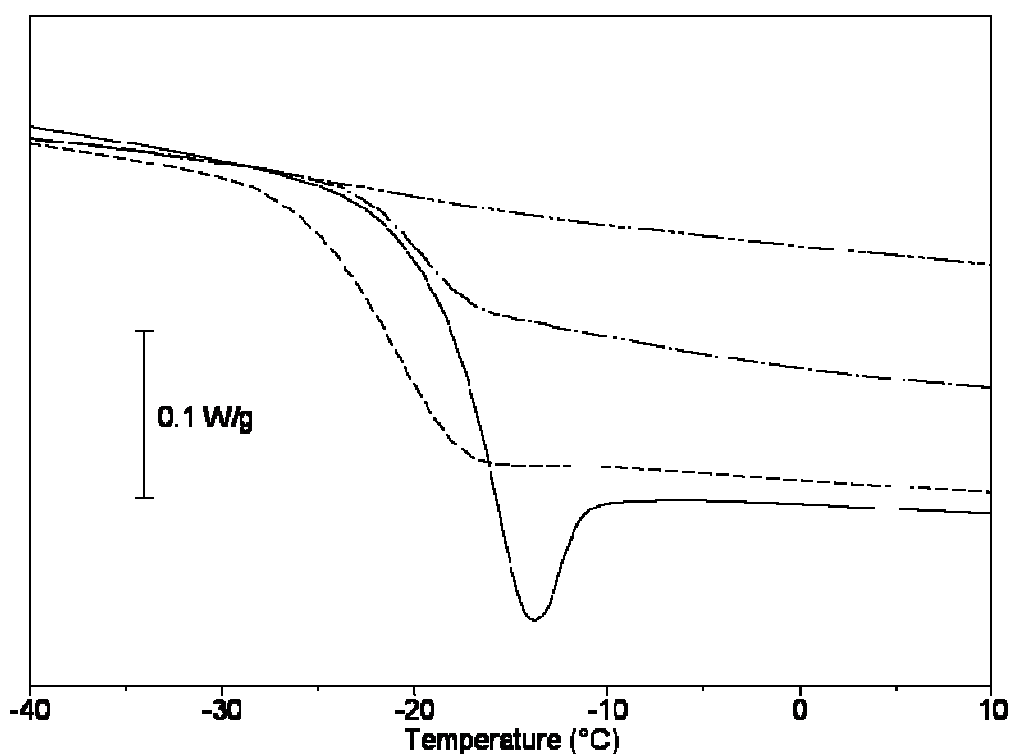


Figure 35. DSC curves focused on the glass transition region of PTMC (—), H-PTMC75 (-----), H-PTMC50 (- · -), H-PTMC25 (- · · -)

The DSC curves in Figure 35 show that the intensity of the polymer glass transition decreases with increasing titania precursor in the hybrid feed. Table 8 compares the

experimental specific heat increment at the glass transition (referred to the whole sample weight) with the expected ΔC_p based on the actual weight of PTMC in each sample.

Table 8. Thermal properties of hybrids and of the organic-phase precursor PTMC, from DSC on quench-cooled samples

Sample	T_g (°C)	ΔT_g (°C)	ΔC_p (J/g°C)	
			Exp.	Calc. ^a
PTMC	-18	4	0.54	-
Hyb-25	-22	7	0.49	0.49
Hyb-50	-20	8	0.26	0.42
Hyb-75	- ^b	- ^b	- ^b	0.28

^a Calculated with respect to the PTMC content in each hybrid, i.e. $w_{PTMC} = (1 - w_{TiO_2})$, where w_{TiO_2} is obtained from the TGA solid residue (Table 6, Titania residue Exp.) as described in the text.

^b Not detectable.

The PTMC content in hybrids is derived by difference from the TiO_2 content obtained from the TGA solid residue. Table 8 clearly illustrates that in H-PTMC75 the experimental and calculated values match, while in H-PTMC50 the experimental ΔC_p is significantly lower than that expected, and in H-PTMC25 (expected $\Delta C_p = 0.28$ J/g°C) no glass transition is appreciable in the DSC curve. This behavior is a direct consequence of the presence of Ti-O-C covalent bonds between polymer and titania network, that inhibit polymer chain mobility [99]. In the case of H-PTMC25, for which the highest number of Ti-O-C covalent bonds was revealed by FT-IR measurements (Figure 29), the interaction between the phases is so strong that almost no glass transition is detected, despite the fact that in this hybrid the amount of polymer is more than 50 wt.-%.

For Class II hybrids it was previously reported that the glass transition temperature of polymers whose chain ends are locked into the inorganic network increases upon hybrid synthesis [130,107,131,132]. However T_g values reported in Table 8 show an opposite trend, with T_g in hybrid samples being lower than in the PTMC polymer precursor. As already explained for polyester-containing hybrids that showed a similar behavior (see Results and Discussion, Paragraph 1.1), it must be noted that in the present case T_g values are influenced by two phenomena that lead to opposite effects.

The presence of covalent bonds that anchor polymer chains to the titania domains should cause an increase of glass transition temperature in hybrids with respect to the plain polymer precursor. Nevertheless, the molecular weight of the polymeric phase decreases as a result of the transesterification reactions occurring during hybrid synthesis, thus leading to an opposite effect on T_g . The interplay of these two events determines the final T_g values. Table 8 also shows that the transition width ΔT_g is wider in the synthesized hybrids than in the pure PTMC, indicating that, as expected, PTMC-titania interactions cause broadening of relaxation time distribution.

As concerns *optical properties*, all hybrid samples prepared were solid transparent films, irrespective of the inorganic content. In Figure 36 a picture of H-PTMC50 sample is reported as an example.



Figure 36. Picture of H-PTMC50

Transparency of organic-inorganic hybrids is generally considered as an indication of the presence of nanometric metal oxide domains [77]. In order to confirm this hypothesis preliminary AFM analyses were performed and Figure 37 shows tapping mode topography and phase-contrast image of sample H-PTMC50, as an example.

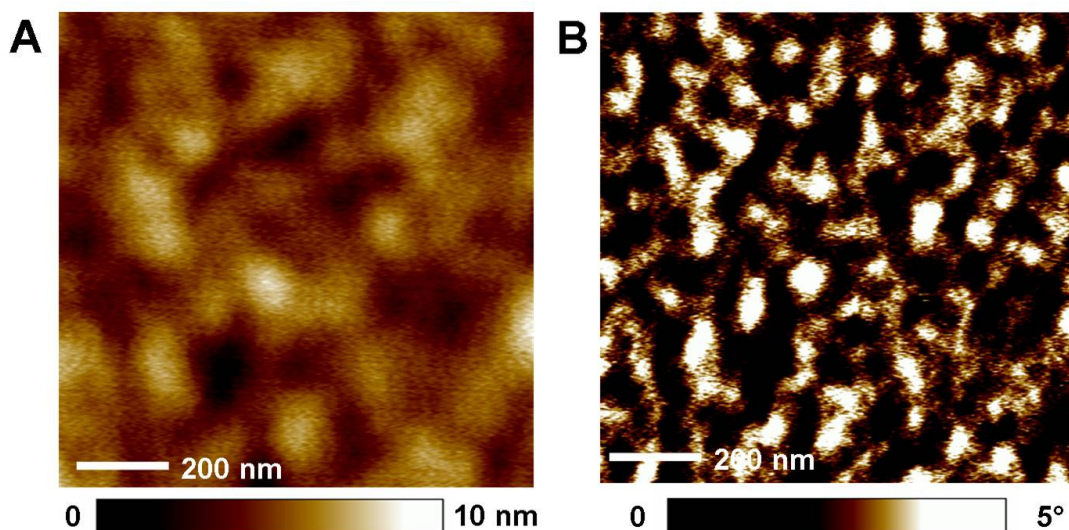


Figure 37. Tapping mode AFM topography (A) and phase-contrast image (B) of H-PTMC50

It can be observed from the topographic image (Figure 37-A) that the film surface is rather flat with a root mean square (rms) roughness of 1.1 nm. Additionally, the phase-contrast image provides information about the nanostructure of the hybrid material (Figure 37-B). It was previously reported that phase-contrast images reflect hardness of the analyzed surfaces [160] and thus, in the case of organic-inorganic hybrids, this methodology allows to discriminate hard inorganic from soft polymeric domains [161]. Figure 37-B reveals the presence of bright hard objects characterized by diameter that ranges from 30 nm to 60 nm, recognized as titania domains, that are homogeneously dispersed within the dark soft PTMC matrix. These preliminary results confirm that optical transparency of PTMC-titania hybrids arises from their nanostructure.

2.4. Hybrid Coating on Flat Surfaces

Analogously to what described for polyester-containing hybrids, in this work hybrids made employing PTMC as the organic phase were applied as coating layers on different flat substrates. As observed for polyester-containing hybrids, PTMC-based materials showed very good adhesion towards all surfaces on which they have been coated in this study (plastics, metals, glass). In addition, when the hybrids are cast on a transparent substrate, such as PP, the resulting coated material maintained transparency to visible light (Figure 38).

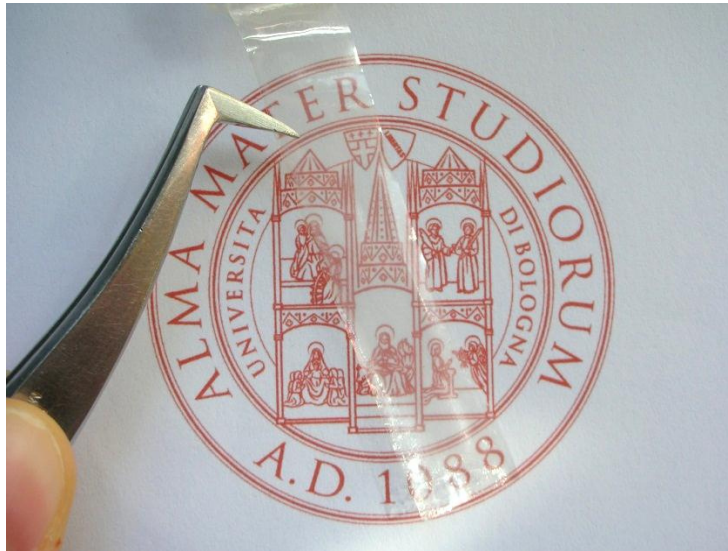


Figure 38. Hybrid H-PTMC50 cast on different PP. Application on the transparent substrate outlines coating transparency to visible light

UV-Vis absorption properties of hybrids in the form of thin layers coated on transparent PP sheets were tested. Figure 39 shows UV-Vis transmittance spectra of three PTMC hybrids with different titania content coated on PP.

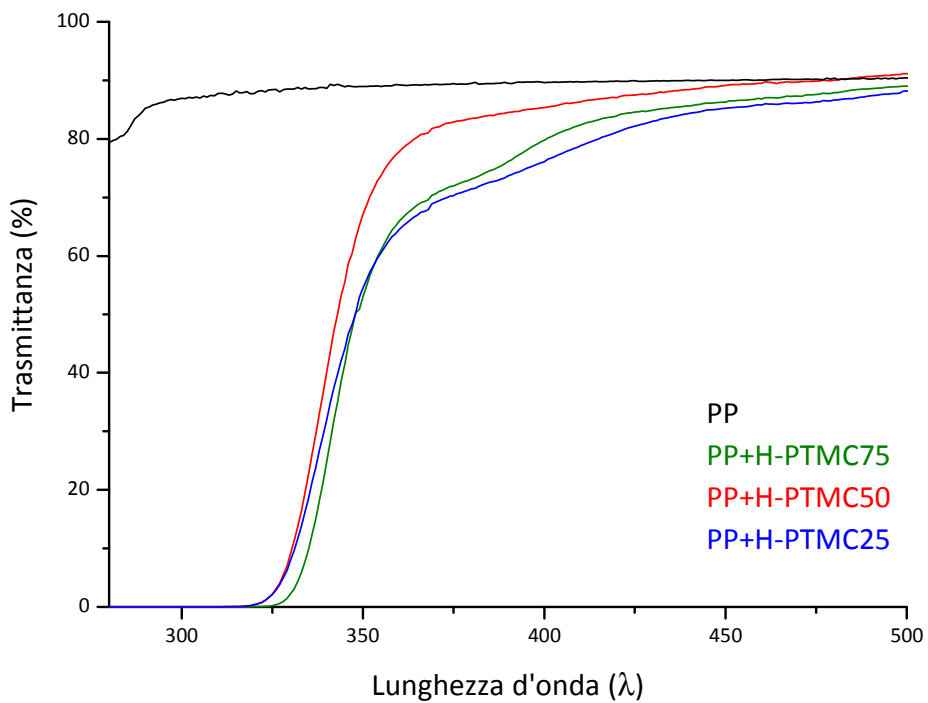


Figure 39. Comparison of UV-Vis spectra of PP sheet (black) with those of PP sheet coated with: H-PTMC75 (green, 8 μ m), H-PTMC50 (red, 9 μ m) and H-PTMC25 (blue, 8 μ m)

For the sake of comparison, the spectrum of plain PP is also reported, showing transmittance higher than 90% along all the UVB/UVA range. In the same frequency range, hybrids H-PTMC75, H-PTMC50 and H-PTMC25 are able to cut off a large fraction of the UV radiation, being completely opaque to UV radiation up to $\lambda = 325$ nm, i.e. over the whole dangerous UVB range (280 - 315 nm) [134]. The synthesized hybrids are also able to cut off a large part of the UVA spectrum, i.e. the UV-A2 range [134]. In particular, for wavelengths lower than 350 nm the transmitted radiation intensity is reduced down to 50%.

In conclusion, in this thesis new hybrids containing poly(trimethylene carbonate) and titania were synthesized starting from different feed compositions. The simple synthetic procedure applied for hybrid production allowed to obtain solid transparent materials, whose nanometric structure was confirmed by AFM. In the hybrids, phase separation at nanoscale level is achieved by establishing covalent bonds between organic and inorganic phases. They result from transesterification reactions that occur during hybrid synthesis and are catalyzed by the presence of titanium compounds. In these hybrids transesterification reactions do not lead to formation of organo-titanium esters, as found in polyester-based hybrid materials. They rather promote formation of Ti-O-C covalent bonds through the production of polymer OH chain terminals, that are able to react with the titania precursor. Hybrids coated on transparent substrates show their intrinsic optical transparency and their ability to completely block UV radiation in the range UVB and UV-A2.

3. Polyester-Titania Hybrid Coatings for X-ray Shielding

Since organic-inorganic hybrids are produced by the sol-gel process, the entire spectrum of wet coating techniques (spin coating, dip coating, spray coating, doctor blade, etc.) is available for the deposition of these materials as coating layers. It is thus possible to foresee a wide range of applications for such hybrids on a number of substrates, no matter their actual shape. In the work by Mazzocchetti et al. regarding PBG-containing hybrids, it was shown that bulk H-PBG hybrids were opaque to X-ray radiation [99] (see Introduction, Paragraph 3.4). This property, like the already discussed UV-blocking activity (see Results and Discussion, Paragraph 1.2), is peculiar

to the inorganic phase. Thus, it can be speculated that radiopacity will characterize any titania-containing hybrid, to an extent that depends on the actual amount of titania per hybrid unit volume. On the assumption that radiopacity can be transferred to fabrics by the simple described hybrid coating procedure, hybrid materials might be employed for the production of light-weight garments for X-ray protection. As already described in the Introduction, the production of such X-ray shielding clothes for the protection of medical staff during interventional fluoroscopy, could be a powerful tool for the prevention of pathologies that stem from chronic X-ray exposure, such as skin damages, injuries to the eye lenses and also some kind of cancer (see Introduction, Paragraph 2.4).

In this Chapter, hybrid deposition via dip coating on complex substrates such as textiles made of different fibers, namely cotton, silk, wool and polyester, is described. PBG was chosen as the organic phase of the hybrid, owing to its low T_g and low-melting crystal phase ($T_m < RT$). Owing to PBG thermal properties, PBG-based hybrids are expected to be able to comply with yarn flexibility leading to coated garments that result soft to the touch.

In order to achieve the application of the hybrid coating on textiles, a synthetic procedure analogous to that described for polyester-containing bulk hybrid (see Results and Discussion, Chapter 1) is followed, the only difference being a greater amount of solvent used to dissolve the hybrid precursors (polymer + TITP).

All fabrics that were coated with such hybrids showed a quite pleasant hand. SEM micrographs of cotton coated with H-PBG50 are shown in Figure 40, where they are compared with pictures of the untreated fabric at the same magnification. Remarkably, no appreciable differences between coated and uncoated fabric are observed. Observing Figure 40-B and Figure 40-D, it is interesting to note that the hybrid is able to coat single fibers of the yarn rather than coating the yarn as a whole. Openings between yarns are maintained and therefore fabric breathability is preserved.

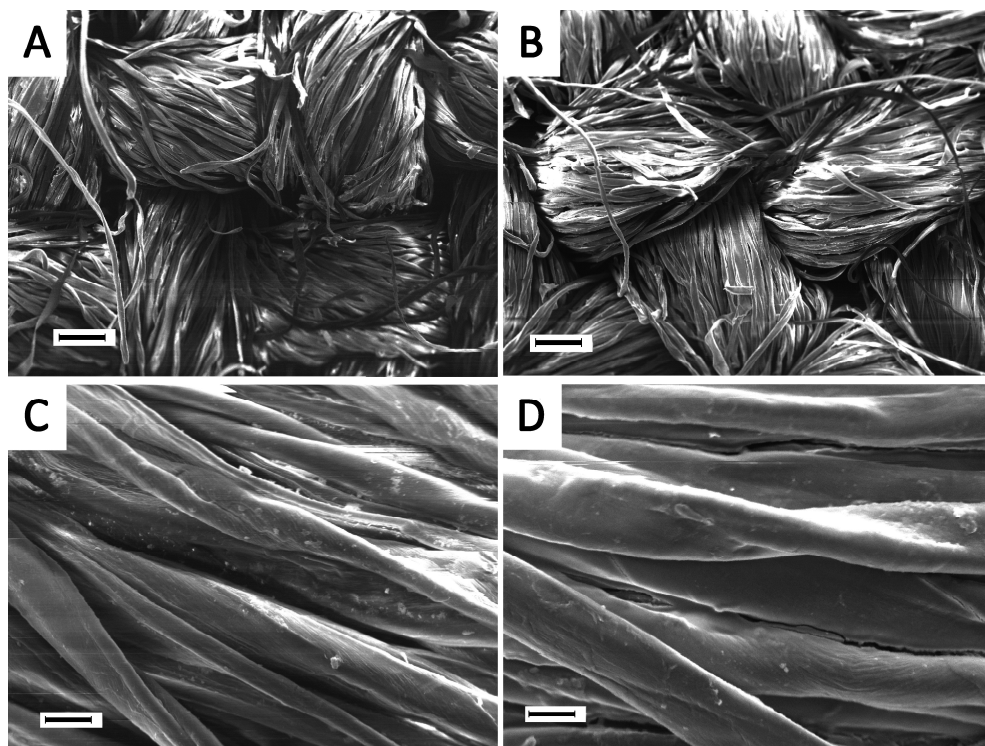


Figure 40. SEM micrographs at different magnification of cotton fabric (A and C) and of cotton fabric coated with H-PBG50 (B and D). Bar: 100µm in A and B, 10µm in C and D

TGA measurements on hybrid-coated fabrics (cotton, wool, silk, polyester) were performed and revealed interesting results. Analysis of plain uncoated fabrics, shows in all cases very small (if any) solid residue at the end of the TGA measurement (T = 600 °C) under air purge.

Table 9. Solid residue (from TGA) of bulk H-PBG hybrids and of hybrid-coated cotton.

Sample	PBG in feed (wt.-%)	Sample type	HL ^a (%)	TGA	
				Exp. ^b (%)	Calc. (%)
H-PBG25	25	Bulk	-	44.5	45.8 ^c
	25	Coated fabric	13.3	9.9	7.5 ^d
H-PBG50	50	Bulk	-	22.5	21.9 ^c
	50	Coated fabric	22.7	6.9	6.4 ^d
H-PBG75	75	Bulk	-	11.2	8.6 ^c
	75	Coated fabric	17.5	3.2	3.4 ^d

^a Percent hybrid load, defined as the hybrid weight fraction in the final sample, gravimetrically determined by weighting the dried fabric sample before and after hybrid coating.

^b Experimental solid residue at 600°C evaluated from TGA experiments run in air.

^c SR_{bulk}^{Cal} calculated according to Eq. 4.

^d SR_{hybCot}^{Cal} Calculated according to Eq. 10.

On the contrary, upon heating up to 600°C in air, all coated fabrics yield a solid residue, whose value reflects the composition and amount of hybrid coated on the fabric. Hereafter, as an example, the behavior of coated cotton fabrics, whose TGA results are listed in Table 9, is discussed deeply. The weight of the coated fabric can be considered as arising from two independent components, namely the cotton yarn and the hybrid loaded onto the tissue.

Upon heating the plain cotton yarn up to 600°C in air purge, a constant solid residue $SR_{cot} = 1.7\%$ by weight is obtained. The plain hybrids in bulk form were also analyzed in the same conditions and the solid residue found at 600 °C (SR_{bulk}^{Exp}), is reported in Table 9. Table 9 also lists the solid residue (SR_{bulk}^{Cal}) expected on the assumption that during the sol-gel process complete hydrolysis of the inorganic phase precursor has occurred and, upon oxidation and volatilization of all the organic material, only TiO_2 is left over at 600 °C. As already discussed for polyester-containing hybrids, SR_{bulk}^{Cal} can be calculated following Eq.4.

The amount of hybrid coated on the cotton fabrics, gravimetrically estimated, is reported as percentage hybrid load (HL) in Table 9. The values of HL vary between ca. 13% to about 23% and it is interesting to note that, notwithstanding such differences, the solid residue at 600 °C of the coated fabrics measured by TGA (Table 9) increases with increasing TIPT content, i.e. in the order H-PBG75 < H-PBG50 < H-PBG25. Such experimentally determined residues may be compared with the value expected for hybrid-coated cotton ($SR_{hyb-cot}^{Cal}$), calculated according to the following equation:

$$SR_{hyb-cot}^{Cal} = SR_{bulk}^{Exp} \frac{HL}{100} + SR_{cot} \frac{(100 - HL)}{100} \quad [Eq. 10]$$

where SR_{bulk}^{Exp} refers to a bulk hybrid obtained from the same sol-gel feed as the one applied on cotton fabrics. Eq. 10 takes into account the contribution to the solid residue from thermal degradation of both hybrid and cotton fibers, assuming that hybrid formation on textile substrates proceeds in the same manner as in the bulk. The results reported in Table 9 show substantial agreement between calculated residue ($SR_{hyb-cot}^{Cal}$) and experimental results, demonstrating that the composition of the hybrid, *in situ* synthesized from precursors adsorbed onto the fabric, is that expected

based on their mutual weight ratio. No significant composition change due to precursor preferential loading by capillary sorption is observed, thus showing that the final coating composition can be easily defined by playing on the sol-gel feed composition.

It has been demonstrated in previous Chapters and in the literature [99,107] that in both titania and silica-based hybrids the solid residue obtained after TGA experiments in air up to 600 °C is the plain metal oxide.

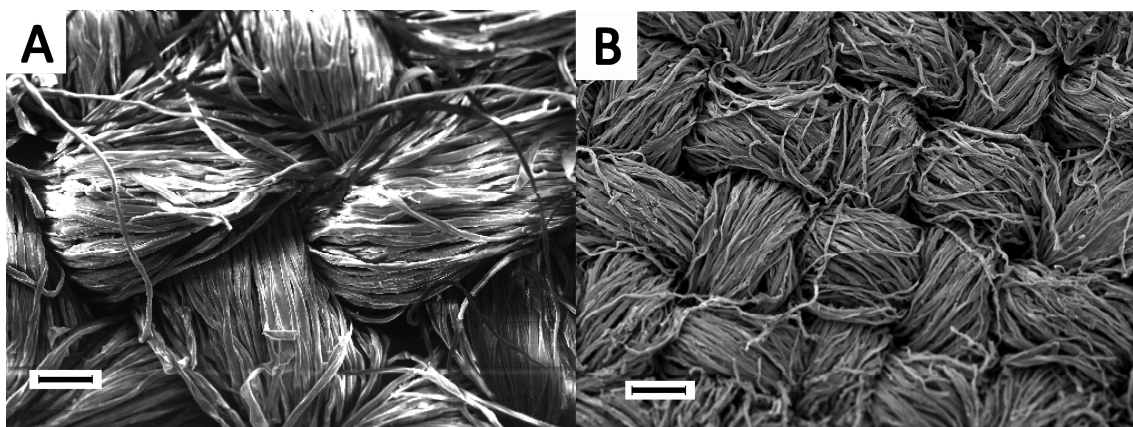


Figure 41. SEM micrographs at the same magnification of cotton fabric coated with H-PBG50 before (A) and after TGA measurement up to 600 °C in air (B). Bar: 100 μ m

In this work, as mentioned above, almost no significant solid residue ($SR_{cot} = 1.7$ %wt) was found in plain cotton, hence it can be safely assumed that also the TGA residue of coated fabrics at 600 °C (Table 9) is mainly composed of titania. Figure 41 shows SEM micrographs of cotton coated with H-PBG50, taken before and after a TGA run up to 600 °C in air. It is evident that the solid residue after TGA experiment keeps the exact texture as the starting sample, although notably reduced in size. A SEM micrograph at higher magnification of the TGA solid residue (Figure 42) showing the yarn cross-section clearly illustrates that the fibrous-looking residue in the front view of Figure 41-B is indeed an empty titania envelope that maintains the fiber shape after thermal decomposition and volatilization of both the polymeric component of the hybrid coating and the inner cellulosic fibers.

Radiographic images of coated fabrics were taken with mammographic equipment. Figure 43 shows radiographs of H-PBGX bulk hybrids and of hybrid-coated cotton.

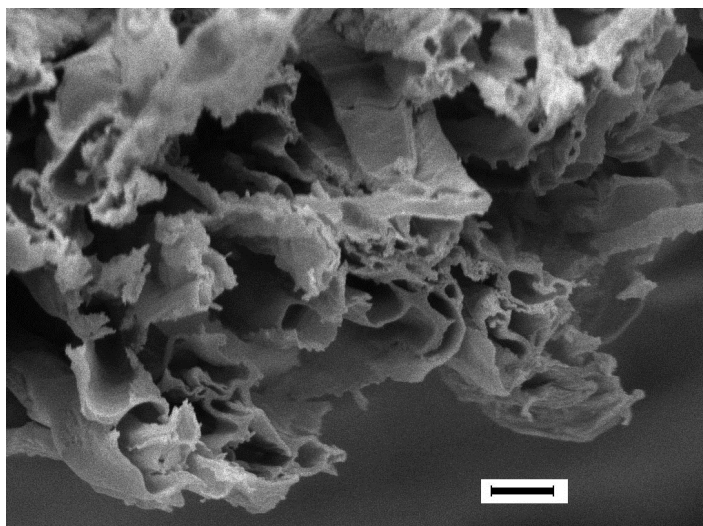


Figure 42. SEM micrograph of cotton fabric coated with H-PBG50 after TGA experiment up to 600°C in air (side view). Bar: 5 μ m

For the sake of comparison, the radiograph of plain cotton is also reported. It is interesting to note that good contrast against the background can be obtained with a thick (640 μ m) H-PBG50 bulk sample (Figure 43-a); an acceptable contrast can be also obtained with a thinner (70 μ m) sample of H-PBG25 hybrid (Figure 43-c) because, as expected, the material enrichment in inorganic component allows thinning of the hybrid layer while keeping radiopacity.

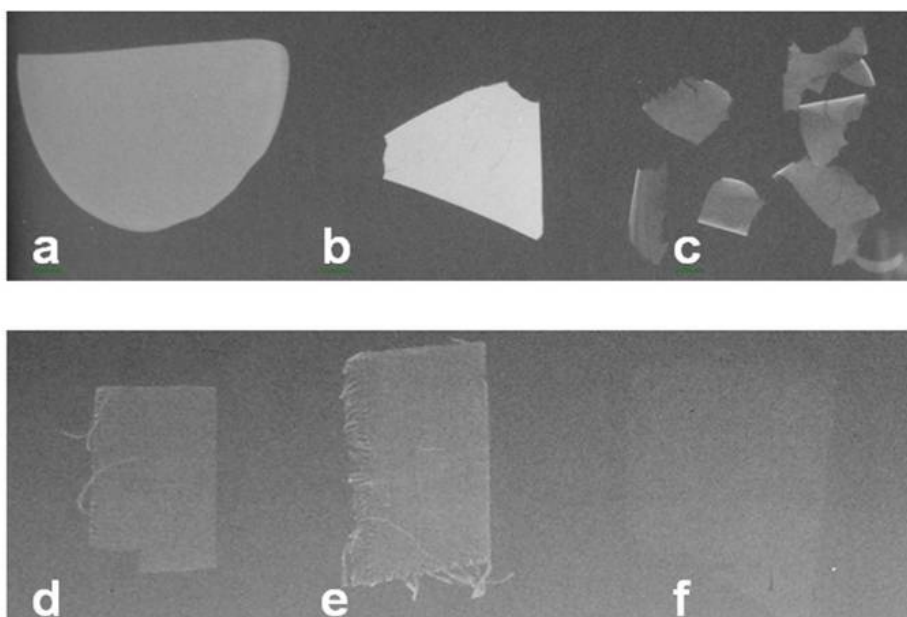


Figure 43. Radiographic images of a. bulk H-PBG50 (640 μ m thick), b. bulk H-PBG25 (490 μ m thick), c. bulk H-PBG25 (70 μ m thick), d. cotton fabric coated with H-PBG50, e. cotton fabric coated with H-PBG25 and f. uncoated cotton fabric

Obviously, a much thicker H-PBG25 sample (490 μm) provides a much stronger contrast (Figure 43-b). Contrarily to the plain uncoated cotton, that is practically undetectable under radiographic conditions (Figure 43-f), application of hybrid coating on cotton fabric gives, as expected, X-ray visibility to the textile. In Figure 43-d and Figure 43-e cotton coated with hybrids characterized by a different composition, namely H-PBG50 and H-PBG25 respectively, are reported. Worth noting that the similar radiographic contrast of the two samples may be ascribed (see Table 9) to an almost double load onto the fabric of the hybrid with lower titania content (H-PBG50).

In addition to cotton, other fabrics can become radiopaque upon coating with the hybrids, as shown in Figure 44 in the case of polyester and silk coated with H-PBG25 and of wool coated with H-PBG50. In order to compare radiopacity of different hybrid-coated textile substrates, besides hybrid composition also the specific loading capacity of each substrate must be taken into account. Hence the hybrid load per fabric unit area (L_A , mg/cm^2) is defined as follows:

$$L_A = \frac{\Delta m}{a} \quad [\text{Eq. 11}]$$

where Δm is the hybrid load on fabric, gravimetrically determined as the fabric weight increment upon hybrid coating (weights before and after coating being taken after careful drying), and a is the area of the fabric sample measured from a digital picture via software (see Experimental Part).

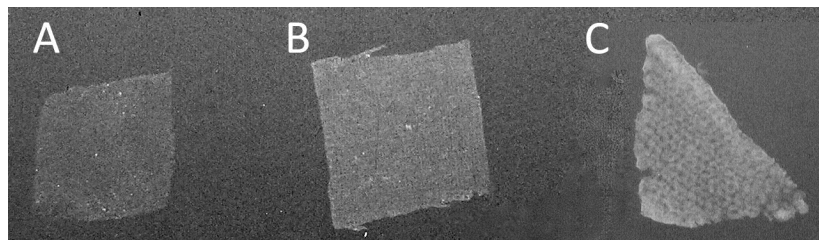


Figure 44. Radiographic images of A. polyester coated with H-PBG25, B. silk coated with H-PBG25 and C. wool coated with H-PBG50

The effect of the L_A parameter is evident when comparing in Figure 44 the pictures of polyester and silk fabrics coated with the same hybrid (H-PBG25). Lower contrast of

the coated polyester sample originates from its lower normalized hybrid loading ($L_A = 3.44 \text{ mg/cm}^2$) compared with that of the brighter coated silk textile ($L_A = 6.17 \text{ mg/cm}^2$). Worth mentioning is that the normalized loading of cotton fabric coated with the same H-PBG25 hybrid, whose radiograph is displayed in Figure 43-e, is $L_A = 3.76 \text{ mg/cm}^2$. Picture comparison shows that cotton (Figure 43-e) and polyester (Figure 44-A), i.e. two fabrics with similar load per unit area, display similar radiopacity. On the other hand, the reason for the strong radiographic contrast of the wool fabric in Figure 44, despite the fact that it is coated with H-PBG50 (a hybrid with smaller titania content than H-PBG25), lays on the great loading capacity of wool ($L_A = 28.84 \text{ mg/cm}^2$). The above examples show the concomitant effect on final fabric radiopacity both of fiber ability to upload the hybrid precursors during the synthetic procedure and of the fraction of titania in hybrid formulation.

The results discussed above demonstrate an easy route to provide radiopacity to textiles with many possible applications, for example, in the field of personal X-ray protective equipment. It is likely that workers involved in everyday radiation exposition, like medical staff occupied in vascular fluoroscopic interventions, may take great advantage of light and comfortable garments able to protect from dangerous X-rays.

4. Organic-Inorganic Hybrids for Enhancement of Device X-ray Visibility

X-ray identification and traceability is an essential requirement for medical devices in many surgical and medical applications. The use of traceable devices has significantly improved patient treatment quality and has generated growing interest towards the development of new radiopaque biomaterials. One strategy for the obtainment of medical devices with improved radiopacity consists in the application at the device surface of a radiopaque coating (see Introduction, Paragraph 2.3). It is known that a strong improvement of device X-ray visibility can be obtained by the application on the device of a surface thin layer (few μm) of a radiopaque metal, such as gold [58] or tantalum [56]. However such metal coatings have some critical drawbacks, such as low adhesion to the substrate and fragility [57].

An alternative to metal coatings can be represented by radiopaque hybrid organic-inorganic coatings. As already pointed out in this thesis, hybrid materials can be easily applied as thin coatings on both flat and irregularly-shaped substrates, by either *doctor blade* or dip coating procedures, and if the polymer phase is properly chosen, hybrid coatings can be significantly more flexible than metal coatings. Moreover, unlike the latter, hybrids have exhibited very good adhesion to different types of substrates, including metal and plastics (see Results and Discussion, Paragraph 1.2). Good radiopacity of organic-inorganic hybrids has been recently reported by Mazzocchetti et al. [99,107] (see Introduction, Paragraph 3.4) and has been also demonstrated in the previous Chapter for polyester-containing hybrid materials, suggesting that these materials might find applications in medical fields where X-ray visibility is required, such as interventional fluoroscopy. Since radiopacity is associated with the presence of the inorganic component, the latter content must be quite high in thin hybrid coatings in order to reach a good level of radiopacity. As a consequence, the coating layer tends to be rigid and to form cracks upon deformation, thus resulting not suitable for biomedical applications.

In this Chapter an alternative solution for enhancing medical device radiopacity that combines advantages of both metallic and hybrid coatings is presented. High metal radiopacity is associated with good mechanical and protective properties of organic-inorganic hybrids in the form of a double-layer coating. Tantalum, a highly radiopaque metal already employed in the medical field [162,163,164], is chosen as the constituent of the first layer deposited on sample substrates by means of a sputtering technique. The second layer is composed of a hybrid whose constituents are well-known biocompatible organic and inorganic components, such as the two polymers PCL and PDMS, and titanium oxide, respectively.

4.1. Synthesis and Characterization of Tantalum Layer

Sputtering is a physical vapor deposition technique that allows to deposit a thin coating of a chosen material on a substrate [165] yielding high purity layers whose thickness can be controlled by varying deposition time. Sputtering has been previously used for the production of radiopaque metal coatings on biomedical devices [57]. In

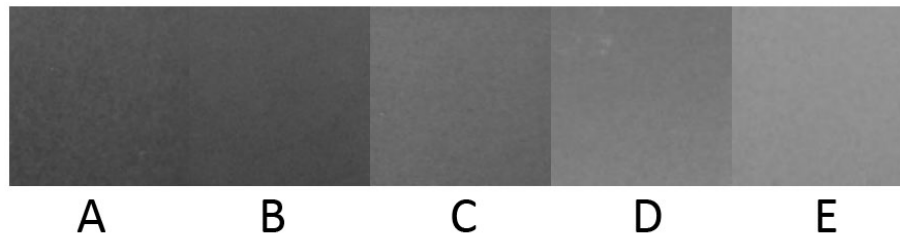
this work tantalum coatings with different thickness were deposited on plastic flexible substrates made of PP. Deposition times of 30 min, 60 min and 90 min were applied and the obtained samples were labeled respectively Ta1, Ta2 and Ta3. In order to evaluate thickness of the deposited layer, Ta was contemporarily sputtered on aluminum stubs half-covered with adhesive tape. Removal of tape yielded a neat step whose height corresponds to the thickness of the deposited Ta layer. Metal layer thickness, evaluated by SEM, gradually increases from 1 μm to 5 μm with changing sputtering time from 30 min to 90 min (Table 10). The sample sputtered for 30 min was also analyzed by AFM, obtaining a value of 0.91 μm for the metal layer thickness, in good agreement with the value obtained by SEM.

Table 10. Tantalum coatings characterization

Sample	Sputtering time (min)	Ta layer thickness (μm)	Radiopacity ^a
PP	-	-	2
Ta1	30	1.0	19
Ta2	60	2.5	40
Ta3	90	5.0	53

^a Calculated as the difference between the pixel intensity of the sample in the radiographic image and the pixel intensity of the background (see background in Figure 45).

All PP coated samples were then analyzed using X-ray radiographic equipment (mammograph) in order to verify their radiopacity and the obtained X-ray images are reported in Figure 45. It is clearly seen that the uncoated PP is almost undistinguishable from the background, whereas application of the tantalum coating provides good X-ray visibility to the plastic substrates. In addition, contrast of the X-ray images, i.e. radiopacity, clearly increases with tantalum coating thickness.



*Figure 45. X-ray images of A: background, B: PP film substrate, C: Ta1, D: Ta2 and E: Ta3.
Brighter pictures correspond to higher radiopacity*

The intensity of the transmitted X-ray radiation (I) through a sample, which decreases as the radiopacity of the analyzed material increases, is correlated with the radiopaque layer thickness by Eq.1. Application of this equation for quantification of sample radiopacity requires knowledge of radiation intensity, an absolute value not provided by X-ray radiographs that show differences of radiopacity as changes of image contrast.

However, an ASTM standard method [166] is available for the quantitative determination of radiopacity of materials for medical use through radiographic image analysis. In the test method, radiopacity is quantitatively evaluated from the radiographic image as the difference between sample tested and background in terms of either optical density (logarithmic ratio of transmitted to incident light through the radiographic image) or pixel intensity (gray scale value ranging from 0 to 255). Radiopacity values for the three tantalum coated PP samples and for plain PP were calculated according to the ASTM standard from digitalized radiographic images as the difference in pixel intensity and results are shown in Table 10. As already suggested by simple observation of the radiographs in Figure 45, the value of relative pixel intensity for the Ta-coated substrates increases with thickness of the tantalum layer.

X-ray images of aluminum sheets with different thickness were also collected and their radiopacity values were calculated following the same procedure.

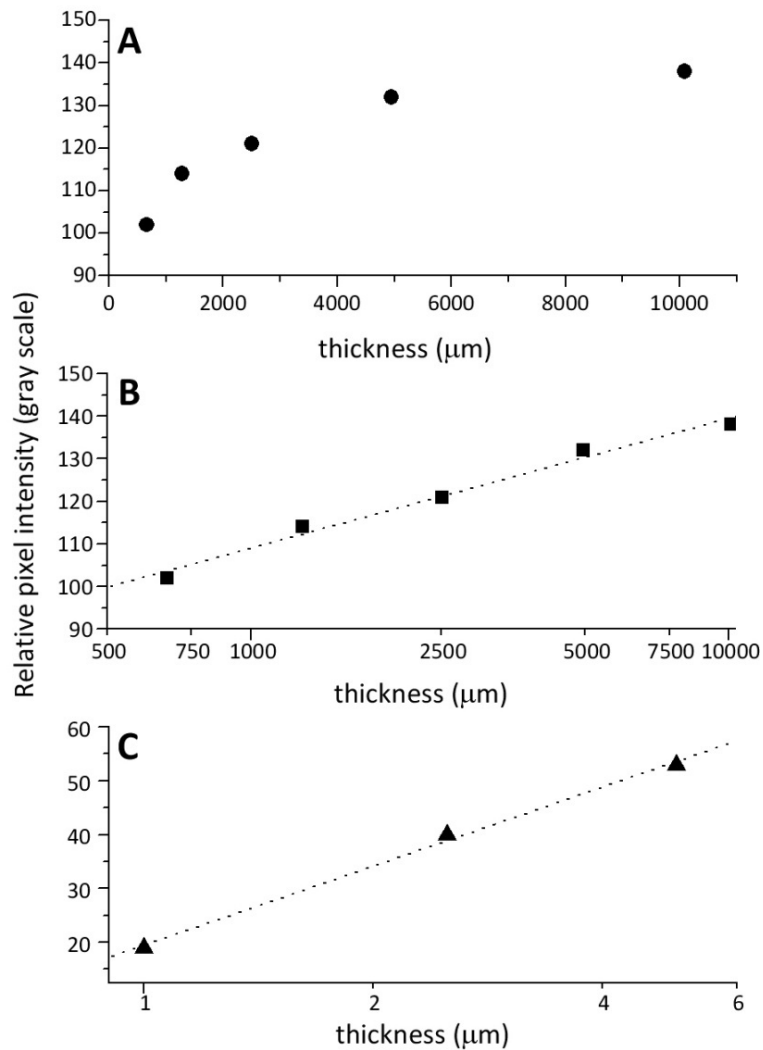


Figure 46. Radiopacity values, reported as relative pixel intensity calculated from a digitalized radiographic image, as a function of sample thickness: for aluminum sheets (A: linear scale, B: semi-logarithmic scale) and for tantalum coated PP sheets (C: semi-logarithmic scale). Linear regression lines are reported in B and C

The relative pixel intensity versus Al thickness is shown in Figure 46-A and, upon replotting the data in a logarithmic thickness scale (Figure 46-B), a linear correlation is obtained (Eq.12, correlation coefficient $R^2 = 0.993$):

$$Rad_{Al} = 17.5603 + 30.4901 \log t \quad [\text{Eq.12}]$$

where Rad_{Al} is the radiopacity of the aluminum sample expressed in relative pixel intensity and t is the thickness of the sample. An analogous linear dependence of optical density on thickness was earlier observed by Watts et al. [167] in a radiographic

evaluation of aluminum standards for dentistry. In Figure 46-C the relative pixel intensity of the Ta-coated PP films (from Figure 45) is plotted as a function of coating thickness in a logarithmic scale, showing a good linear correlation between radiopacity and Ta layer thickness (Eq.13, $R^2 = 0.999$):

$$Rad_{Ta} = 19.4687 + 48.8589 \log t \quad [\text{Eq.13}]$$

where Rad_{Ta} is the radiopacity of the tantalum sample expressed in relative pixel intensity and t is again sample thickness. This result demonstrates that it is possible to obtain Ta layers with controlled radiopacity on medical devices by simply adjusting sputtering deposition time.

Radiopacity data have been obtained in the present work using a mammographic apparatus characterized by an energy radiation of 22 kV. However, for some surgical procedures such as vascular interventions, radiographic equipment that uses higher energy radiation is employed. Since higher energy radiation implies lower visibility of materials, thickness of the radiopaque metallic coating should be adjusted considering the specific application of the medical device to be coated, and the correlation between thickness and radiopacity obtained in this work can be applied to perform this calculation. As an example, X-ray images of an aluminum sheet with a thickness of 650 μm were collected both with the mentioned mammographic apparatus and with angiographic equipment using much higher energy radiation (55 kV, Figure 47).

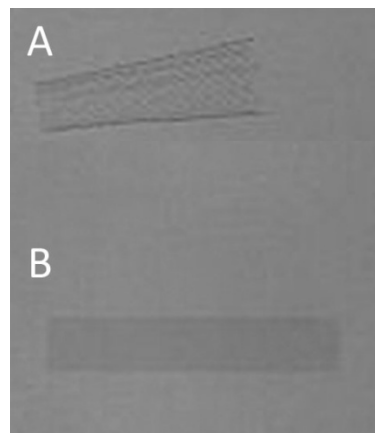


Figure 47. X-ray image of an Al sheet 650 μm thick (B), and of a Ti-Ni stent (A) for comparison, using an angiographic apparatus (energy radiation: 55 kV)

The obtained sample radiopacity (pixel intensity values) decreases from 102 to 16 when analyzed with the above instruments respectively. By application of the correlation reported above for Ta coatings (Eq.13) it is found that, in order to obtain the same visibility under the angiographic equipment as that of the mentioned Al sheet, the thickness of the Ta coating should be 49 μm .

4.2. Synthesis and Characterization of PCL-containing Bulk Hybrid and Double-layer Coating (Metal/PCL-Hybrid)

As already mentioned, metal coatings have some significant drawbacks (mainly fragility and poor resistance to corrosion) that strongly suggest application of a protective layer. In this work protection of the metal layer is achieved by coating it with an organic-inorganic hybrid. Hybrid components were selected considering that biocompatibility is the first requirement that a coating for biomedical devices needs to fulfill. Titania is an inorganic oxide that has already found commercial application in different fields such as food, cosmetics and medicine [168,169,170]. In particular, titania coatings are currently investigated as biocompatibility enhancer in medical devices [171,172,173]. On the other hand, polymer PCL has found a number of biomedical applications due to its biocompatibility and slow degradation rate, including application as component for drug delivery devices and degradable staples (for wound closure) [5]. Titania and PCL are therefore good candidates for the development of a hybrid protective coating for biomedical devices.

The PCL-titania hybrid (H-PCLb50) was synthesized as described in the Experimental Part starting from a TIPT (titania precursor) to polymer ratio equal to 50/50. The hybrid was then investigated by TGA and FT-IR analyses, in the form of a self-standing film, obtained by casting the sol-gel colloidal solution on Teflon sheet by the *doctor blade* method. As already discussed in previous Chapters for polyester-titania and polycarbonate-titania hybrids, evaluation of the high temperature solid residue ($T = 600\text{ }^{\circ}\text{C}$) in TGA experiments, run in the presence of air, allows to ascertain whether the synthetic procedure applied for hybrid production leads to complete hydrolysis of the titania precursor (TIPT). The experimental TGA solid residue at $600\text{ }^{\circ}\text{C}$ for H-PCLb50 is 22.5%, a value that very well compares with that theoretically expected (21.9%), thus

confirming reliability of the synthetic procedure applied that allows to finely tune hybrid composition through the precursors ratio.

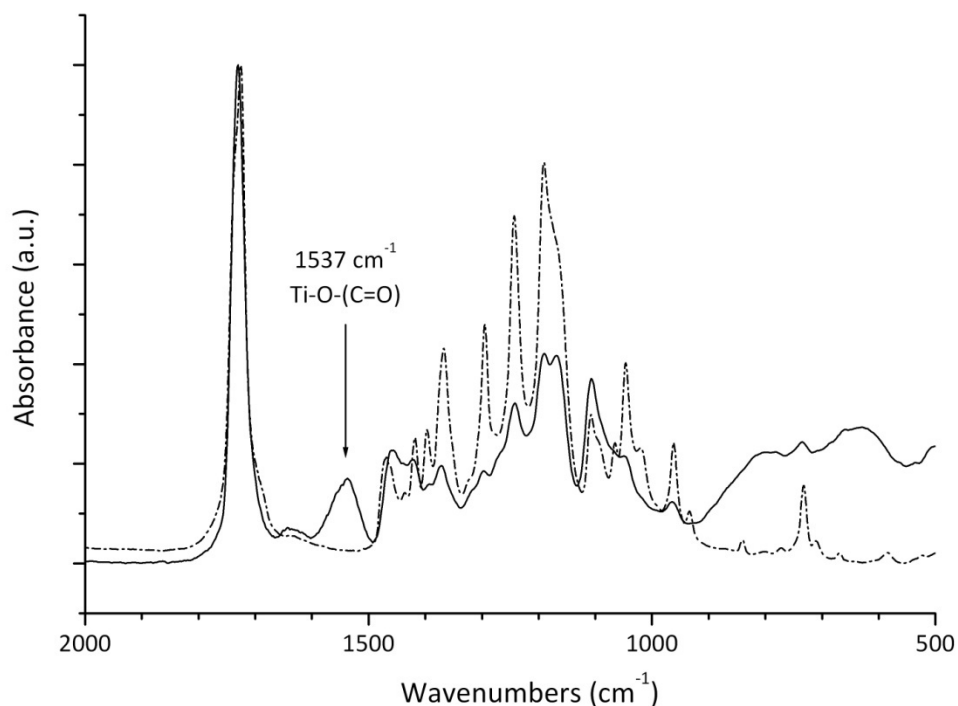


Figure 48. FT-IR spectrum in the range $2000\text{cm}^{-1} - 500\text{cm}^{-1}$ of plain PCLb (broken line) and H-PCLb50 hybrid (solid line)

FT-IR spectrum of the self-standing H-PCLb50 film was recorded and it is compared in Figure 48 with the spectrum of plain PCLb in the range $2000 - 500 \text{ cm}^{-1}$. Both samples show the characteristic carbonyl vibration band at 1733 cm^{-1} , while the hybrid also shows in addition a new band at 1535 cm^{-1} and a broad multiple absorption region in the range $1000 - 500 \text{ cm}^{-1}$, where vibrations of Ti-O-Ti bonds are located [155]. As already thoroughly explained above (see Results and Discussion, Paragraph 1.1) the band at 1535 cm^{-1} is attributed to the presence of organotitanium ester carboxylates, which interact with titanium atoms through the carbonyl oxygen, giving rise to a bidentate bridging structure. Ester moieties connect organic and inorganic phases in this hybrid.

The H-PCLb50 hybrid was then synthesized on top of Ta-sputtered PP substrates (Ta1, Ta2 and Ta3) after layering the precursors by the *doctor blade* procedure. The obtained samples were respectively labeled H-PCLb50-Ta1, H-PCLb50-Ta2 and H-

PCLb50-Ta3. Figure 49 shows a picture and the corresponding radiographic image of a H-PCLb50-Ta1 sample in which the Ta layer underlying the hybrid is star-shaped. Since the hybrid is coated over the whole rectangular sample shown in Figure 49, the picture (A) clearly shows that the hybrid coating is transparent, implying the presence of nano-sized inorganic domains. Comparison of the radiographic image of H-PCLb50-Ta1 in Figure 49-B with that of the plain PP substrate in Figure 45-B shows that, in the area outside the Ta star, the hybrid contributes some additional radiopacity to H-PCLb50-Ta1. Indeed a difference in relative pixel intensity corresponding to 5 units in the grey scale is observed, the increase in radiopacity being attributed to the presence of titanium atoms in the inorganic phase of the hybrid material.

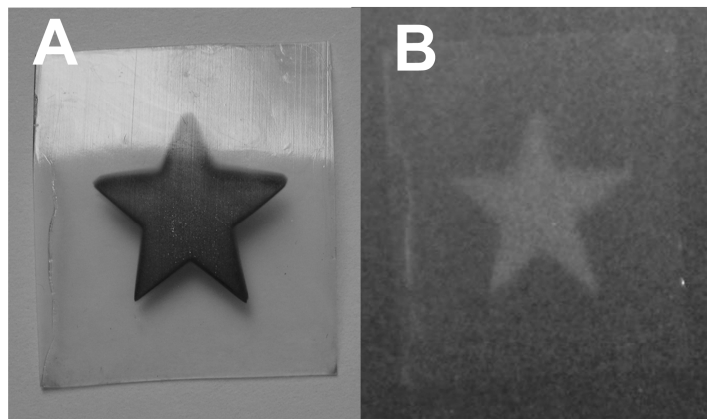


Figure 49. Picture of H-PCLb5-Ta1 sample (A) and corresponding radiographic image (B)

As highlighted in Figure 49, employment of the sputtering technique for radiopaque metallic layer deposition offers the additional interesting feature of easily obtaining specific shapes, by simply applying a suitable hollow-mask over the substrate on which the metal must be deposited. The ability of easy-shaping radiopaque coatings for medical devices is extremely important since it is the presence of one or more radiopaque markers with given shape that permits surgeons to unambiguously localize position and orientation of implanted devices under X-ray radiation, without confusing them with internal body parts. Hence implantable devices, catheters, etc... carrying markers that associate a desired-shape radiopaque Ta layer with an upper protective

hybrid layer, as proposed in this work, represent a new option with interesting potential applications.

The double layered H-PCLb50-Ta sample discussed above (H-PCLb50-Ta1) was subjected to cytotoxicity tests. VW-MSCs were chosen as cellular biocompatibility model, considering that medical devices for vascular surgery could be a potential field of application for the double layered X-ray traceable coating developed in this work.

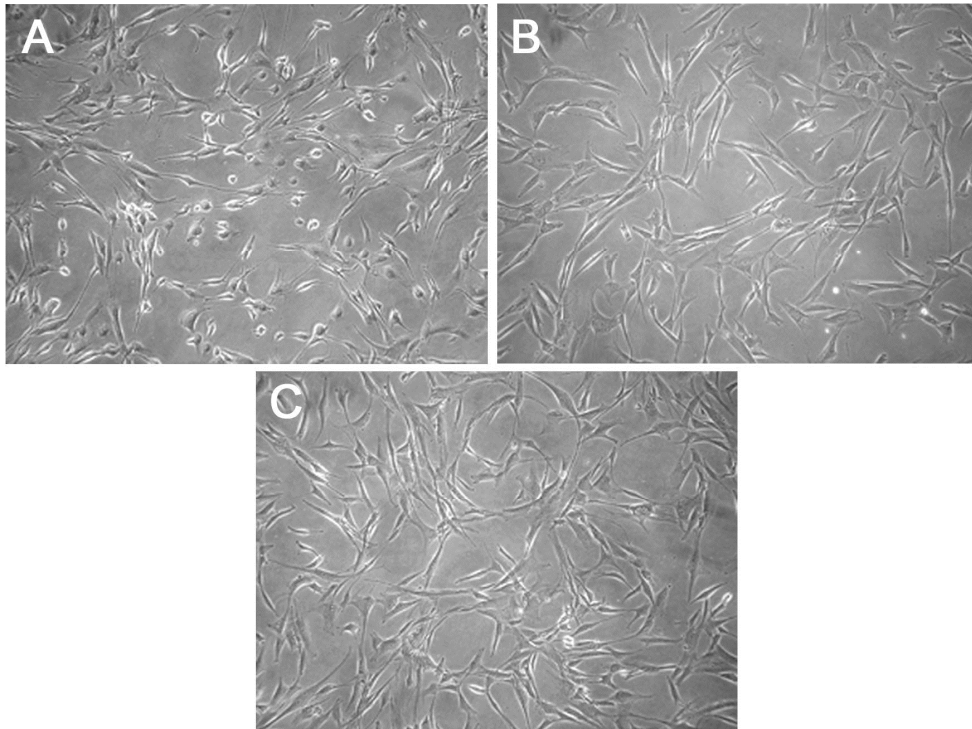


Figure 50. Optical microscope images of VW-MS cells grown in vitro with A. 1mM H₂O₂ for two hours (positive control), B. fresh medium (negative control) and C. H-PCLb50-Ta1 conditioned medium for 24 hours.

The double coating procedure described above consists of various steps and cytotoxicity tests were run on the sample after each single step, starting from the plain substrate (PP film) and going through the two coating steps, i.e. after Ta sputtering (Ta1) and after subsequent hybrid-coating (H-PCLb50-Ta1). Figure 50 compares microscope images of cells exposed to positive control (A), to negative control (B) and to medium conditioned with H-PCLb50-Ta1 (C). It can be noted that exposure to medium conditioned with H-PCLb50-Ta1 doesn't alter the spindle-shaped morphology typical of VW-MSCs and that no significant differences are observed with respect to cells exposed to plain fresh medium (negative control). On the other hand, challenging

the cells with 1mM H₂O₂ as positive control, rapidly determines changes of morphology such as membrane wrinkling and alters adhesion properties of VW-MSCs which shift from spindle to rounded shape morphology; during the two hours of exposure to hydrogen peroxide solution a typical suffering response of cells to adverse growing conditions leading to diffuse cell death is observed. The percentage of cell mortality upon exposure to differently conditioned mediums, including the double layered H-PCLb50-Ta1 sample (Table 11), is comparable with that obtained from negative control.

Table 11. Cytotoxicity test results

Sample	Cell mortality (%) ^a	N° living cells ^b
PP	4.4 (±2.1)	65600
Ta1	4.1 (±3.3)	56600
H-PCLb50-Ta1	4.1 (±2.4)	75800
Positive control ^c	100.0 (±0.0)	0
Negative control ^d	4.9 (±2.4)	77500

^a Values are given as means out of 5 replicates. For each value correspondent standard deviation is reported within brackets.

^b Number of living cells present in each well after 24 hours incubation in medium starting from 50000 seeded cells.

^c Cells exposed to 1 mM H₂O₂ solution for 2 h.

^d Cells exposed to fresh culture medium for 24 h.

Statistical analysis ANOVA ($p \gg 0.05$) confirms that no significant difference between negative controls and tested samples is present. In addition cell counts reveal not only the absence of sample-induced mortality, but also the absence of any obstacle to cell proliferation, suggesting that no toxic elements are released by the samples in culture medium after 24 h of incubation. These preliminary results show that H-PCLb50-Ta1 is biocompatible and that it can be proposed as a suitable material for applications in the medical field.

In addition to the primary biocompatibility demand, specific biomedical devices may require that the radiopaque coating exhibits a degree of deformability that allows it to properly follow device deformation without cracking or detaching. Flexibility of the PCL-titania hybrid coating was evaluated under bending deformation. As shown in Figure 51-A for sample H-PCLb50-Ta1, the double coating stands deformation of the PP

film substrate towards which it shows very good adhesion (no evidence of partial detachment).

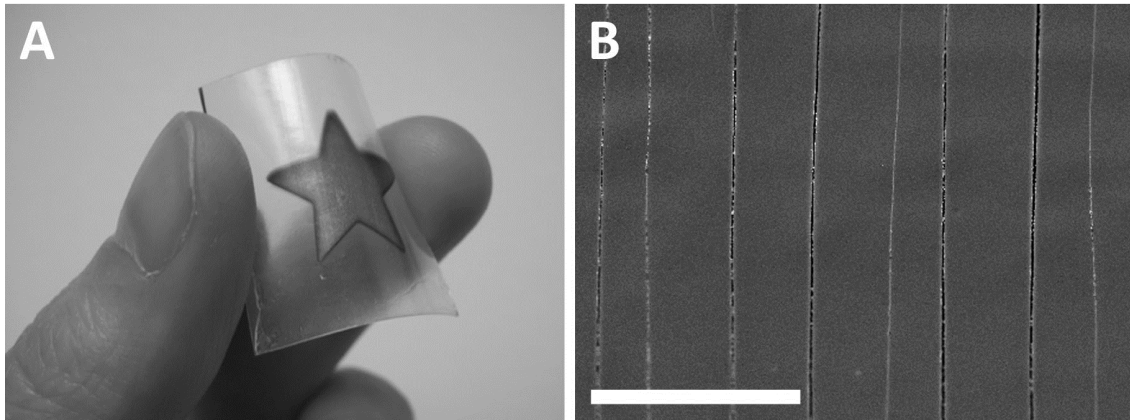


Figure 51. Picture of H-PCLb50-Ta1 sample deformed by hand (A) and SEM image of H-PCLb50-Ta1 surface after bending deformation according to Figure 52 (B). White scale bar = 100 μ m

Simple visual inspection of the coating surface after substrate deformation does not reveal the presence of cracks, whose existence was however evidenced by SEM. Before SEM observation, the sample (a stripe with given dimensions, see Figure 52), is manually bent until its ends come into contact; then some of the deformation is released and sample ends are fixed onto the SEM stub as shown in the picture. The SEM picture of H-PCLb50-Ta1 in Figure 51-B shows that the hybrid coating is not able to fully comply with substrate deformation and it breaks forming parallel cracks perpendicular to the bending direction.

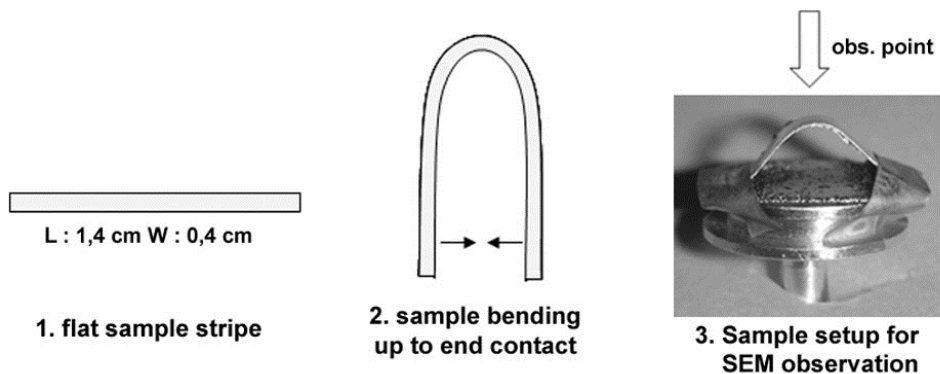


Figure 52. Bending of coated samples and fixing on SEM stub

Fragility and low extensibility exhibited by the H-PCLb50 hybrid might originate, in principle, from crystallinity of the organic polymeric phase (PCLb is a partially crystalline polyester that melts around 60°C) and/or by the stiffening effect of the titania particles. DSC results reported in Figure 53 demonstrate that, though plain PCL easily crystallizes, crystallization of the polymer in the hybrid is almost totally inhibited.

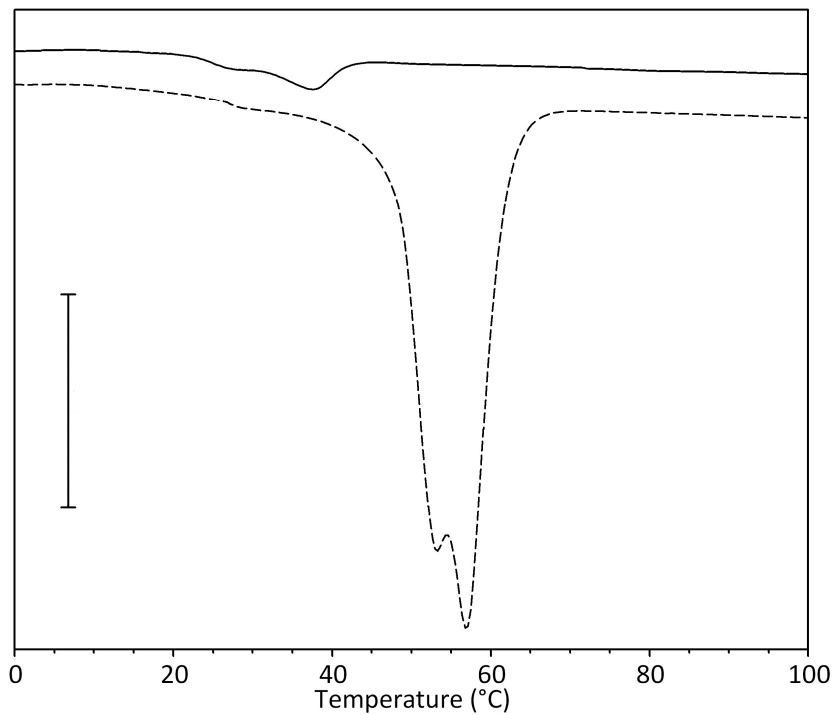


Figure 53. DSC curves focused on the melting region of PCLb (broken line) and H-PCLb50 (solid line); scale bar = 1 W/g.

This result agrees with findings concerning polyester-containing hybrids (see Results and Discussion, Paragraph 1.1), where hindrance to polymer component crystallization was attributed to the occurrence of transesterification reactions which lead to polymer chain shortening and organotitanium ester bond formation. Furthermore it should be noted that the present H-PCLb50 hybrid contains a considerable amount of nano-sized titania particles (22%-wt) that bridge rather short PCL chains in a highly crosslinked network and this might explain low deformability of this coating. Therefore it can be concluded that H-PCLb50 is a material that, according to its biocompatibility and above mentioned properties, may be suitable for production of protective coatings for a range of biomedical devices, but it doesn't seem the best choice for coatings that need to stand considerable bending deformation.

4.3. Synthesis and Characterization of PDMS-Containing Bulk Hybrid and Double-layer Coating

PDMS is well-known in the medical field as a material with good biocompatibility and biodurability [5]. PDMS has found widespread applications in health care, in the fluid form (for medical device lubrication, siliconization of needles and syringes, excipient for topical formulation, etc.), in the cross-linked gel form (as soft skin adhesive) and in the cross-linked solid elastomeric form (for the production of catheters, heart valves, mammary prosthesis, etc.) [5,174]. Moreover, being a totally amorphous polymer with a very low glass transition temperature, PDMS is suitable for the production of highly flexible hybrid materials [90,175]. With the aim of obtaining a coating that is able to stand high deformations, PDMS was investigated in this work as organic component for hybrid protective coating production. In particular, a dicarboxypropyl-terminated PDMS was employed, on the assumption that carboxyl terminals can react with the inorganic phase precursor (TIPT) during sol-gel process, forming organotitanium ester bonds. Since such bonds can form only at chain terminals, a low degree of cross-linking is expected and, as a consequence, PDMS high chain flexibility should be preserved.

In order to additionally decrease rigidity of the final material, the hybrid containing PDMS has a higher organic to inorganic precursor ratio (70/30 w/w) than the PCL-titania hybrid discussed above (50/50 w/w). TGA analysis of the self-standing PDMS-titania hybrid (H-PDMS70), obtained by casting the sol-gel colloidal solution on Teflon sheet by the *doctor blade* method, showed a 45% residue at 600 °C, a value well above that (10.7%) corresponding to the expected titania content, owing to the additional presence of silicon oxide deriving from thermal degradation of PDMS. No precise calculation of SiO₂ produced upon thermal degradation of PDMS in air can be carried out because, as reported in the literature [176], part of the SiO₂ is produced in the gas phase from oxidation of pre-volatilized oligomers and thus can be washed out by the TGA carrier gas.

FT-IR analysis of H-PDMS70 was carried out and Figure 54 compares the spectrum of the hybrid with that of plain PDMS in the range 2000 - 500 cm⁻¹. The plain polymer spectrum shows characteristic bands of PDMS (2964 cm⁻¹ CH₃ stretching; 1260 cm⁻¹

CH₃ bending; 1094 cm⁻¹ and 1021 cm⁻¹ Si-O-Si stretching; 800 cm⁻¹ Si-C stretching) [177] and, in addition, a band (see magnification in insert) at 1711 cm⁻¹ associated with the stretching of carbonyl groups of carboxyl chain terminals. In the H-PDMS70 spectrum, the signal related to carboxyl moieties disappears while a new band located at 1537 cm⁻¹ is observed.

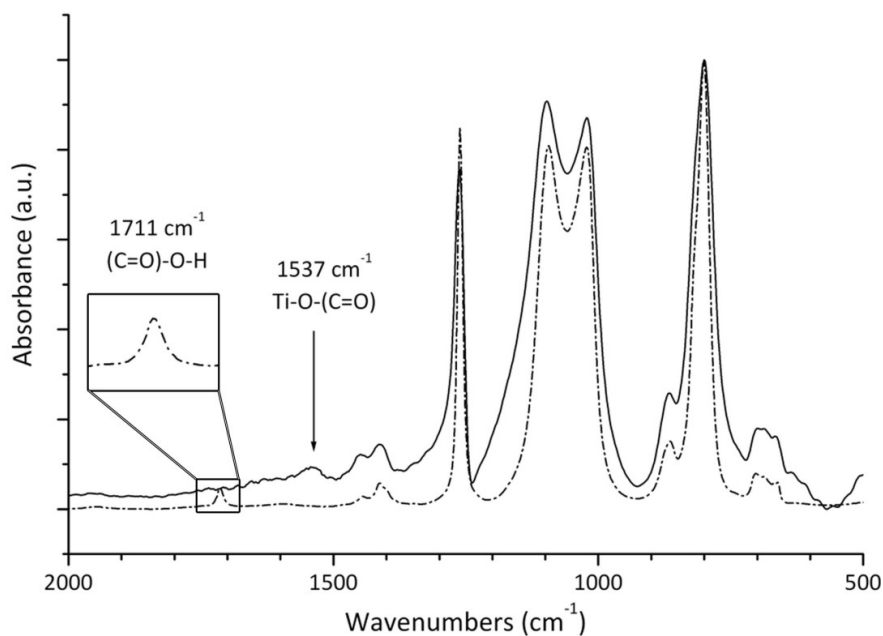


Figure 54. FT-IR spectrum in the range 2000 cm⁻¹ – 500 cm⁻¹ of plain PDMS (broken line) and H-PDMS70 hybrid (solid line)

The latter is attributed, in agreement with previous assignments [99,178], to the stretching vibration of the carbonyl group interacting with titanium atom and its appearance demonstrates formation of organotitanium ester bonds between titanium oxide and PDMS chain ends.

Once the PDMS hybrid is coated on Ta-sputtered samples, the obtained double-layered coating is transparent (Figure 55-A) but, unlike H-PCLb50 hybrid (Figure 49-B), no significant radiopacity enhancement is observed when H-PDMS70 is used as the protective coating of Ta-sputtered PP (Figure 55-B), due to the low percentage of titanium oxide in H-PDMS70 (ca. 10% vs 22% in H-PCLb50).

An interesting result on the PDMS-containing hybrid coating concerns its behavior under bending deformation.

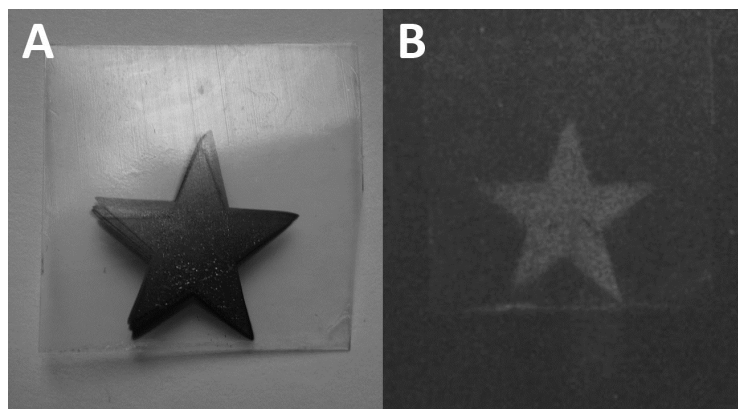


Figure 55. Picture of H-PDMS70-Ta1 sample (A) and corresponding radiographic image (B)

H-PDMS70-Ta1, H-PDMS70-Ta2 and H-PDMS70-Ta3 were deformed according to Figure 52 and SEM observation of the deformed coating surface showed no crack formation, indicating that the H-PDMS70 hybrid coating is able to uniformly follow substrate deformation without breaking.

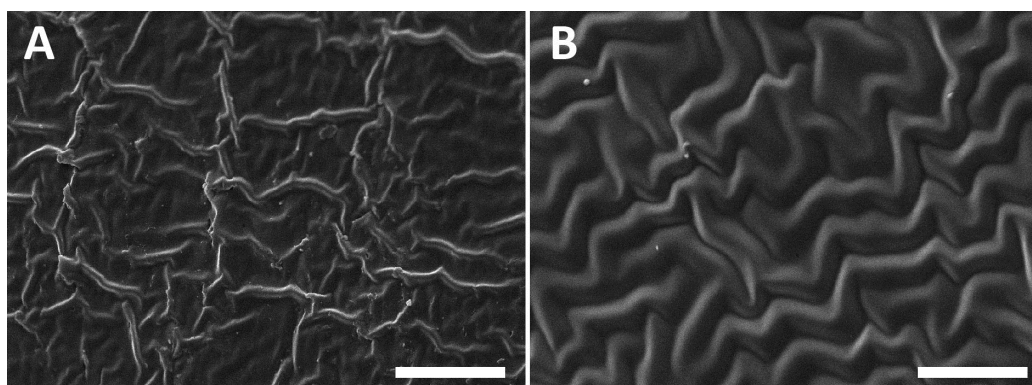


Figure 56. SEM image after bending deformation according to Figure 52 of plain PP sheet (A) and H-PDMS70-Ta1 sample (B) surfaces. White scale bar = 10 μm

The hybrid coating very firmly adheres to the plastic substrate showing no tendency to detach under deformation. As an example, Figure 56 reports SEM images of plain PP sheet (A) and H-PDMS70-Ta1 (B) upon deformation; images reveal how the hybrid coating resembles the PP substrate after partially release of the deformation, without the formation of cracks. These results show that selection of a low- T_g polymeric component able to form a rather loose network via bond formation between chain end functional groups and Titania particles is a good strategy to obtain a hybrid

protective layer able to follow large bending deformations of a radiopaque Ta-sputtered substrate.

Table 12 reports the results of cytotoxicity tests performed on H-PDMS70-Ta1. Cell mortality upon exposure to medium conditioned with the double layered H-PDMS70-Ta1 sample is comparable with that obtained from negative control, taking into account standard deviation. Besides the absence of any evidence of sample-induced mortality, cell counts show that cells are free to proliferate implying that no toxic elements are released from the H-PDMS70-Ta1 material in the culture medium.

Worth pointing out is the fact that after 24 h exposure to medium and subsequent room temperature drying, no weight change was gravimetrically detected for H-PDMS70-Ta1. In addition, neither visual observation nor surface analysis by SEM (Figure 57) revealed appreciable differences before/after medium exposure.

Table 12. Cytotoxicity test results for H-PDMS70-Ta1

Sample	Cell mortality (%) ^a	N° living cells ^b
PP	4.4 (±2.1)	65600
Ta1	4.1 (±3.3)	56600
H-PDMS70-Ta1	5.9 (±2.6)	76800
Positive control ^c	100.0 (±0.0)	0
Negative control ^d	4.9 (±2.4)	77500

^a Values are given as means out of 5 replicates. For each value correspondent standard deviation is reported within brackets.

^b Number of living cells present in each well after 24 hours incubation in medium starting from 50000 seeded cells.

^c Cells exposed to 1mM H₂O₂ solution for 2h.

^d Cells exposed to fresh culture medium for 24h.

These results indicate 24 h water resistance of the coating. The data collected in this work provide evidence of biocompatibility of the double-layered H-PDMS70-Ta1 coatings investigated and suggest that such coatings are very promising materials for applications in the area of radiopaque flexible medical devices.

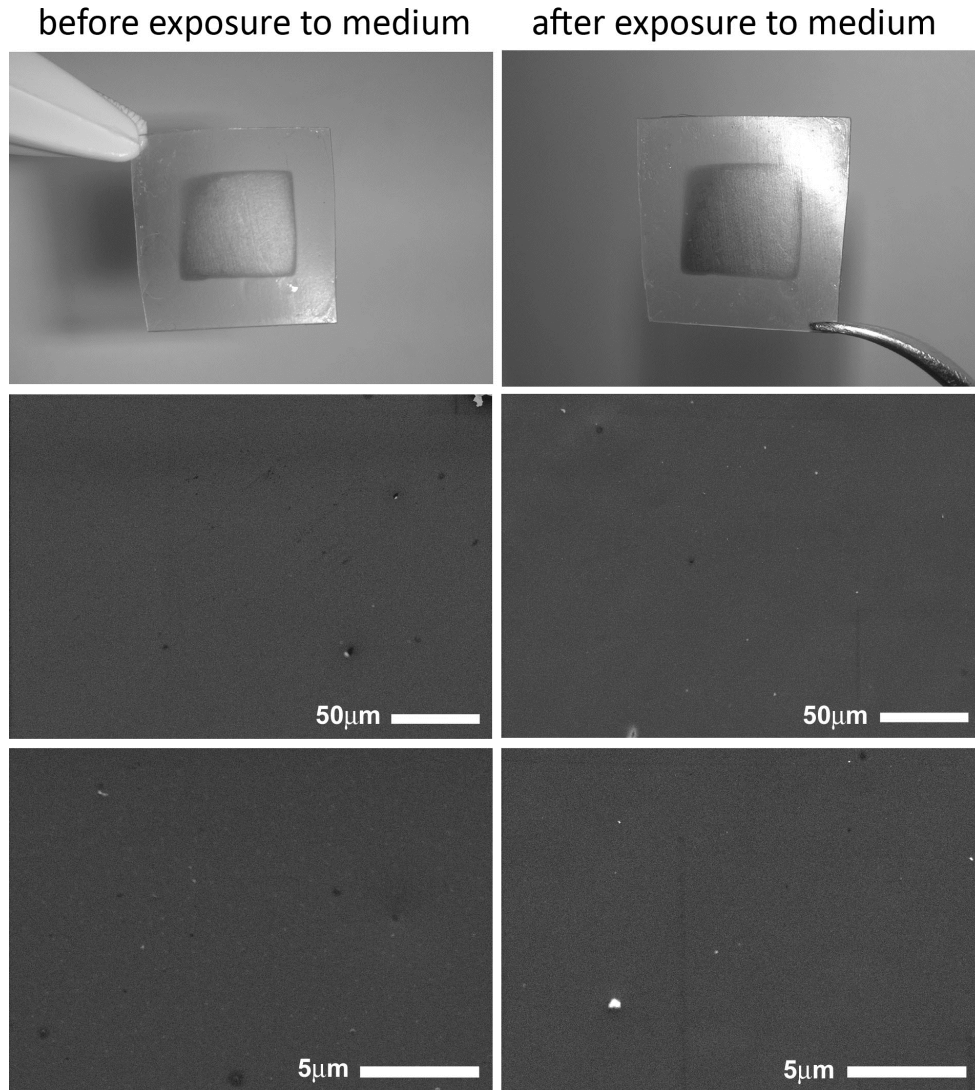


Figure 57. Picture and SEM images of $H_{PDMS-Ta1}$ sample before (left column) and after (right column) 24h exposure to culture medium at 37°C.

In conclusion a two-step procedure for the production of coatings able to enhance radiopacity of medical devices has been described in this Chapter. In the first step a thin layer of tantalum is deposited by sputtering on a plastic substrate. The metallic layer confers to the polymer substrate good X-ray visibility and the correlation found between radiopacity and coating thickness allows to tailor the former simply by controlling sputtering deposition time. The applied metal deposition technique also permits easy shaping of the radiopaque layer, allowing production of radiopaque markers for medical devices that can be unambiguously identified by surgeons during implantation and in subsequent radiological investigations. The second step consists in the application of a protection layer made of an organic-inorganic hybrid material that

can be applied on top of the metallic film either by dip coating or by doctor blade method.

Synthesized PCL-titania and PDMS-titania hybrids strongly adhere to substrates and show good biocompatibility as highlighted by cytotoxicity tests. The PDMS-titania hybrid coating is also characterized by high flexibility that allows it to stand large substrate deformations without detaching nor cracking, thus being suitable for application on flexible devices.

5. PDMS-Titania Hybrids Loaded with Nanoparticles

In the previous Chapter a two-step procedure to obtain a double-layer coating constituted by a radiopaque metallic layer, i.e. tantalum, and a protective biocompatible hybrid layer was described. Such coating is characterized by higher radiopacity than simple hybrid coatings and, when PDMS is employed as the hybrid organic phase, the material is also able to follow high bending deformation, becoming therefore suitable for application on flexible medical devices, such as catheters and guidewires. In this Chapter a simple one-step procedure for the synthesis of material characterized by intermediate radiopacity between plain hybrid material and metal-hybrid double-layer ones is presented. The procedure consists in the suspension of radiopaque nanoparticles (NP) in a solution containing the polymer and the inorganic hybrid precursors, so that sol-gel process occurs in presence of nanoparticles, finally leading to X-ray visible NP-loaded organic-inorganic hybrid materials. The employment of the sol-gel process for the synthesis of such materials allows coating NP-loaded hybrids on a huge variety of substrates, no matter their actual shape. Therefore NP-loaded hybrid materials might be exploited to develop light-weight garments for X-ray protection. In the present thesis, synthesis of PDMS-titania hybrid materials loaded with different amounts of tantalum nanoparticles was studied. Materials were obtained as self-standing films and their radiopacity was evaluated with respect to plain hybrid samples. Furthermore such materials were also coated on cotton textiles.

5.1. Synthesis of PDMS-Titania Hybrids Loaded with Tantalum Nanoparticles

The obtainment of homogeneous nanoparticle dispersions represents a great challenge in the field of nanocomposite fabrication. A method for the production of polymer nanocomposites consists in the addition of nanoparticles to a polymeric solution, followed by sonication, which allows obtaining a homogeneous suspension. Such a suspension can then be casted on a substrate to let the solvent evaporate, finally obtaining a solid nanocomposite. Unfortunately, in absence of interaction between polymer chains and nanoparticles (that can be achieved for example through nanoparticle chemical functionalization), nanoparticles tend to form aggregates and to precipitate before complete solvent evaporation has occurred.

In the present thesis dispersion of tantalum nanoparticles inside PDMS-titania hybrid materials has been attempted. In particular, a dicarboxypropyl-terminated PDMS was employed, on the assumption that carboxyl terminals can react with the inorganic phase precursor (TIPT) during sol-gel process, forming organotitanium ester bonds (see Results and Discussion, paragraph 4.3).

The synthetic procedure developed (see Experimental Part) consists in the addition of a solution of the inorganic hybrid precursor, i.e. TIPT, in a pre-sonicated suspension of tantalum nanoparticles in PDMS/THF solution; the final suspension is then sonicated for 10 min. It is hypothesized that the formation of the hybrid network during the sol-gel process inhibits nanoparticles aggregation thanks to the progressive increase of system viscosity. Furthermore, assuming that tantalum nanoparticles in contact with air oxidize at the surface (thus obtaining the presence of a certain amount of surface Ta-OH groups [179]), it is possible that Ta-O-Ti covalent bonds form between nanoparticles and growing inorganic network during the sol-gel process, thus stabilizing even more the nanoparticles suspension.

Stabilization of different tantalum nanoparticle suspensions has been evaluated in the present thesis through NP suspension optical density measurements versus time. A stable suspension is characterized by a constant value of optical density versus time, while nanoparticles aggregation and precipitation is associated with a progressive decrease in optical density with time. Stability of two Ta nanoparticle suspensions, one in THF and the other in PDMS/THF solution, are compared with a NP suspension in the hybrid precursor mixture in Figure 58. While the presence of the polymer does not

significantly stabilize the NP suspension with respect to the one where NP are suspended in plain solvent, the addition of the hybrid inorganic precursor (TIPT) slow down the rate of NP aggregation and precipitation. Noteworthy, during the initial 6 minutes no decrease of OD is observed. The results of Figure 58 are in line with the hypothesis described above and they show the advantage that can be obtained by suspending nanoparticles in a hybrid precursor mixture instead of suspending them in a plain polymer solution. The synthetic procedure here described might be suitable, therefore, for production of NP-loaded hybrid materials.

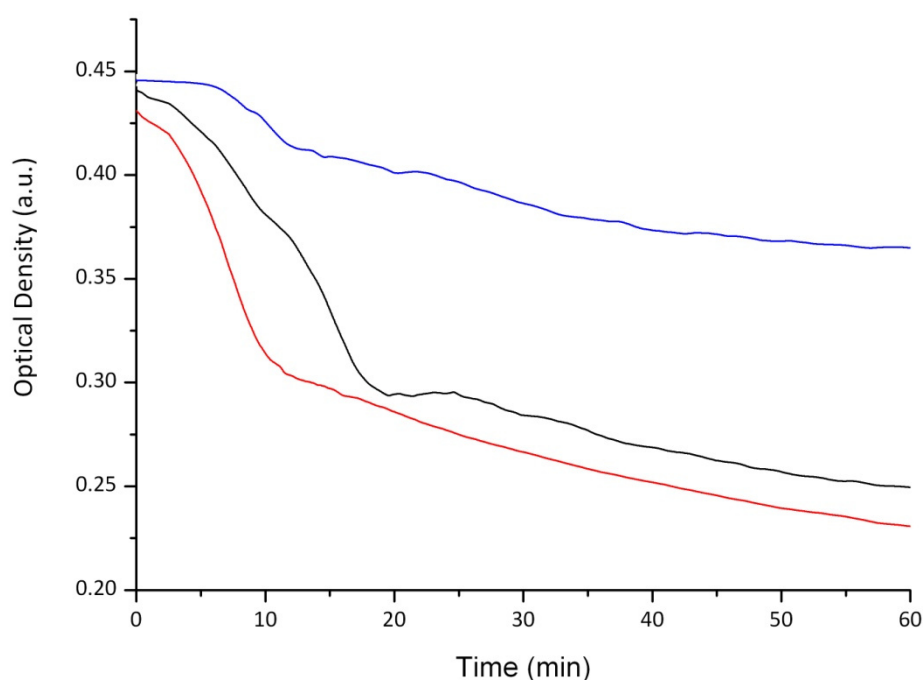
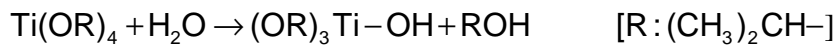


Figure 58. Optical Density vs time for Ta NP suspended in THF (red, 4 mg NP in 8 mL THF), Ta NP suspended in a solution of PDMS in THF (black, 4 mg NP, 183 mg PDMS in 8 mL THF) and Ta NP suspended in a mixture of PDMS and inorganic precursor TIPT in THF (blue, 4 mg NP, 183 mg PDMS and 46 mg TIPT in 8 mL THF). All the suspensions were sonicated for 10 min before measurement.

PDMS-Titania hybrids loaded with different percentages of Ta nanoparticles, i.e. 1, 2, 5 and 10 %-wt, were synthesized starting from a constant PDMS to TIPT weight ratio (80:20); such a high organic to inorganic precursor ratio has been chosen in order to obtain a rather flexible material, since it is reasonable to assume that the presence of tantalum nanoparticles will increase rigidity of the loaded materials with respect to the plain hybrid. Hybrid samples synthesized are labeled H-TaNP-X, where X represents the

weight percentage of the nanoparticles in the final material (i.e. $X = 1, 2, 5$ or 10). Weight percentage of NP in the final material can be easily controlled by choosing the appropriate amount of hybrid precursors and nanoparticles to be added during the synthesis. These quantities were calculated following the procedure described below for H-TaNP-2 as an example: in order to produce 200 mg of final material containing 2%-wt of nanoparticles, 4 mg of Ta NP must be added during the synthesis. Therefore, 196 mg (98%-wt) of the final material will consist of PDMS and TiO_2 . While PDMS doesn't undergo changes during the synthetic procedure, TiO_2 is obtained through hydrolysis and condensation reactions of the TIPT alkoxide precursor during the sol-gel process (Figure 59).

Hydrolysis



Condensation

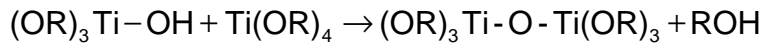
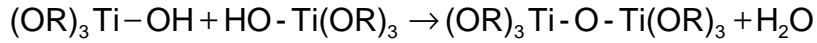


Figure 59. TIPT sol-gel reactions

Starting from a PDMS to TIPT weight ratio of 80/20 and assuming that TIPT hydrolysis and condensation reactions go to completion, the PDMS to TiO_2 ratio R_{PDMS} : R_{TiO_2} in the final material can be obtained through the following equations:

$$R_{TiO_2} = \frac{X_{TIPT} \frac{MW_{TiO_2}}{MW_{TIPT}}}{X_{PDMS} + X_{TIPT} \frac{MW_{TiO_2}}{MW_{TIPT}}} \cdot 100 \quad [Eq.14]$$

$$R_{PDMS} = 100 - R_{TiO_2} \quad [Eq.15]$$

where X_{PDMS} and X_{TIPT} are the weight fractions of PDMS (= 80) and TIPT precursors (= 20) in the feed and MW_{TiO_2} and MW_{TIPT} are the molecular weights of titania and of TIPT respectively. The calculated value is $R_{PDMS}/R_{TiO_2} = 93.4/6.6$, which for 196 mg of the final material, corresponds to 183 mg of PDMS (that must be added during the synthesis) and 13 mg of TiO_2 . Knowing that in the sol-gel process 1 mol of TIPT leads to 1 mol of TiO_2 , the amount of TIPT to weigh can be easily obtained and corresponds to 46 mg. All synthesized materials are optically transparent self-standing film (thickness approximately 100 μ m), as shown in Figure 60, where a picture of H-TaNP2 sample is reported as an example. The increase of Ta nanoparticles amount in the hybrids is associated with a darker color of the final material, which maintains, however, its intrinsic transparency.

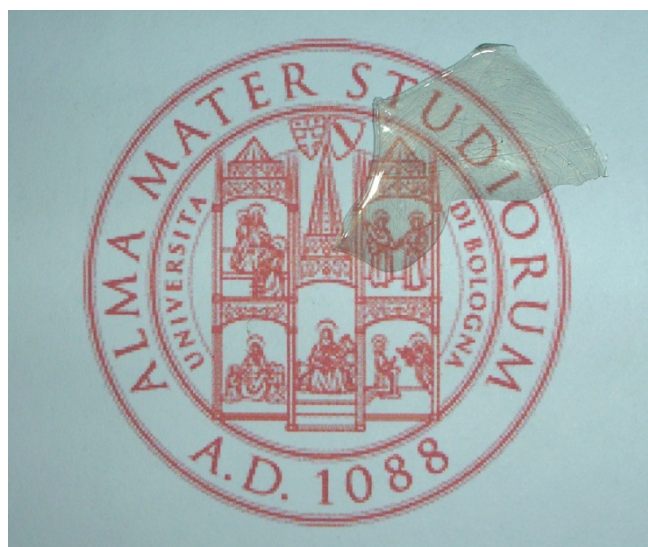


Figure 60. Picture of H-TaNP2 sample.

With the aim of gaining information regarding the presence of interactions between the different phases, FT-IR spectra of hybrid samples were recorded. Figure 61 compares the spectra of H-TaNP10 sample with that of plain PDMS-Titania hybrid and with the spectrum of Ta NP. The spectrum of Ta NP (Figure 61-A) is in good agreement with those reported in the literature for tantalum oxide Ta_2O_5 , confirming the formation of an oxide layer at nanoparticle surface [180,181,182,183]. The spectrum displays a broad multiple absorption region in the range 1000 cm^{-1} - 500 cm^{-1} , where vibrations of Ta-O-Ta bonds are located. In addition, bands related to Ta-OH bond

vibrations are present at 3425cm^{-1} (stretching) and 1082cm^{-1} (bending) [181,183], confirming that hydroxide groups able to react during sol-gel process exist at the nanoparticle surface.

The plain hybrid spectrum (Figure 61-B) shows characteristic bands of PDMS (2964cm^{-1} CH_3 stretching; 1260cm^{-1} CH_3 bending; 1094cm^{-1} and 1021cm^{-1} Si-O-Si stretching; 800cm^{-1} Si-C stretching) [177] and, in addition, a band at 1539cm^{-1} which is attributed, in agreement with previous assignments [99,178] (see Results and Discussion, Paragraph 4.3), to the stretching vibration of the carbonyl group interacting with titanium atom. This latter band demonstrates formation of organotitanium ester bonds between titanium oxide and PDMS chain ends.

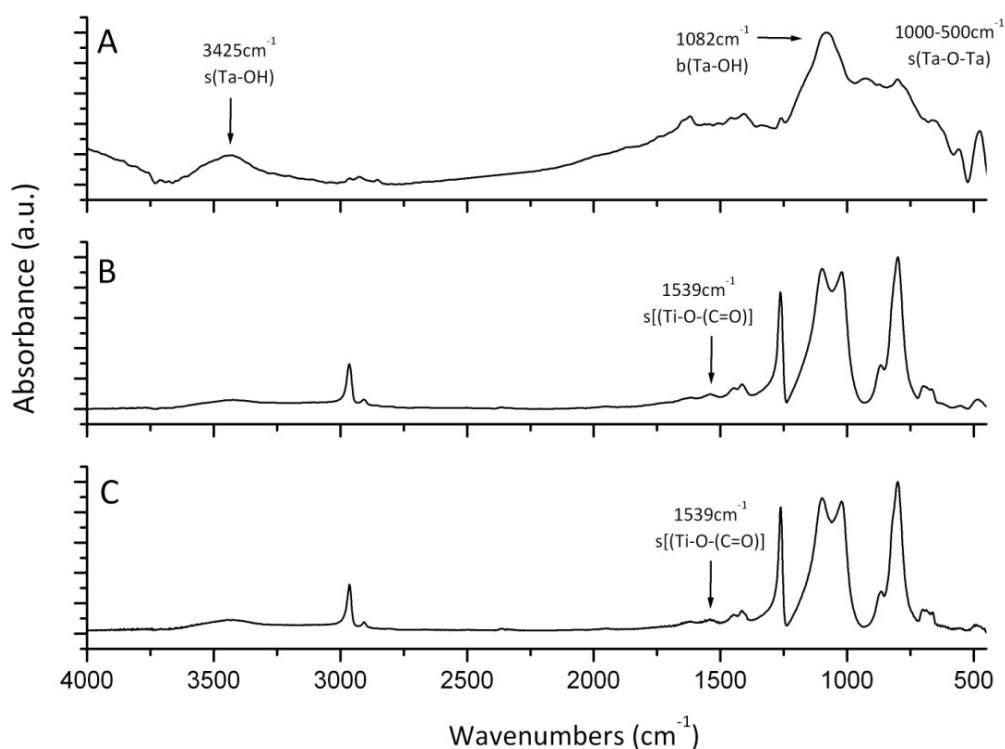


Figure 61. FT-IR spectra in the range $4000\text{cm}^{-1} - 500\text{cm}^{-1}$ with band attribution.
A: Tantalum NP, B: H-PDMS80 and C: H-TaNP10.

Comparison of the plain hybrid spectrum with the one corresponding to H-TaNP10 (Figure 61-C) reveals that no significant differences exist between the two spectra, both in terms of band position and band intensity. The absence of bands related to the Ta phase in the loaded hybrid spectrum might be explained considering that the

overall amount of Ta NP in the sample is relatively low; absorption bands associated to the Ta phase, that overlap hybrid bands in the spectrum, might be not intense enough to be detectable.

All samples were then analyzed using X-ray radiographic equipment (mammograph) in order to verify their radiopacity and the obtained X-ray images are reported in Figure 62. It is clearly seen that radiopacity of the hybrid samples increases with Ta NP amount in the hybrid.

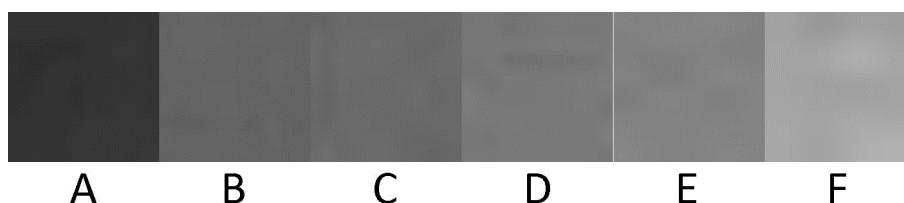


Figure 62. X-ray images of A: background, B: H-PDMS80 (thickness 119 μm), C: H-TaNP1 (thickness 98 μm), D: H-TaNP2 (thickness 101 μm), E: H-TaNP5 (thickness 84 μm) and F: H-TaNP10 (thickness 86 μm). Brighter pictures correspond to higher radiopacity.

Radiopacity values for the four Ta loaded hybrids and for plain PDMS-Titania hybrid were calculated according to ASTM standard method F640 [166] from digitalized radiographic images as the difference in pixel intensity between sample tested and background (see Results and Discussion, Paragraph 4.1) and results are shown in Table 10. For both H-TaNP5 and H-TaNP10 samples a thicker sample was also synthesized and its radiopacity was measured.

As already suggested by simple observation of the radiographs in Figure 63, the value of relative pixel intensity, for samples of comparable thickness, increases with the weight percentage of tantalum nanoparticles in the hybrid.

Theoretically, radiopacity of samples with given thickness should be directly proportional to their Ta NP content (i.e. weight percentage). In order to confirm this hypothesis, the NP weight percentage (w_{NP}^{100}) for a hypothetical sample 100 μm thick showing the same radiopacity as that of the actually synthesized samples was calculated as follows and is reported in Table 13:

$$W_{NP}^{100} = \frac{W_{NP}^{synth} \cdot t^{synth}}{t^{100}} \quad [\text{Eq.16}]$$

where w_{NP}^{synth} is the Ta NP weight percentage in the synthesized sample, t^{synth} is the thickness of the synthesized sample and t^{100} is equal to 100 μm . The calculation was made on the assumption that flat samples of different thickness containing the same amount of NP have equal radiopacity values.

Table 13. Radiopacity values of self-standing hybrid samples loaded with Ta NP.

Sample	NP content (%-wt)	Thickness (μm)	Radiopacity ^a	Normalized NP content (%wt) ^b
H-PDMS80	0	119	11	0
H-TaNP1	1	98	19	0.98
H-TaNP2	2	101	23	2.02
H-TaNP5	5	91	32	4.55
	5	209	51	8.60
H-TaNP10	10	86	42	10.45
	10	160	71	16.0

^a Calculated as the difference between the pixel intensity of the sample in the radiographic image and the pixel intensity of the background (see background in Figure 62).

^b Theoretical weight percentage of nanoparticles in a sample 100 μm thick having the radiopacity value reported in the previous column.

In Figure 63 radiopacity values are plotted as a function of the “normalized” NP weight percentage values, showing a good linear correlation between radiopacity and amount of tantalum nanoparticles. This result demonstrates that it is possible to obtain hybrid materials with controlled radiopacity by simply adjusting the relative content of radiopaque nanoparticles. When the radiopaque material is used as a coating, two options are available: either to increase coating thickness at constant NP concentration, or to increase the NP content while keeping the coating layer thickness constant.

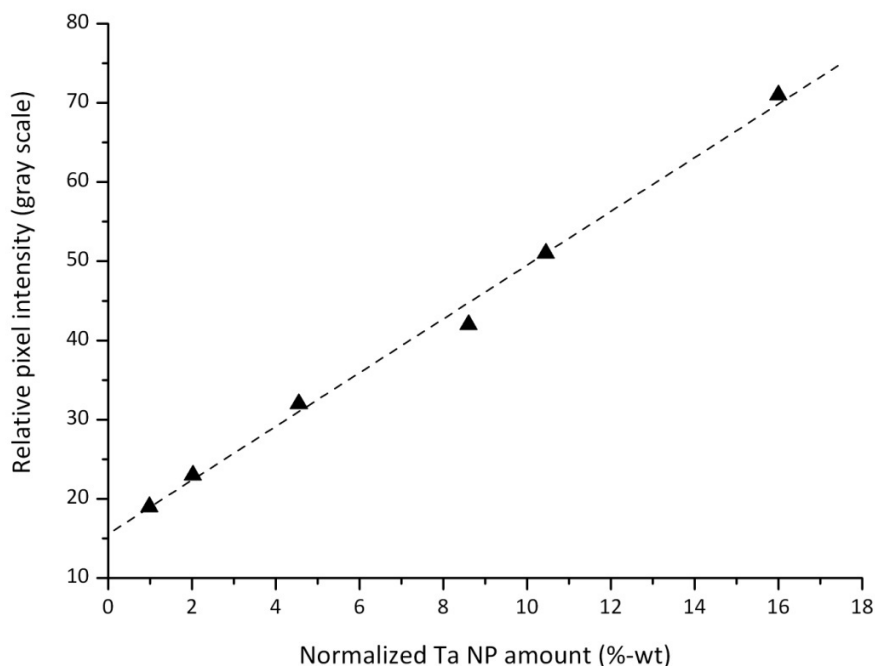


Figure 63. Radiopacity values, reported as relative pixel intensity calculated from a digital radiographic image, as a function of Ta nanoparticles amount “normalized” to a sample thickness of 100 μm , calculated following Eq.16.

As already described in the Introduction, the production of X-ray shielding clothes for the protection of medical staff during interventional fluoroscopy, could be a powerful tool for the prevention of pathologies deriving from chronic X-ray exposure, such as skin damages, injuries to the eye lenses and also some kind of cancer (see Introduction, Paragraph 2.4). Hence, radiopaque NP-loaded hybrids were deposited on cotton textiles via dip coating. All fabrics that were coated with such NP-loaded hybrids showed a quite pleasant hand. SEM micrographs of cotton coated with H-TaNP10 are shown in Figure 64, where they are compared with pictures of the untreated fabric at the same magnification. Remarkably, no appreciable differences between coated and uncoated fabric are observed.

Observing Figure 64-B and Figure 64-D, it is interesting to note that the hybrid is able to coat single fibers of the yarn rather than coating the yarn as a whole. Openings between yarns are maintained and therefore fabric breathability is preserved.

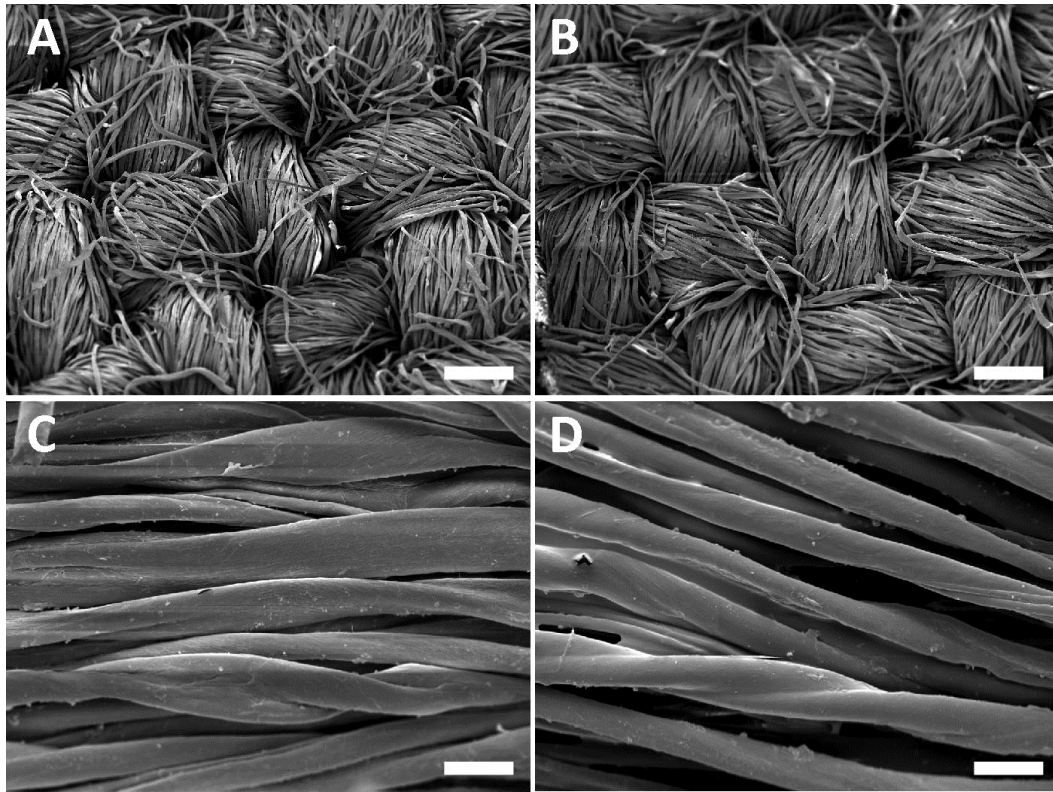


Figure 64. SEM micrographs at different magnification of cotton fabric (A and C) and of cotton fabric coated with H-TaNP10 (B and D). Bar: 200 μ m in A and B, 20 μ m in C and D.

In addition, thanks to the presence of the PDMS phase in the hybrid material, the coated fabric becomes water impermeable. Figure 65 shows indeed how the water wettability of the cotton textiles dramatically changes when the fabric is coated with the loaded hybrid.

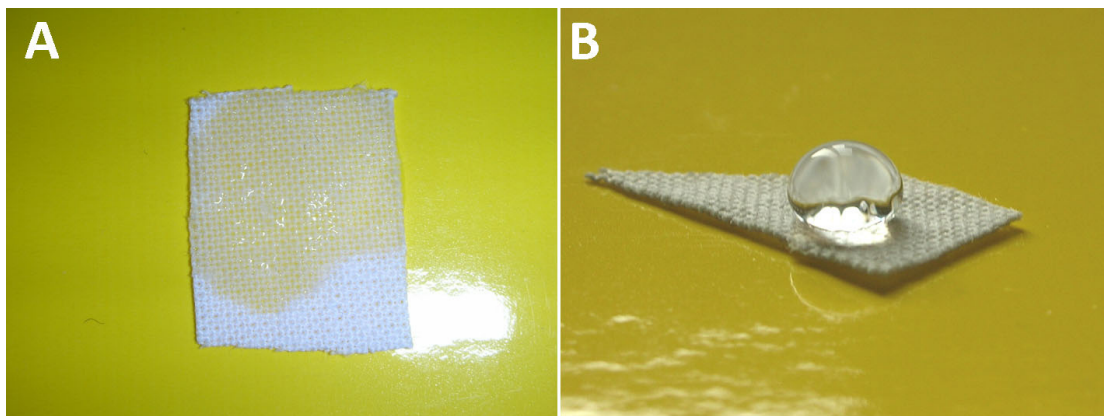


Figure 65. Water wettability of A: cotton fabric and B: cotton fabric coated with H-TaNP10.

The results discussed above demonstrate an easy route to provide radiopacity to textiles with many possible applications, for example, in the field of personal X-ray protective equipment. The synthetic procedure developed allows the addition of radiopaque tantalum nanoparticles on PDMS-Titania hybrid materials in a one step process. The presence of such nanoparticles provides additional radiopacity to the hybrid materials, with radiopacity proportionally increasing with Ta NP content. Similar to plain hybrid materials, loaded hybrids are easily coated on textiles providing radiopacity and water resistance to fabrics, without affecting material breathability. Medical staff occupied in endovascular interventions may take great advantage of light and comfortable garments able to shield from dangerous X-rays.

Acknowledgements

I gratefully thank Dr. Massimo Marcaccio (Dip. Chimica "G.Ciamician", Bologna University) and Prof. Andrea Alessandrini (Dip. Fisica, Modena and Reggio Emilia University) for AFM characterization, Prof. Stefano Mignani and Mrs. Rita Luciani (Centro Mammografico, Policlinico Sant'Orsola Malpighi, Bologna University) for the radiographic images, Prof. Gianandrea Pasquinelli and Dr. Annalisa Pacilli (Dipartimento Clinico di Scienze Radiologiche e Istocitopatologiche, Sezione di Patologia Clinica, Policlinico Sant'Orsola Malpighi, Bologna University) for cytotoxicity tests, Prof. Gianluca Faggioli and Prof. Andrea Stella (Dipartimento di Scienze Chirurgiche Specialistiche e Anestesiologiche, Policlinico Sant'Orsola Malpighi, Bologna University) for fluoroscopic images. A special thanks to Prof. Mariastella Scandola (Dip. Chimica "G.Ciamician", Bologna University) for tutoring the PhD laboratory research activity.

Bibliography

1. World Health Organization *The World Health Report 2004 - Statistical Annex* **2004**, 121-123.
2. Lloyd-Jones, D., Adams, R. J., Brown, T. M., Carnethon, M., Dai, S., De Simone, G., Ferguson, T. B., Ford, E., Furie, K., Gillespie, C., Go, A., Greenlund, K., Haase, N., Hailpern, S., Ho, P. M., Howard, V., Kissela, B., Kittner, S., Lackland, D., Lisabeth, L., Marelli, A., McDermott, M. M., Meigs, J., Mozaffarian, D., Mussolino, M., Nichol, G., Roger, V. L., Rosamond, W., Sacco, R., Sorlie, P., Stafford, R., Thom, T., Wasserthiel-Smoller, S., Wong, N. D., Wylie-Rosett, J., and Amer Heart Assoc Stat Comm Stroke *Circulation* **2010**, *121*, E46-E215.
3. Orford, J. L., Selwyn, A. P., Ganz, P., Popma, J. J., and Rogers, C. *American Journal of Cardiology* **2000**, *86*, 6H-11H.
4. Ross, R. *Nature* **1993**, *362*, 801-809.
5. Ratner, B. D., Hoffman, A. S., Schoen, F. J., and Lemons, J. E. In *Biomaterials science: an introduction to materials in medicine*, Elsevier Academic Press 2004.
6. Donnan, G. A., Fisher, M., Macleod, M., and Davis, S. M. *Lancet* **2008**, *371*, 1612-1623.
7. Hallett, J. W., Mills, J. L., Earnshaw, J. J., Reekers, J. A., and Rooke, T. W. In *Comprehensive Vascular and Endovascular Surgery*, 2nd Edition ed.; Mosby Elsevier: Philadelphia, 2009.
8. Flynn, R. W. V., MaWalter, R. S. M., and Doney, A. S. F. *Neuropharmacology* **2008**, *55*, 250-256.
9. Shammas, N. W. *Vasc Health Risk Manag* **2007**, *3*, 229-234.
10. Aronow, W. S. *Cardiol Rev* **2005**, *13*, 61-68.
11. Venkatraman, S., Boey, F., and Lao, L. L. *Progress in Polymer Science* **2008**, *33*, 853-874.
12. Greenwald, S. E. and Berry, C. L. *Journal of Pathology* **2000**, *190*, 292-299.
13. Sarkar, S., Schmitz-Rixen, T., Hamilton, G., and Seifalian, A. M. *Medical & Biological Engineering & Computing* **2007**, *45*, 327-336.

14. Wang, X. W., Lin, P., Yao, Q. H., and Chen, C. Y. *World Journal of Surgery* **2007**, *31*, 682-689.
15. Isenberg, B. C., Williams, C., and Tranquillo, R. T. *Circulation Research* **2006**, *98*, 25-35.
16. Niklason, L. E., Gao, J., Abbott, W. M., Hirschi, K. K., Houser, S., Marini, R., and Langer, R. *Science* **1999**, *284*, 489-493.
17. Couet, F., Rajan, N., and Mantovani, D. *Macromolecular Bioscience* **2007**, *7*, 701-718.
18. Mani, G., Feldman, M. D., Patel, D., and Agrawal, C. M. *Biomaterials* **2007**, *28*, 1689-1710.
19. Hanawa, T. *Journal of Artificial Organs* **2009**, *12*, 73-79.
20. Koster, R., Vieluf, D., Kiehn, M., Sommerauer, M., Kahler, J., Baldus, S., Meinertz, T., and Hamm, C. W. *Lancet* **2000**, *356*, 1895-1897.
21. Heintz, C., Riepe, G., Birken, L., Kaiser, E., Chakfe, N., Morlock, M., Delling, G., and Imig, H. *Journal of Endovascular Therapy* **2001**, *8*, 248-253.
22. BergerGorbet, M., Broxup, B., Rivard, C., and Yahia, L. H. *Journal of Biomedical Materials Research* **1996**, *32*, 243-248.
23. O'Brien, B. and Carroll, W. *Acta Biomaterialia* **2009**, *5*, 945-958.
24. Virmani, R., Guagliumi, G., Farb, A., Musumeci, G., Grieco, N., Motta, T., Mihalcsik, L., Tsepili, M., Valsecchi, O., and Kolodgie, F. D. *Circulation* **2004**, *109*, 701-705.
25. Munoz, J. J. and Ribes, R. In *Learning Vascular and Interventional Radiology*, 1st Edition ed.; Springer: New York, 2010.
26. Deem, M. E. US Patent 5840046, **1998**.
27. Schneider, P. A. In *Endovascular Skills: Guidewire and Catheter Skills for Endovascular Surgery*, 3rd Edition ed.; Informa Healthcare 2008.
28. Jonas, W. B. In *Mosby's Dictionary of Complementary and Alternative Medicine*, Mosby Elsevier 2004.
29. Barrett, C. S. In *Structure of metals*, McGraw Hill Book Company Inc 1943.

30. Wang, Y. PCT Patent Application WO2009126479 , **2009**.
31. Krufft, M. A. B., Benzina, A., Blezer, R., and Koole, L. H. *Biomaterials* **1996**, *17*, 1803-1812.
32. Mirji, S. P., Listro, A., O'Neil, C. J., Areva, S., Acquarulo, L., and Johnson, L. *ANTEC 2008 Plastics: Annual Technical Conference Proceedings* **2008**, 2213-2217.
33. Simpson, J. A., Boylan, J. F., and Cornish, W. US Patent Application 20090099645 , **2009**.
34. Allen, J. and Birdsall, M. PCT Patent Application WO2009099958 , **2009**.
35. Li, J. US Patent Application 20090281558 , **2009**.
36. Glocker, D. A. and Romach, M. M. *SVC - 51st Annual Technical Conference Proceedings* **2008**, 199-204.
37. Chan, W. A., Bini, T. B., Venkatraman, S. S., and Boey, F. Y. C. *Journal of Biomedical Materials Research Part A* **2006**, *79A*, 47-52.
38. Constant, M. J., Keeley, E. M., and Cruise, G. M. *Journal of Biomedical Materials Research Part B-Applied Biomaterials* **2009**, *89B*, 306-313.
39. Wang, X., Ye, J., and Wang, Y. *Acta Biomaterialia* **2007**, *3*, 757-763.
40. Rusu, M. C., Rusu, M., Popa, M., Delaite, C., and Riess, G. *Polymer Bulletin* **27-6-2007**, *59*, 25-30.
41. Kiran, S., James, N. R., Joseph, R., and Jayakrishnan, A. *Biomaterials* **2009**, *30*, 5552-5559.
42. Mawad, D., Poole-Warren, L. A., Martens, P., Koole, L. H., Slots, T. L. B., and Hooy-Corstjens, C. S. J. *Biomacromolecules* **30-11-2007**, *9*, 263-268.
43. Carbone, A. L., Song, M., and Urich, K. E. *Biomacromolecules* **2008**, *9*, 1604-1612.
44. O'Brien, B., Stinson, J., and Carroll, W. *Acta Biomaterialia* **2008**, *4*, 1553-1559.
45. Pacetti, S. and Mroz, J. US Patent US6355058 , **2002**.
46. Carlson, J. M., Carr, S., Devereaux, P., Haverty, D., Lavelle, S., McGloughlin, T., and Tofail, S. PCT Patent Application WO2008030517 , **2008**.

47. Makita, M., Yamakado, K., Nakatsuka, A., Takaki, H., Inaba, T., Oshima, F., Katayama, H., and Takeda, K. *Radiation Medicine* **2008**, *26*, 533-538.
48. Manero, J. M., Ginebra, M. P., Gil, F. J., Planell, J. A., Delgado, J. A., Morejon, L., Artola, A., Gurruchaga, M., and Goni, I. *Proceedings of the Institution of Mechanical Engineers Part H-Journal of Engineering in Medicine* **2004**, *218*, 167-172.
49. Thompson, P. J. and Lee, N. T. US Patent Application US20090069879 , **2009**.
50. Ohri, R. and Steckel, M. US Patent Application US2009259286 , **2009**.
51. Yribarren, T. R., Oepen, R. V., Coffey, L., Rieth, T., and Zucker, A. US Patent Application 20080097404 , **2008**.
52. Lorenzo, J. A. US Patent Application 20080243227 , **2008**.
53. Wu, P. P. US Patent Application US20080015684 , **2008**.
54. Young, E., Shrivastava, S., Borg, R., Shumer, D., Shumer, D. H., Simeon, P., and Osman, K. US Patent Application US20090005858 , **2009**.
55. Balgobin, K., Mitelberg, V., Rainer, J. T., and Thinnes, J. H. US Patent Application US20080269675 , **2008**.
56. Cheng, Y., Cai, W., Li, H. T., and Zheng, Y. F. *Journal of Materials Science* **2006**, *41*, 4961-4964.
57. Macionczyk, F., Gerold, B., and Thull, R. *Surface & Coatings Technology* **2001**, *142*, 1084-1087.
58. Edelman, E. R., Seifert, P., Groothuis, A., Morss, A., Bornstein, D., and Rogers, C. *Circulation* **2001**, *103*, 429-434.
59. Martin, C. J. *Radiation Protection Dosimetry* **2009**, *136*, 140-157.
60. *The Society of Interventional Radiology* **2005**, 1-5.
61. Mahesh, M. *Radiographics* **2001**, *21*, 1033-1045.
62. Faulkner, K. and Vano, E. *Radiation Protection Dosimetry* **2001**, *94*, 95-98.
63. Yoshinaga, S., Mabuchi, K., Sigurdson, A. J., Doody, M. M., and Ron, E. *Radiology* **2004**, *233*, 313-321.

64. Via, W. F. US Patent US3569713, **1971**.
65. Hollands, G. US Patent US30552799, **1962**.
66. Demeo, R. and Kucherovsky, J. US Patent US6828578, **2004**.
67. Jensen, S. D. US Patent Application 20100210161 , **2010**.
68. Mammeri, F., Le Bourhis, E., Rozes, A., and Sanchez, C. *Journal of Materials Chemistry* **2007**, *15*, 3787-3811.
69. Schmidt, H. *Journal of Non-Crystalline Solids* **1985**, *73*, 681-691.
70. Wilkes, G. L., Orler, B., and Huang, H. H. *Polymer Preprints* **1985**, *26*, 300-302.
71. Gilman, J. W., Jackson, C. L., Morgan, A. B., Harris, R., Manias, E., Giannelis, E. P., Wuthenow, M., Hilton, D., and Phillips, S. H. *Chemistry of Materials* **17-7-2000**, *12*, 1866-1873.
72. Chiang, C. L. and Chang, R. C. *Composites Science and Technology* **2008**, *68*, 2849-2857.
73. Choi, C. G. and Bae, B. S. *Organic Electronics* **2007**, *8*, 743-748.
74. Gomez-Romero, P. *Advanced Materials* **2001**, *13*, 163-174.
75. Godovski, D. Y. *Advances in Polymer Science* **1995**, *119*, 78-122.
76. Sanchez, C., Lebeau, B., Chaput, F., and Boilot, J. P. *Advanced Materials* **2003**, *15*, 1969-1994.
77. Caseri, W. *Macromolecular Rapid Communications* **2000**, *21*, 705-722.
78. Sanchez, C. and Ribot, F. *New Journal of Chemistry* **1994**, *18*, 1007-1047.
79. Brinker, J. C. and Sherer, G. In *Sol-Gel Science: The Physics and Chemistry of Sol-Gel Processing*, Academic Press: San Diego, 1990.
80. Hench, L. L. and West, J. K. *Chemical Reviews* **1-1-1990**, *90*, 33-72.
81. Judeinstein, P. and Sanchez, C. *Journal of Materials Chemistry* **1996**, *6*, 511-525.

82. Livage, J., Henry, M., and Sanchez, C. *Progress in Solid State Chemistry* **1988**, *18*, 259-341.
83. Wen, J. and Wilkes, G. L. *Chemistry of Materials* **14-8-1996**, *8*, 1667-1681.
84. Takahashi, R., Takenaka, S., Sato, S., Sodesawa, T., Ogura, K., and Nakanishi, K. *Journal of the Chemical Society-Faraday Transactions* **1998**, *94*, 3161-3168.
85. Schmidt, H., Scholze, H., and Kaiser, A. *Journal of Non-Crystalline Solids* **1984**, *63*, 1-11.
86. Bradley, D. C. *Adv Chem Serv* **1959**, *23*, 10-
87. Toki, M., Chow, T. Y., Ohnaka, T., Samura, H., and Saegusa, T. *Polymer Bulletin* **1992**, *29*, 653-660.
88. Morikawa, A., Iyoku, Y., Kakimoto, M., and Imai, Y. *Journal of Materials Chemistry* **1992**, *2*, 679-690.
89. Novak, B. M. and Davies, C. *Macromolecules* **1991**, *24*, 5481-5483.
90. Yamada, N., Yoshinaga, I., and Katayama, S. *Journal of Materials Chemistry* **1997**, *7*, 1491-1495.
91. Katayama, S., Kubo, Y., and Yamada, N. *Journal of the American Ceramic Society* **2002**, *85*, 1157-1163.
92. Sanchez, C., Livage, J., Henry, M., and Babonneau, F. *Journal of Non-Crystalline Solids* **1988**, *100*, 65-76.
93. Huang, H. and Wilkes, G. L. *Polymer Bulletin* **1-11-1987**, *18*, 455-462.
94. Wang, B. and Wilkes, G. L. *Journal of Polymer Science Part A: Polymer Chemistry* **1991**, *29*, 905-909.
95. Noell, J. L. W., Wilkes, G. L., Mohanty, D. K., and McGrath, J. E. *Journal of Applied Polymer Science* **1990**, *40*, 1177-1194.
96. Messori, M., Toselli, A., Pilati, F., Fabbri, E., Fabbri, P., Pasquali, L., and Nannarone, S. *Polymer* **2004**, *45*, 805-813.
97. Kweon, J. O. and Noh, S. T. *Journal of Applied Polymer Science* **2001**, *81*, 2471-2479.

98. Tian, D., Dubois, P., and Jerome, R. *Journal of Polymer Science Part A: Polymer Chemistry* **1997**, *35*, 2295-2305.
99. Mazzocchetti, L., Scandola, M., and Pollicino, A. *Polymer* **2008**, *49*, 5215-5224.
100. Sanchez, C., Julian, B., Belleville, P., and Popall, M. *Journal of Materials Chemistry* **2005**, *15*, 3559-3592.
101. Wen, J., Vasudevan, V. J., and Wilkes, G. L. *Journal of Sol-Gel Science and Technology* **1995**, *5*, 115-126.
102. Kasemann, R. and Schmidt, H. *New Journal of Chemistry* **1994**, *18*, 1117-1123.
103. Hazan, I. and Rummel, M. K. US Patent 5162426 US5162426, **1992**.
104. Bico, J., Marzolin, C., and Quere, D. *Europhysics Letters* **1999**, *47*, 220-226.
105. Akamatsu, Y., Makita, K., Inaba, H., Nakazumi, H., and Minami, T. *Journal of Sol-Gel Science and Technology* **2000**, *19*, 387-391.
106. Lapidot, N., Gans, O., Biagini, F., Sosonkin, L., and Rottman, C. *Journal of Sol-Gel Science and Technology* **2003**, *26*, 67-72.
107. Mazzocchetti, L., Sandri, S., Scandola, M., Bergia, A., and Zuccheri, G. *Biomacromolecules* **12-2-2007**, *8*, 672-678.
108. Reetz, M. T. *Advanced Materials* **1997**, *9*, 943-&.
109. Houbertz, R., Domann, G., Cronauer, C., Schmitt, A., Martin, H., Park, J. U., Frohlich, L., Buestrich, R., Popall, M., Streppel, U., Dannberg, P., Wachter, C., and Brauer, A. *Thin Solid Films* **2003**, *442*, 194-200.
110. Houbertz, R., Domann, G., Schulz, J., Olsowski, B., Frohlich, L., and Kim, W. S. *Applied Physics Letters* **2004**, *84*, 1105-1107.
111. Houbertz, R., Frohlich, L., Popall, M., Streppel, U., Dannberg, P., Brauer, A., Serbin, J., and Chichkov, B. N. *Advanced Engineering Materials* **2003**, *5*, 551-555.
112. Popall, M., Houbertz, R., Frohlich, L., Streppel, U., Dannberg, P., Westenhofer, S., and Gale, M. *Glass Science and Technology* **2003**, *76*, 53-58.
113. Belleville, P., Bonnin, C., and Priotton, J. J. *Journal of Sol-Gel Science and Technology* **2000**, *19*, 223-226.

114. Popall, M., Buestrich, R., Semrau, G., Eichinger, G., Andrei, M., Parker, W. O., Skaarup, S., and West, K. *Electrochimica Acta* **2001**, *46*, 1499-1508.
115. Zoppi, R. A., deCastro, C. R., Yoshida, I. V. P., and Nunes, S. P. *Polymer* **1997**, *38*, 5705-5712.
116. Deng, Q., Moore, R. B., and Mauritz, K. A. *Journal of Applied Polymer Science* **1998**, *68*, 747-763.
117. Kamitakahara, M., Kawashita, M., Miyata, N., Kokubo, T., and Nakamura, T. *Journal of Materials Science-Materials in Medicine* **2007**, *18*, 1117-1124.
118. Chen, Q., Miyaji, F., Kokubo, T., and Nakamura, T. *Biomaterials* **1999**, *20*, 1127-1132.
119. Miyata, N., Fuke, K. I., Chen, Q., Kawashita, M., Kokubo, T., and Nakamura, T. *Journal of the Ceramic Society of Japan* **2003**, *111*, 555-559.
120. Maeda, H., Kasuga, T., and Hench, L. L. *Biomaterials* **2006**, *27*, 1216-1222.
121. Manzano, M., Salinas, A. J., and Vallet-Regi, M. *Progress in Solid State Chemistry* **2006**, *34*, 267-277.
122. Li, R., Nie, K., Shen, X., and Wang, S. *Materials Letters* **2007**, *61*, 1368-1371.
123. Pasquinelli, G., Pacilli, A., Alviano, F., Foroni, L., Ricci, F., Valente, S., Orrico, C., Lanzoni, G., Buzzi, M., Tazzari, P. L., Pagliaro, P., Stella, A., and Bagnara, G. P. *Cytotherapy* **2010**, *12*, 275-287.
124. In *Polymer handbook*, 4th ed.; Brandrup, J., Immergut, E. H., and Grulke, E. A. Eds.; John Wiley and Sons, Inc.: New York, 1999.
125. Blanchard, J., In, M., Schaudel, B., and Sanchez, C. *European Journal of Inorganic Chemistry* **1998**, 1115-1127.
126. Blanchard, J., Ribot, F., Sanchez, C., Bellot, P. V., and Trokiner, A. *Journal of Non-Crystalline Solids* **2-3-2000**, *265*, 83-97.
127. Boettcher, S. W., Bartl, M. H., Hu, J. G., and Stucky, G. D. *Journal of the American Chemical Society* **13-7-2005**, *127*, 9721-9730.
128. Boettcher, S. W., Fan, J., Tsung, C. K., Shi, Q., and Stucky, G. D. *Accounts of Chemical Research* **18-9-2007**, *40*, 784-792.

129. Hagan, D. B., Leng, F. J., Smith, P. M., Snow, M., and Watson, A. *International Journal of Cosmetic Science* **1997**, *19*, 271-280.
130. Mazzocchetti, L., Scandola, M., Amerio, E., Malucelli, G., and Marano, C. *Macromolecular Chemistry and Physics* **2006**, *207*, 2103-2111.
131. Ceccorulli, G., Zini, E., and Scandola, M. *Macromolecular Chemistry and Physics* **2006**, *207*, 864-869.
132. Malucelli, G., Priola, A., Sangermano, M., Amerio, E., Zini, E., and Fabbri, E. *Polymer* **15-4-2005**, *46*, 2872-2879.
133. ASTM D 3363, Standard Test Method for Film Hardness by Pencil Test , **2005**.
134. CIE Report 134/1, Standardization of the terms UV-A1, UV-A2 and UV-B , **1999**.
135. Canada, J., Esteve, A., Marin, M. J., Utrillas, M. P., Tena, F., and Maitinez-Lozano, J. A. *International Journal of Climatology* **2008**, *28*, 693-702.
136. Knifton, J. F. and Duranleau, R. G. *Journal of Molecular Catalysis* **1991**, *67*, 389-399.
137. Haba, O., Itakura, I., Ueda, M., and Kuze, S. *Journal of Polymer Science Part A: Polymer Chemistry* **1999**, *37*, 2087-2093.
138. Harris, R. F. *Journal of Applied Polymer Science* **1992**, *44*, 605-617.
139. Shuster, M., Narkis, M., and Siegmann, A. *Journal of Applied Polymer Science* **1994**, *52*, 1383-1391.
140. Kricheldorf, H. R. and Stricker, A. *Macromolecular Chemistry and Physics* **2000**, *201*, 2557-2565.
141. Kricheldorf, H. R. and Stricker, A. *Polymer* **2000**, *41*, 7311-7320.
142. Carter, K. R., Richter, R., Kricheldorf, H. R., and Hedrick, J. L. *Macromolecules* **1997**, *30*, 6074-6076.
143. Darensbourg, D. J., Ganguly, P., and Billodeaux, D. *Macromolecules* **28-6-2005**, *38*, 5406-5410.
144. Matsuo, J., Nakano, S. L., Sanda, F., and Endo, T. *Journal of Polymer Science Part A: Polymer Chemistry* **1998**, *36*, 2463-2471.

145. Yu, F. and Zhuo, R. *Polymer Journal* **2004**, *36*, 28-33.
146. Matsumura, S., Tsukada, K., and Toshima, K. *Macromolecules* **1997**, *30*, 3122-3124.
147. Bisht, K. S., Svirkin, Y. Y., Henderson, L. A., Gross, R. A., Kaplan, D. L., and Swift, G. *Macromolecules* **15-12-1997**, *30*, 7735-7742.
148. Feng, J., He, F., and Zhuo, R. *Macromolecules* **2002**, *35*, 7175-7177.
149. Sepulchre, M., Sepulchre, M. O., Dourges, M. A., and Neblai, M. *Macromolecular Chemistry and Physics* **2000**, *201*, 1405-1414.
150. Wang, H., Dong, J. H., and Qiu, K. Y. *Journal of Polymer Science Part A: Polymer Chemistry* **1998**, *36*, 695-702.
151. Habraken, W. J. E. M., Zhang, Z., Wolke, J. G. C., Grijpma, D. W., Mikos, A. G., Feijen, J., and Jansen, J. A. *Biomaterials* **2008**, *29*, 2464-2476.
152. Dobrzynski, P., Pastusiak, M., and Bero, M. *Journal of Polymer Science Part A-Polymer Chemistry* **2005**, *43*, 1913-1922.
153. Velasco, M. J., Rubio, F., Rubio, J., and Oteo, J. L. *Thermochimica Acta* **8-2-1999**, *326*, 91-97.
154. Soria, J., Sanz, J., Sobrados, I., Coronado, J. M., Maira, A. J., Hernandez-Alonso, M. D., and Fresno, F. *Journal of Physical Chemistry C* **19-7-2007**, *111*, 10590-10596.
155. McDevitt, Neil T. and Baun, W. L. *Spectrochimica Acta* **1964**, *20*, 799-808.
156. Sayilkan, F., Asilturk, M., Sayilkan, H., Onal, Y., Akarsu, M., and Arpac, E. *Turkish Journal of Chemistry* **2005**, *29*, 697-706.
157. Kriegsmann, H. and Licht, K. *Zeitschrift fur Elektrochemie* **1958**, *62*, 1163-1174.
158. Rodriguez, J. C., Hernandez, R., Gonzalez, M., Rodriguez, Z., Tolon, B., Velez, H., Valdes, B., Lopez, M. A., and Fini, A. *Il Farmaco* **2003**, *58*, 363-369.
159. Ling, J., Shen, Z. Q., and Huang, Q. H. *Macromolecules* **2001**, *34*, 7613-7616.
160. Magonov, S. N., Elings, V., and Whangbo, M.-H. *Surface Science* **1-4-1997**, *375*, L385-L391.

161. Amerio, E., Sangermano, M., Malucelli, G., Priola, A., and Voit, B. *Polymer* **28-11-2005**, 46, 11241-11246.
162. Malkani, A. L., Price, M. R., Crawford, C. H., and Baker, D. L. *Journal of Arthroplasty* **2009**, 24, 1068-1073.
163. Casanova, R. M. and Pathak, C. P. PCT Patent Application WO2007056762 , **2007**.
164. Castillo, M. V. and Joquin Walker, J. US Patent 6077880 , **2000**.
165. Mattox, D. M. In *Handbook of physical vapor deposition (PVD) processing*, William Andrew Publishing/Noyes 1998.
166. ASTM F 640, Standard test methods for determining radiopacity for medical use , **2007**.
167. Watts, D. C. and McCabe, J. F. *Journal of Dentistry* **1999**, 27, 73-78.
168. Burdock, G. A. In *Encyclopedia of Food and Color Additives*, CRC Press 26-11-1996.
169. Barel, A. O., Paye, M., and Maibach, H. I. In *Handbook of Cosmetic Science and Technology*, Third Edition ed.; Informa Healthcare 2009.
170. Brunette, D. M., Tengvall, P., and Textor, M. In *Titanium in medicine*, Springer 2001.
171. Mulhonen, V., Kujala, S., Vuotikka, A., Aaritalo, V., Peltola, T., Areva, S., Narhi, T., and Tuukkanen, J. *Acta Biomaterialia* **2009**, 5, 785-793.
172. Chu, C. L., Wang, R. M., Hu, T., Yin, L. H., Pu, Y. P., Lin, P. H., Dong, Y. S., Guo, C., Chung, C. Y., Yeung, K. W. K., and Chu, P. K. *Journal of Materials Science-Materials in Medicine* **2009**, 20, 223-228.
173. Yang, Y. Z., Park, S. W., Liu, Y. X., Lee, K. M., Kim, H. S., Koh, J. T., Menge, X. W., Kim, K. H., Ji, H. B., Wang, X. D., and Ong, J. L. *Vacuum* **2008**, 83, 569-574.
174. De Jaeger, R. and Gleira, M. In *Inorganic Polymers*, Nova Science Publishers 2007.
175. Nakade, M., Ichihashi, K., and Ogawa, M. *Journal of Sol-Gel Science and Technology* **2005**, 36, 257-264.
176. Camino, G., Lomakin, S. M., and Lazzari, M. *Polymer* **2001**, 42, 2395-2402.

177. Smith, A. Lee *Spectrochimica Acta* **1960**, *16*, 87-105.
178. Takahashi, R, Takenaka, S., Sato, S., Sodesawa, T., Ogura, K., and Nakanishi, K. *Journal of the Chemical Society, Faraday Transactions* **1998**, *94*, 3161-3168.
179. McCafferty, E. and Wightman, J. P. *Surface and Interface Analysis* **1998**, *26*, 549-564.
180. Agrawal, M., Pich, A., Gupta, S., Zafeiropoulos, N. E., Simon, P., and Stamm, M. *Langmuir* **2008**, *24*, 1013-1018.
181. Kelly, P. V., Mooney, M. B., Beechinor, J. T., O'Sullivan, B. J., Hurley, P. K., Crean, G. M., Zhang, J. Y., Boyd, I. W., Paillous, M., Jimenez, C., and Senateur, J. P. *Advanced Materials for Optics and Electronics* **2000**, *10*, 115-122.
182. An, C. H. and Sugimoto, K. *Journal of the Electrochemical Society* **1992**, *139*, 1956-1962.
183. Sun, Y., Sermon, P. A., and Vong, M. S. W. *Thin Solid Films* **1996**, *278*, 135-139.